UNIVERSITÀ DEGLI STUDI DI MILANO–BICOCCA
Facoltà di Scienze Matematiche, Fisiche e Naturali

Scuola di Dottorato in Scienze

Corso di Dottorato di Ricerca in Fisica ed Astronomia
XXIII Ciclo

The high voltage system of the RICH and the multiplicity study with LHCb data

Relatore:
Prof.ssa Clara MATTEUZZI
Correlatori:
Prof. Gianluigi PESSINA
Dr. Thierry GYS

Tesi di dottorato di:
Erica FANCHINI
Matricola: **033495**

...Mi piace scivolarvi fuori da ogni calcolo
Per riportarmi in riga servirà un miracolo...

Negrita

CONTENTS

RIASSUNTO

Questa tesi rappresenta il lavoro che ho effettuato nel corso della scuola di dottorato presso l'Univerità degli studi di Milano–Bicocca nell'ambito dell'esperimento LHCb.
L'esperimento, situato presso il CERN di Ginevra, si appresta a studiare la violazione di CP e ricercare nuova fisica oltre il Modello Standard sfruttando i decadimenti rari degli adroni contenenti i *quark b*.
Mi sono inserita nel gruppo che si occupa del rivelatore *Ring Imaging Cherenkov Counter* (RICH). Il rivelatore è necessario per l'identificazione di particelle e sfrutta l'effetto Cherenkov prodotto dall'interazione di particelle cariche che attraversano materiali radiatori.
I fotorivelatori utilizzati nel RICH sono i *Pixel Hybrid Photon Detectors* (HPD), capaci di convertire i fotoni incidenti in fotoelettroni. Un sistema di schede distribuisce l'alta tensione a tre elettrodi (-18 kV, -17.7 kV e -14.8 kV) ed i fotoelettroni prodotti vengono focalizzati dal campo così creato sull'anodo. Questi rilasciano la loro energia in una matrice di pixel di silicio da cui si ottiene un segnale di tipo binario.
Il mio lavoro di tesi si divide in due parti: la parte strumentale e la parte di analisi dati.
Il lavoro svolto per la parte strumentale si è focalizzato nell'ottimizzazione e nello studio di stabilità e di rumore del sistema di alimentazione con le alte tensioni per i fotorivelatori utilizzati.
Si è inizialmente effettuato uno studio per la riduzione delle sistematiche, svolto con i dati ottenuti dalle misure di caratterizzazione effettuate a Milano, che ha permesso di ottenere una maggiore sensibilità sulla stima, in fase di monitoraggio, del valore delle tensioni applicate. Unitamente al successivo studio dei comportamenti durante la fase di *commissioning* al CERN di Ginevra, la riduzione delle sistematiche sviluppata durante il mio periodo di dottorato è risultata importante per l'ottimizzazione del rivelatore.
L'erogazione delle alte tensioni avviene a circa 40 m dal rivelatore, questo ha imposto uno studio di stabilità. Unitamente a questo, la rivelazione di rumore nella catena di distribuzione ha imposto un'analisi approfondita di tale comportamento. L'analisi ha portato all'identificazione della causa ti tale effetto. Il risultato si è tramutato in una modifica strutturale effettuata dalla casa produttrice per i nuovi alimentatori.
Entrambi gli studi sono stati utili proprio per garantire la massima affidabilità nella ricostruzione degli anelli Cherenkov.
Allo stesso tempo il processo di *upgrade* di LHCb previsto per l'esperimento ha coinvolto il gruppo di Milano–Bicocca. La richiesta di poter lavorare alla luminosità di 10^{33} cm^{-2}s^{-1} con un sistema di lettura adeguato ha portato il gruppo a scegliere di testare un nuovo sistema di fotorivelazione. In questo ambito abbiamo testato il fotorivelatore multianodo

Hamamatsu H9500, su cui sono state eseguite misure di *cross–talk* e di rumore per segnali di singolo fotone. Il cross–talk si rivela solo in una frazione di circa il 10% dei segnali, con un'ampiezza vicina al 30%. Questo fenomeno si interpreta statisticamente nella perdita di un elettrone al primo dinodo della catena di moltiplicazione. Tutte le misure sono state infatti eseguite con una sorgente di singolo fotone e non con luce uniforme come invece effettuate dalla casa produttrice.
Nella seconda parte della mia tesi mi sono occupata dell'analisi dei primi dati raccolti da LHCb. I dati presi in esame sono le collisioni protone–protone avvenute nel 2010 con energie nel centro di massa $\sqrt{s} = 7$ TeV.
Lo studio delle prime collisioni con i suoi eventi di *minimum bias* sono utili per la caratterizzazione e calibrazione dell'esperimento.
Gli eventi di *minimum bias* sono eventi raccolti con le minime richieste di *trigger* dovuti prevalentemente a collisioni inelastiche non difrattive che avvengono con uno scambio minimo di momento trasverso. Alle energie in gioco ad LHC le funzioni di struttura utilizzate nei Monte–Carlo usati per descrivere tali eventi sono estrapolate da dati a più basso Q^2. È molto interessante quindi uno studio di tali eventi, per validare i generatori utilizzati.
In particolare, dopo aver analizzato diverse distribuzioni per le diverse tipologie di traccia, mi sono soffermata sullo studio di possibili asimmetrie di carica nel rivelatore. Il confronto con le simulazioni Monte–Carlo ha dimostrato una buona descrizione della realtà.
Questo lavoro è stato svolto in vista di un'ottimizzazione del Monte–Carlo per una corretta descrizione del rivelatore e per l'analisi dei dati.

ABSTRACT

This thesis is about the work done during my PhD at the Univerità degli studi di Milano–Bicocca. During these three years I was involved in the RICH group of the LHCb experiment.
LHCb is one of the four main experiments at CERN. It uses proton–proton collisions to study CP violation and to search for new physics beyond the Standard Model in the *b* decays.
One of the main feature of the experiment is the particle identification, performed with the Ring Imaging Cherenkov (RICH) technology.
The RICH detects Cherenkov rings via photons emitted by charged particles traversing radiator materials. The photon detection system used consists of pixel Hybrid Photon Detectors (HPDs). They convert photons into photoelectrons which are then accelerated by means of a field generated by three electrodes, biased with high voltages (-18 kV, -17.7 kV and -14.8 kV), onto the silicon pixel anode. The energy released in the pixel is converted into a binary output.
My work can be divided in two main parts: the hardware and the data analysis.
The hardware activity is focused on the High Voltage (HV) supply and distribution systems. I optimized the voltage measurement system reducing the systematics determining improvement in the voltage resolution. This result was obtained using measurements taken during the characterization tests performed in Milano.
The strong requirement of a good stability implies a continuous monitoring and analysis of the commissioning data. The HV supply system is placed about 40 m from the experiment and voltages must remain stable until they reach the HPDs.
The study of the noise evolution and the discovery of its cause determined the substitution of a component inside the supply modules. The company after this evaluation decided to replace a component with a new material in all the new HV modules produced.
All the analysis contributed largely to the stability of the RICH system for all the operations of data taking.
For future operations, LHCb aims at collecting data at a LHC luminosity of 10^{33} cm^{-2}s^{-1}, to improve the statistics of the main rare channels studied. For the RICH, this implies a new readout system. The Milano group decided to design a new front–end electronics system and is studying the performance of commercial Multi anode Photo Multiplier (MaPMT) produced by Hamamatsu.
I participated to the test of the H9500 tube. We obtained a complete characterization of this tube with respect to the single photon electron response. The main issues were to study

noise and cross–talk effects. These are important because one of the RICH requirement is the single photon detection.
The tests done in Milano confirmed the cross–talk percentage at the level of 10% with an amplitude of the order of 30% due to the loss of photoelectrons in the first stages of the multiplication chain. The important aspect is that this measurement was obtained using a single photon light source instead of a uniform light source used by the company.
All these tests concluded that this MaPMT can be a good candidate for the upgrade, but other photodetectors are under test and the choice will be done in the near future.
In the second part of my work I analyzed the first data taken by LHCb with proton–proton collisions at $\sqrt{s} = 7$ TeV.
I used the minimum bias sample collected with a very loose trigger in the very first part of 2010.
Minimum bias events are important for understanding the detector and its response. They are due to inelastic processes: these processes are related to the distribution of quarks and gluons inside the proton. These distributions are extrapolated from experiments at lower energies up to $\sqrt{s} = 7$ TeV. LHC data will be therefore ultimately important to validate the QCD calculation of the evaluation of the structure function.
The analysis concerned a first study of the track distributions in the detector, followed by the study of a possible detector charge asymmetry. Data were compared with Monte–Carlo simulations, which describe data satisfactory.
This study was done to obtain the most reliable detector description in view of measuring CP asymmetry in the b sector, where charge asymmetry of the detector response could be a dangerous contribution to the systematic error.

LHCb is the Large Hadron Collider (LHC) experiment dedicated to precise measurements of CP violation and rare decays in the B meson sector and it is already operational since November 2009.
LHCb is a one arm spectrometer designed and optimized to match the kinematical structure of $b\bar{b}$ events produced in a proton–proton collision at $\sqrt{s} = 14$ TeV. One of the key aspects of LHCb is the identification of the particles. This tool is achieved using the Ring Imaging CHerenkov (RICH) detector technology.
The spectrometer is currently collecting data.
This thesis is structured into six chapters:

Chapter 1 describes the LHC machine and gives a general introduction to the Standard Model (SM) and to the CP violation. The experimental status of the CKM matrix is also given.

Chapter 2 describes the LHCb spectrometer layout. All detectors are described separately and their performance are also reported

Chapter 3 is divided into two parts. In the first part there is a short RICH detectors description. Pixel Hybrid Photon Detectors (HPDs) are the photon detectors developed to detect Cherenkov light. They convert photons into photoelectrons focusing them onto a silicon pixel matrix with a binary redout. Three electrodes are necessary to produce the focusing field and they are biased by three high voltages (the highest at -18 kV).
The second part is focused on the high voltage distribution system. The necessity to detect the single photon signal with high spatial accuracy determined a high voltage resolution study. Stability and reliability of the system are important and the analysis was done to determine a reduction of the systematic error of the voltage measurement. It has been obtained optimizing the characterization of high voltage distribution boards.

Chapter 4 contains a complete description of the HPD high voltage supply system during operations. Following the study reported in the previous chapter, the monitoring and the characterization of the entire high voltage system during operations is described here. The analysis of voltage and current stability necessary to the detector reliability is reported. An investigation on the observed noise, its source and the involved implications are described.

Chapter 5 introduces the LHCb upgrade and the necessity to replace the photon detectors presently in use with another one having a faster redout while maintening a good detection efficiency for a single photon signal. In this chapter a description of the tests done with the MaPMT H9500 is given. An analysis of the cross–talk, done for a single photon signal response, is made. All these tests concluded that the MaPMT H9500 can be considered as a good candidate for the upgrade.

Chapter 6 describes the analysis of the charged particles distributions with data taken in 2010 at $\sqrt{s} = 7$ TeV. To study the detector response is important to compare data

and Monte Carlo samples. Minimum bias events were used to investigate a possible charge asymmetry induced by the detector itself. This study was done using two different sample collected with opposite magnetic field which demonstrate the detection response uniformity of the spectrometer. The charge asymmetry induced by the proton–proton collisions is also investigated.

CHAPTER 1

THE LARGE HADRON COLLIDER AND THE STANDARD MODEL

LHC is the new high–energy particle accelerator which gives the possibility to study in details matter–antimatter imbalance. The high energies already reached, in the first year of operation, are used to study particles created with hadron–hadron interactions.
In this chapter there is a brief description of the LHC machine and an introduction to the Standard Model and CP violation. This is necessary to introduce LHCb, one of the big experiments at LHC.

1.1 A universe of matter

The known universe is made up by matter particles (protons, neutrons and electrons) rather than their antimatter partners (antiprotons, antineutrons and positrons).
There are two sectors which can study matter–antimatter imbalance: elementary particle and astroparticle physics.
Astrophysics with the Cosmic Microwave Background (CMB) radiation shows that, in the early days of the cosmos, particles and antiparticles were populating it on equal basis. This supports the hypothesis that, the Big-Bang i.e. the birth of the universe, should have created equal amounts of matter and antimatter. Since then, particles and antiparticles were continuously annihilating each other. On the other side high energy photons were keeping on creating matter–antimatter pairs.
The expansion and the consequent cooling down of the universe made the high energy photons rarer and rarer. This effect left the annihilation process no longer balanced by pair creation. All antibaryons disappeared and only a small amount of barions survived building the universe as known today. A pictorial evolution scheme of the universe since the Big–Bang is displayed in Fig. 1.1.
Matter–antimatter imbalance is already a controversial subject. Sakharov [1, 2] explains it making three hypothesis:

1. Non conservation of the baryon number

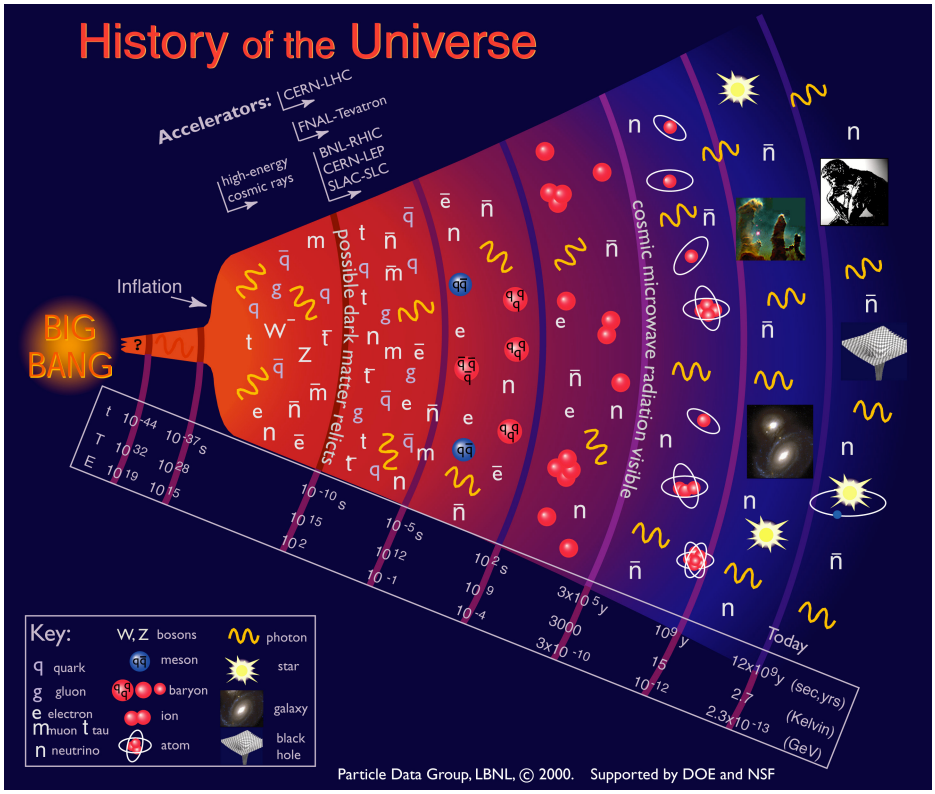

Figure 1.1: Pictorial description of the universe history since the Big–Bang

2. Baryogenesis CP violation

3. Lack of thermal equilibrium

These three points are also valid in the Standard Model (SM). An example is the SM predicted baryon number violation, never observed until today. The only evidence is the barions abundance [3]. Another possibility is the SM CP violation. However the effect described by the SM is too small to explain the observed matter–antimatter asymmetry.
These open questions could be explained with New Physics (NP) effects.
The new Large Hadron Collider (LHC) machine can help to answer these questions. LHCb is one of the experiments taking data at the LHC. It is performing the most precise measurements of CP violation symmetry in the b quark sector. This will allow to test deeper the SM and potentially to find NP contributions beyond it.

1.2 The Large Hadron Collider

Most high energy particle physics experiments use colliders to produce high energy densities required. The Large Hadron collider (LHC) [4], shown in Fig. 1.2, is the highest energy particle accelerator ever constructed and operated.
It is a circular storage ring 26.7 km long, placed around the French-Swiss border to the west of Geneva and lying between 45–170 m underground.
It has four colliding points where the four main experiments (ALICE [5, 6], ATLAS [7, 8],

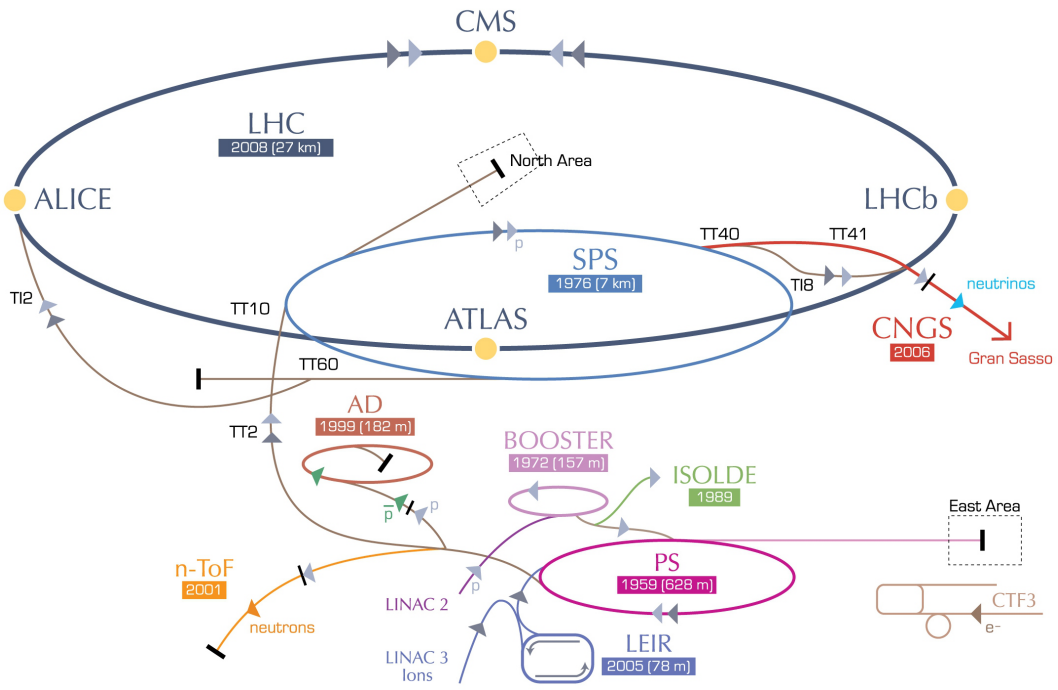

Figure 1.2: Scheme of the CERN accelerator systems

CMS [9, 10] and LHCb (details in Chapter 2)) are located.
ALICE is a dedicated experiment for heavy ion collision for quark-gluon plasmas studies. The other three experiments were designed mainly to study proton–proton collisions. Two of them (ATLAS and CMS) are general purpose experiments to study SM limits, Higgs boson and supersimmetry models. LHCb is the detector devoted to CP violation and B meson rare decay studies.
LHC is designed to circulate proton bunches with intervals of 25 ns corresponding to a bunch crossing frequency of 40 MHz. Given the filling scheme, the real frequency is reduced to 33 MHz. The bunch number reduction is needed for beam injection and dumping (some bunches are empty) from SPS into LHC. The collider magnets are based on Niobium-Titanium alloy superconducting technology. To maintain temperature lower than ~ 2 K super–fluid helium cools all the cryostates placed around the accelerator ring.
LHC is designed to obtain the nominal center of mass energy of $\sqrt{s} = 14$ TeV (7 TeV per colliding beam) and a luminosity up to 10^{34} cm^{-2}s^{-1}.
To obtain this result dipole magnets, in Fig. 1.3, are used to make the beams turning around the circular trajectories and quadrupole magnets, in Fig. 1.4, to focus beams. There are also RadioFrequency (RF) cavities used to increase beam energy.
LHC is also able to accelerate ions $^{208}Pb^{82+}$ up to 2.76 TeV energy per nucleon. It corresponds to a center of mass energy of 1.15 PeV and a nominal luminosity of 10^{27} cm^{-2}s^{-1}.
To obtain these performance LHC alone is not enough. It is only the last step of a complex system of accelerators already existing at CERN, as shown in Fig. 1.2.
Protons are first accelerated through a linear accelerator (LINAC2) to the energy of 50 MeV, then through the Booster to 1.4 GeV. The next accelerator is Proton Synchrotron (PS) to reach 25 GeV and finally the Super Proton Synchrotron (SPS) accelerates protons up to

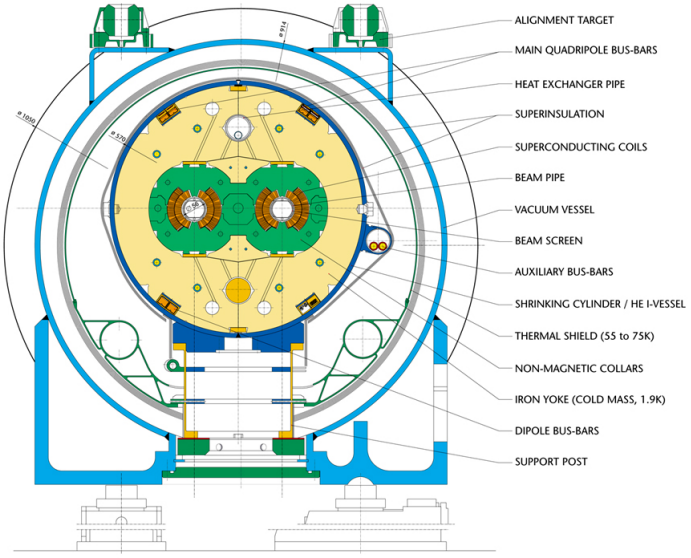

Figure 1.3: Cross–sections of the LHC dipole magnets

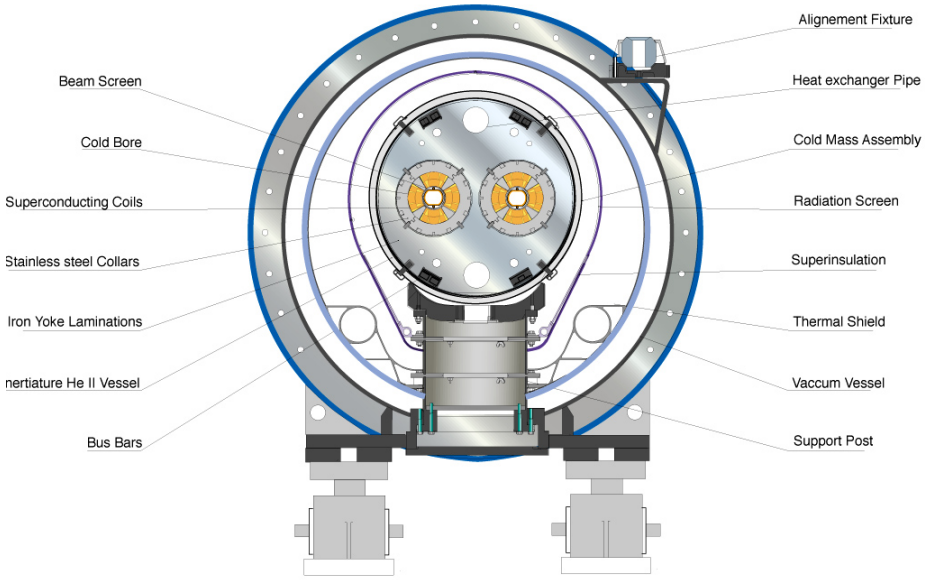

Figure 1.4: Cross–sections of the LHC quadrupole magnets

450 GeV, before injecting them into LHC.
This circular storage rings enable beams to circulate many times increasing energy at each revolution. However, some energy is lost because of the synchrotron radiation. The loss rate $dE/dt \propto 1/m^4 r^2$ with r the ring radius and m the particle mass. For this reason protons were chosen to reduce this huge power loss, compared to the electrons previously used.
To obtain the nominal 40 MHz frequency 3564 bunches (only 2808 filled with $\sim 10^{11}$ protons each) will be equally spaced of 7.5 m. The limitation is the complicated filling procedure. Beams mean lifetime should be of $\sim$10 h achieved by maintaining high vacuum conditions of better than 10^{-8} mbar inside the beam pipes.

1.3 The luminosity

An important aspect to consider is the event rate $R(t)$. In a collider this rate is proportional to the cross section σ of a given process and to the instantaneous luminosity $\mathcal{L}(t)$. The rate is defined as:

$$R(t) = \sigma \times \mathcal{L}(t) \tag{1.1}$$

where σ is the process cross section and $\mathcal{L}(t)$ is the instantaneous luminosity.
The number of events N occurred in a certain time interval T, needs the time–integrated luminosity to be calculated:

$$\mathcal{L}_{int} = \int_0^T \mathcal{L}(t)dt \tag{1.2}$$

The machine luminosity depends only on the beam parameters and can be written, assuming a Gaussian beam distribution, as:

$$\mathcal{L}(t) = \frac{N_1 N_2 k_b f \gamma F}{4\pi\beta^*\varepsilon} \tag{1.3}$$

where γ is the relativistic factor, N_i the particle number per colliding bunch, f the beam revolution frequency, k_b is the number of bunches per beam, ε the emittance i.e. the compactness of the beam, β the beam focusing factor at the interaction point and F the crossing angle factor at the colliding point. At LHC the factor $k_b \times f$ is the crossing frequency of 33 MHz.
The geometric luminosity reduction factor F due to the crossing angle at the Interaction Point (IP) is defined as:

$$F = \left(1 + \left(\frac{\theta_c \sigma_z}{2\sigma^*}\right)^2\right)^{-\frac{1}{2}} \tag{1.4}$$

θ_c is the full crossing angle and is 300 μrad at LHCb, σ_z the RMS bunch length and σ^* the transverse RMS beam size at the IP. The Eq. 1.4 assumes round beam profiles and equal beam parameters for both beams.
The number n of proton–proton interactions occurring in a bunch crossing follows a Poisson distribution:

$$P(\mu, n) = \frac{\mu^n}{n!} e^{-\mu} \tag{1.5}$$

where μ is the proton–proton average number of collisions per bunch crossing. It is related to luminosity and to the total inelastic pp cross–section:

$$\mu = \frac{\sigma_{inel}\, \mathcal{L}(t)}{f_{\mathrm{LHC}}\, \varepsilon_{filled}} \tag{1.6}$$

where σ_{inel} ($\sim$ 80 mb) is the total inelastic pp cross section, $\mathcal{L}(t)$ is the luminosity, f_{LHC} is the 40 MHz LHC bunch crossing frequency and ε_{filled} (0.744 for LHCb) is the fraction of non–empty bunch crossings. In Fig. 1.5 the probability distributions, for several n, are plotted as a function of the luminosity.

A higher luminosity results in a smaller number of bunch crossings with no interaction

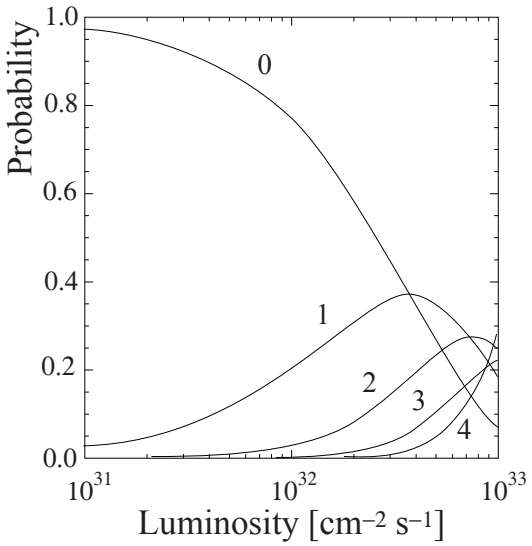

Figure 1.5: Interaction probability distributions as a luminosity function

($n = 0$), multiple interactions ($n > 1$) increase causing an higher detection occupancy.
In order to have a high precision on decay distances, primary and secondary vertexes have to be measured accurately. For this reason it is important to have one interaction per bunch crossing.
Considering Fig. 1.5, with a $\sigma_{inel} = 80$ mb, 4×10^{32} cm^{-2}s^{-1} is the highest luminosity to maximize the single interaction probability. However, at that luminosity multiple interactions probability is high. Running at these high luminosities, the average number of proton–proton collisions per bunch crossing is greater than one making the event reconstruction more difficult and time–consuming.
Reducing the detector occupancy which afflicted the vertex locator and the tracking system, it is possible to obtain more precise measurements. Moreover this effect reduces also possible radiation damages. For this reason the LHCb nominal designed luminosity is 2×10^{32} cm^{-2}s^{-1}.

1.3.1 The b quark production at LHC

LHC with its energy and luminosity will be a very abundant B meson source.
The dominant b–quark production processes are gluon–gluon fusion and quark–antiquark annihilation. Feynman diagrams are shown in Fig. 6.5. b–quarks are created in pair ($b\bar{b}$) predominantly in the forward and backward directions and at small angles respect to the beam direction. More details are given in Chapter 6.
The geometry of the LHCb detector, considering the physics program based on the $b\bar{b}$ production, is a forward single arm spectrometer as shown in Fig. 1.7.

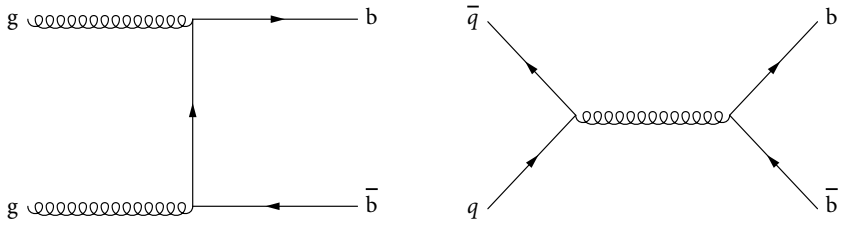

Figure 1.6: Feynman diagrams of the two main *b*–quark production processes at LHC: gluon–gluon fusion (left plot) and quark–antiquark annihilation (right plot)

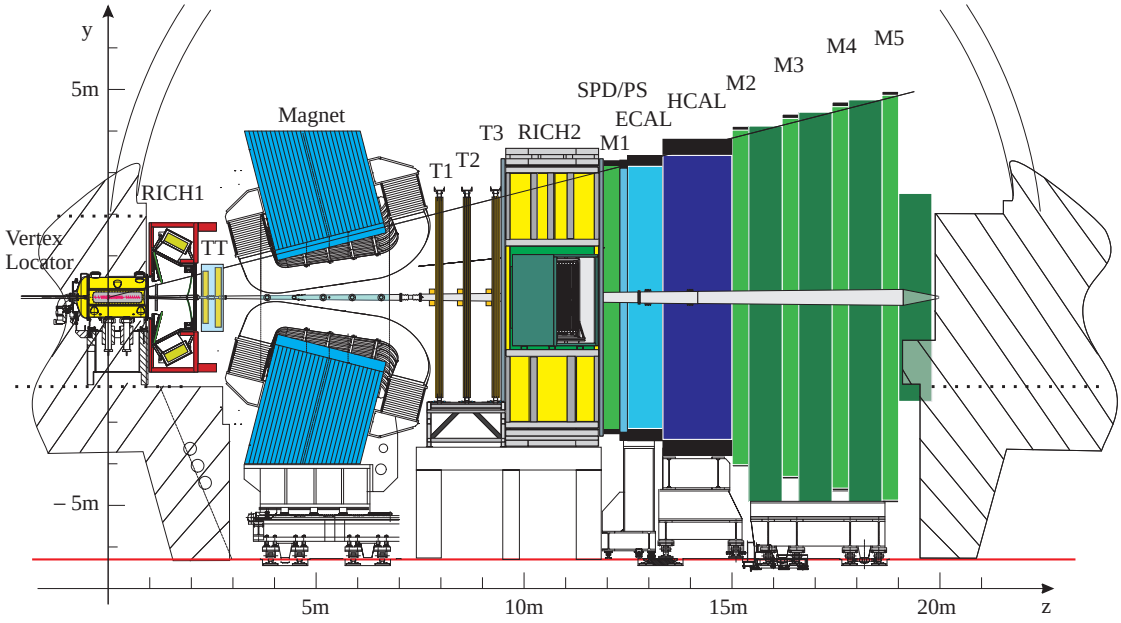

Figure 1.7: Schematic view of the single arm LHCb spectrometer

1.4 The Standard Model

The Standard Model (SM) [11] is a quantum field theory. It describes elementary particles and their interactions (strong, weak and electromagnetic). It is a very successful theory experimentally tested and it describes all the observed phenomena in particle physics up to the energies presently explored. Some predictions have been experimentally confirmed. However it does not include gravitational force and is not able to explain the mass hierarchy. In the SM this hierarchy is described by the Higgs mechanism [12, 13] leaving the Higgs particle the only piece to be discovered.
Physicists believe that SM is an effective low energy model of a more fundamental theory called Grand Unified Theory (GUT) [14] suggesting a strong and electroweak interactions unification.
To describe the SM three discrete symmetries are important to be considered:

Charge conjugation (C): the C operator interchanges a particle with its antiparticle without changing its spin nor momentum

Parity (P): the P operator inverses space transforming a left–handed particle into a right–handed one. It also reverses momentum leaving angular momentum and spin unchanged

Time reversal (T): the T operator interchanges direction of the time. It inverses forward and backward light cones

These symmetries are singled and coupled broken, but the combination of these three operators (CPT) is an exact symmetry in any local field theory: it is an universal invariance. As a consequence of this conservation, mass and lifetime of an elementary particle and its antiparticle must be equal.
Considering SM interactions, strong and electromagnetic are invariant under C, P and T but weak interaction violates C and P. In 1957 it was discovered that β–decay of ^{60}Co nuclei violated P [15]. In 1964 CP violation was observed studying rare decays ($K_L^0 \to \pi^-\pi^+$) of neutral kaons [16]. Since its discovery, CP violation has been deeply investigated in the K meson sector. Only recently (2001) BaBar and BELLE experiments observed CP violation in B meson decays [17, 18] and now also LHCb has started to be operational. B physics is becoming an important framework to test SM and to search NP.
SM describes elementary particles dividing them into fermions and bosons. They differ in the spin value. Fermions have a half integer and bosons an integer spin. Fermions, listed in Tab. 1.1, are divided in three families of quarks and leptons interacting through electromagnetic, weak and strong forces. All their interations happen through a mediating force carriers exchanged as listed in Tab. 1.2.
The six quarks interact through all fundamental forces, having mass, electric charge, weak isospin and color charge.
Electron, muon and tau leptons have integer electric charges and are coupled with neutral leptons called neutrinos. Charged leptons are involved in all except in strong interactions, not having color charge, and neutrinos are involved only in weak interactions.
In nature quarks do not exist as free particles, all quarks except the top (it decays before hadronizing), are combined into composite particles called hadrons.
The existence of three quark families allow the SM CP violation in the weak interactions.

Type	Name	Generation	Name	Type
Leptons	Electron (e) Electron neutrino (ν_e)	1	Up (u) Down (d)	Quarks
	Muon (μ) Muon neutrino (ν_μ)	2	Charm (c) Strange (s)	
	Tau (τ) Tau neutrino (ν_τ)	3	Top (t) Bottom (b)	

Table 1.1: The three main generations of the Standard Model particles

In 1963 Cabibbo introduced a mixing angle (θ_c) between d and s quarks [19]. Only in the 1973 Kobayashi and Maskawa proposed a quark mixing model assuming three generations of quarks [20].
The CP violation origin is due to these weak charged–current interactions. They are described by a Lagrangian function showing the quark flavor transitions of the left-handed

Force	**Gauge boson**
Strong	Gluons (g_i)
Electromagnetic	Photon (γ)
Weak	Bosons ($W^{\pm}$, Z^0)

Table 1.2: Standard Model fundamental forces and mediating gauge bosons

components of the quark mass eigenstates:

$$L_{int}^{CC} = -\frac{g_2}{\sqrt{2}} (\bar{u}_L,\ \bar{c}_L,\ \bar{t}_L,) \gamma^{\mu} V_{CKM} \begin{pmatrix} d_L \\ s_L \\ b_L \end{pmatrix} W_{\mu}^{\dagger} + h.c. \tag{1.7}$$

the interaction strength is given by g_2, the $SU_L(2)$ gauge coupling. $W_{\mu}^{\dagger}$ is the W–boson exchange operator, γ^{μ} the Dirac matrices, V_{CKM} the CKM quark mixing matrix and (d_L, s_L, b_L) represent the left–handed quark mass eigenstates.

1.5 The CKM matrix

The unitary 3×3 Cabibbo–Kobayashi–Maskawa (CKM) matrix describes weak interactions among quark families. The unitarity is required by the gauge theory and the SM assures the absence of tree level flavor changing neutral current transitions.

$$\begin{pmatrix} d' \\ s' \\ b' \end{pmatrix} = V_{CKM} \begin{pmatrix} d \\ s \\ b \end{pmatrix} = \begin{pmatrix} V_{ud} & V_{us} & V_{ub} \\ V_{cd} & V_{cs} & V_{cb} \\ V_{td} & V_{ts} & V_{tb} \end{pmatrix} \begin{pmatrix} d \\ s \\ b \end{pmatrix} \tag{1.8}$$

The V_{ij} terms are complex numbers and indicate the quark mixing transition probability.
In the SM with 3 quark families, the V_{CKM} matrix has three rotation angles and one complex phase. This phase introduces the CP violation in the SM [20]. No CP violation is expected if only two generations of quarks are considered.
The CKM matrix can be re–written in different modes. Several parametrization are available and based on its unitarity [20, 21].
One of the most known and useful is due to Wolfenstein [22]. Each element is expanded as a power series of parameter $\lambda \equiv |V_{us}| = sin\theta_c \approx 0.22$ which is the Cabibbo's angle θ_c. The diagonal elements are close to unity and the off–diagonal elements are progressively smaller. The fifth order parametrization accessible to LHC is:

$$\mathbf{V}_{CKM} = \begin{pmatrix} 1 - \frac{1}{2}\lambda^2 + \frac{1}{4}\lambda^4 & \lambda & A\lambda^3(\rho - i\eta) \\ -\lambda + \frac{1}{2}A^4\lambda^4 - A^2\lambda^5(\rho + i\eta) & 1 - \frac{1}{2}\lambda^2 + \frac{1}{4}\lambda^4(1 - 2A^2) & A\lambda^2 \\ A\lambda^3(1 - \rho - i\eta) & -A\lambda^2 + A\lambda^4(\frac{1}{2} - \rho - i\eta) & 1 - \frac{1}{2}A^2\lambda^4 \end{pmatrix} \tag{1.9}$$

followed by elements of the order $O(\lambda^6)$.
The four independent parameters are:

$$\lambda, \quad A, \quad \rho, \quad \eta \tag{1.10}$$

Considering the unitarity:

$$V_{CKM}^{\dagger} V_{CKM} = \mathbf{1} = V_{CKM} V_{CKM}^{\dagger}$$

nine constraining relations between matrix elements arise. Three of them coming from the $\Sigma_j |V_{ij}|^2 = 1$ for each generation i describe the weak universality. The other six equations are orthogonality conditions and can be written as $\Sigma_k V_{ik} V_{jk}^* = 0$ with $i \neq j$. Each of these relations can be represented by a triangle in the complex plane (ρ, η) [23]. Areas of all triangles are the same and equal to half of the Jarlskog invariant [24–26].
The most used triangle, experimentally accessible having all the sides of the same order of magnitude, correspond to the Eq. 1.11 and it is shown in Fig. 1.8.

$$V_{ud} V_{ub}^* + V_{cd} V_{cb}^* + V_{td} V_{tb}^* \tag{1.11}$$

Dividing each side by $V_{cd} V_{cb}^*$ and defining two new variables $\overline{\rho}$, $\overline{\eta}$ as:

$$\overline{\rho} = \rho \left(1 - \frac{1}{2}\lambda^2 \right), \qquad \overline{\eta} = \eta \left(1 - \frac{1}{2}\lambda^2 \right) \tag{1.12}$$

Two of the three triangle vertices are exactly $(0,0)$ and $(1,0)$ as displayed in Fig. 1.8. To have a complete characterization it is necessary to know the three internal angles (α, β and γ). They can be defined in term of the CKM matrix elements:

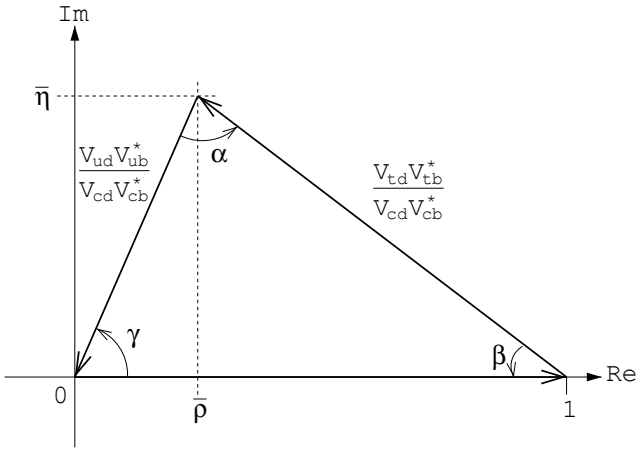

Figure 1.8: The triangle described in Eq. 1.11 It is one of the triangle experimentally accessible

$$\alpha = arg\left(-\frac{V_{td} V_{tb}^*}{V_{ud} V_{ub}^*} \right) \tag{1.13}$$

$$\beta = arg\left(-\frac{V_{cd} V_{cb}^*}{V_{td} V_{tb}^*} \right) \tag{1.14}$$

$$\gamma = arg\left(-\frac{V_{ud} V_{ub}^*}{V_{cd} V_{cb}^*} \right) \tag{1.15}$$

Experimentally the hierarchical pattern of the matrix elements and their absolute values has been measured. Diagonal elements are close to unity and all the others have smaller experimental values as expected.
Experimental measurements can be easily displayed and compared in the $(\overline{\rho},\overline{\eta})$ plane. Using this method, the CP violation description of the SM can be tested by determining the elements of the CKM matrix. Measuring all the angles and side lengths over–constrains the CKM matrix. This offers the possibility to deeply test the SM and find hints of NP if inconsistency is observed between constraints shown in Fig. 1.9 and in Tab. 1.3.

Parameter	**Value**
$\alpha[^\circ]$	$89.0^{+4.4}_{-4.2}$
$\beta[^\circ]$	$23.8^{+2.1}_{-2.0}$
$\gamma[^\circ]$	73^{+22}_{-25}
$sin2\alpha$	$-0.14^{+0.37}_{-0.41}$
$sin2\beta$	0.67 ± 0.023

Parameter	**Value**
λ	0.2253 ± 0.0007
A	$0.808^{+0.022}_{-0.015}$
$\overline{\rho}$	$0.132^{0.022}_{0.014}$
$\overline{\eta}$	0.341 ± 0.013
J_{CP}	$\left(2.91^{+0.19}_{0.11}\right)10^{-5}$

Table 1.3: Main world average parameter values [25, 27]

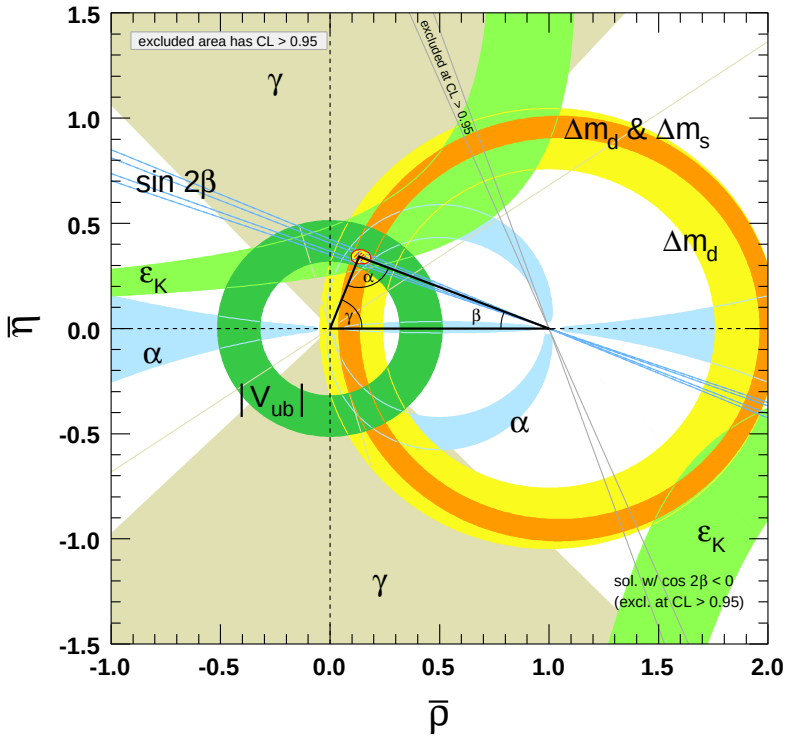

Figure 1.9: Constraints on the $(\overline{\rho}, \overline{\eta})$ plane [27]. The shaded areas correspond to 95% CL

CHAPTER 2

PARTICLE DETECTION AND IDENTIFICATION IN THE LHCb EXPERIMENT

The LHCb experiment consist in a single arm spectrometer designed to study CP asymmetries and rare decays in b and c quark sectors [28].
The selection of the events needed for the offline analysis is provided by a powerful trigger system specifically designed and optimized. In this chapter a general description of the experiment, together with the trigger system, particle and track identification are given.

2.1 The LHCb trigger

Even if the maximum instantaneous luminosity of LHC will be $\mathcal{L} = 10^{34}$ cm^{-2}s^{-1}, in the LHCb interaction point it will be kept to the level of $\mathcal{L} = 2 \times 10^{32}$ cm^{-2}s^{-1}. At this luminosity, events will be dominated by a single visible interaction per bunch crossing, giving a crossing frequency of about 10 MHz. Lower luminosity implies also a lower density particle flux and a lower radiation damage for the detector.
Writing data at the LHC frequency, of 40 MHz, is a very difficult task. For this reason the LHCb trigger, designed to select interesting events for the offline analysis rejecting background, is able to take a fast decision and reduce the event rate. The LHCb strategy is to reduce the frequency down to 2 kHz writing data on disk for further offline analysis. The trigger flow is shown in the Fig. 2.1.
At the LHCb luminosity the rate of the $b\bar{b}$ pairs is estimated to be of the order of 100 kHz, but in the spectrometer acceptance only $\sim$15% of the events contains at least one B meson. The trigger strategy consist of two parts [29]: the Level–0 (L0) and the High Level Trigger (HLT). They have been optimized to maximize the signal to noise ratio during data taking.

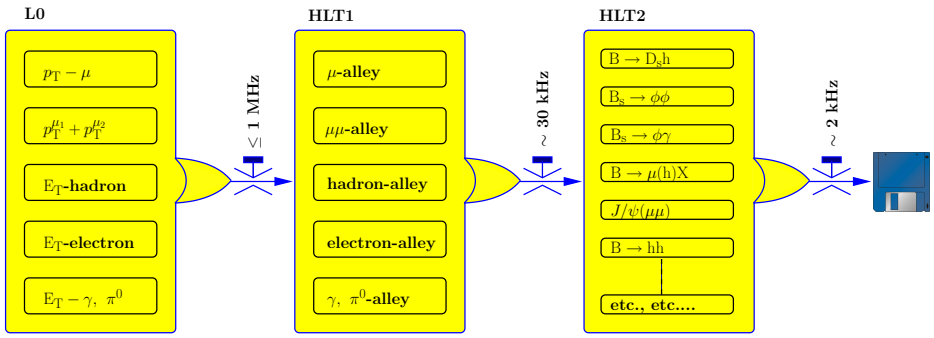

Figure 2.1: Diagram of the trigger flow. The scheme shows the selection applied and the reduction, at each step, of the rate. The LHCb trigger is able to reduce the rate starting from 40 MHz to 2 kHz, frequency used to write data on tape

2.1.1 The Level–0 Trigger

The L0 trigger is an hardware trigger generated by custom made electronics providing the reduction of the events rate. It reduces the LHC beam crossing rate of 40 MHz, down to 1 MHz. At this rate all the channels of the whole experiment can be considered and readout. The selection criteria applied by the trigger were studied considering the physics of LHCb. B mesons, for example, have large masses and when decaying, they produce particles with large transverse energy (E_T) or transverse momentum (p_T). These are all variables considered.
The L0 trigger is provided considering outputs from three components: pile–up, calorimeter and muon [30, 31] system. The cuts applied for the selection are based on:

- the highest E_T hadron, electron and photon clusters in the calorimeters
- the two highest p_T muons in the muon chambers
- number of pp interaction evaluated by the pile–up system of the VELO Sect. (2.3.2)
- charged track multiplicity using the SPD Sect. (2.5.1) hits
- total energy released in the calorimeters

The efficiency of these cuts is shown in the two plots in Fig. 2.2, where there is the comparison between MonteCarlo and data.
A Level–0 Decision Unit (L0DU) collects all these values and takes the decision for each bunch–crossing. This needs a perfect synchronization with the LHC clock. The latency of the L0 trigger is 4 μs, time needed to get the data and takes the decision.

2.1.2 The High level trigger

The second step of the rate reduction is provided by the High Level Trigger (HLT) able to cut from 1 MHZ to 2 kHz the amount of data to store.
HLT is a software application running in a computing farm, the Event Farm Filter (EFF). It takes the L0 output and puts them into alleys which must be confirmed.

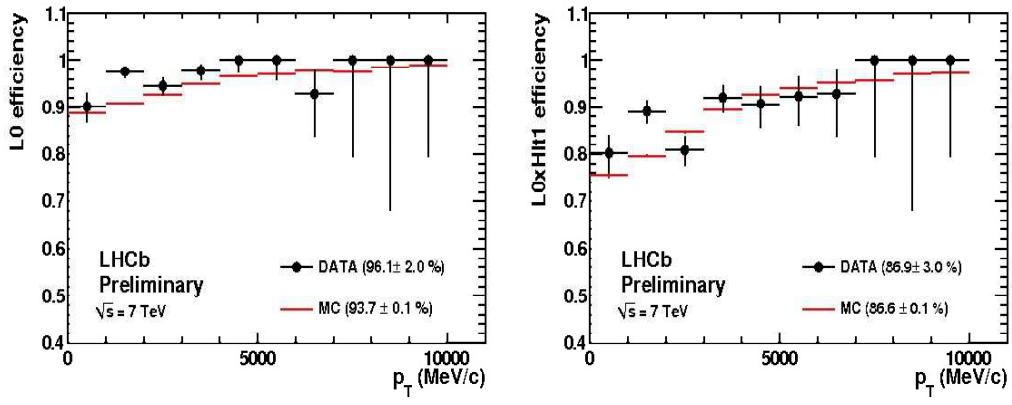

Figure 2.2: Efficiency plot for the muon trigger obtained considering reconstructed J/ψ with $\mathcal{L}_{int} = 14\text{nb}^{-}1$. On the left, the L0 muon trigger efficiency to select J/ψ as a function of p_T. On the right, the muon trigger efficiency considering also HLT1

The HLT structure is divided in two levels, HLT1 and HLT2. HLT1 reconstructs particles from vertex and tracking detectors and confirms the presence or not of neutral particles candidates, reducing the rate to 30 kHz. Before starting the reconstruction, all the L0 outputs must be confirmed, and at the end of this procedure, VELO and/or T-station information are implemented and combined. The alleys run all together in parallel and they act on the appropriate L0 candidate. Cuts on p_T and impact parameter are also considered to reduce further the rate.
The event is selected only if it passes at least one alley, then it is sent to the HLT2. Full reconstruction and pattern recognition are applied to reduce the rate to 2 kHz, applying inclusive and exclusive selection criteria. The HLT2 stage in fact uses cuts either on invariant mass, or on the pointing of the B momentum towards the primary vertex. While the inclusive triggers select partial B decays like $\mu^+\mu^- X$ or $J/\psi X$, the exclusive selection of these channels produces a lower rate. The exclusive criteria, for specific decay channels, produce a smaller rate but it has very loose cuts, compared with the criteria applied with the off–line analysis.
The final trigger decision is the logical OR of the inclusive and exclusive selections.
HLT trigger is an application still in evolution. It follows the progress of the LHC machine in terms of instantaneous luminosity, bunch size, etc. and it is always optimized to meet the computing infrastructure power available.

2.2 Track Reconstruction

All the particles created in *pp* collisions go through the detector and interact with materials depending on their own properties, as shown in Fig. 2.3.
The forward geometry of the LHCb implies that the interaction point is placed on one edge of the experiment in the vertex locator, with the particles boosted in a cone in the forward direction. Important issues are: detection and reconstruction of tracks and active particle identification.
Charged particles are reconstructed by the tracking system.

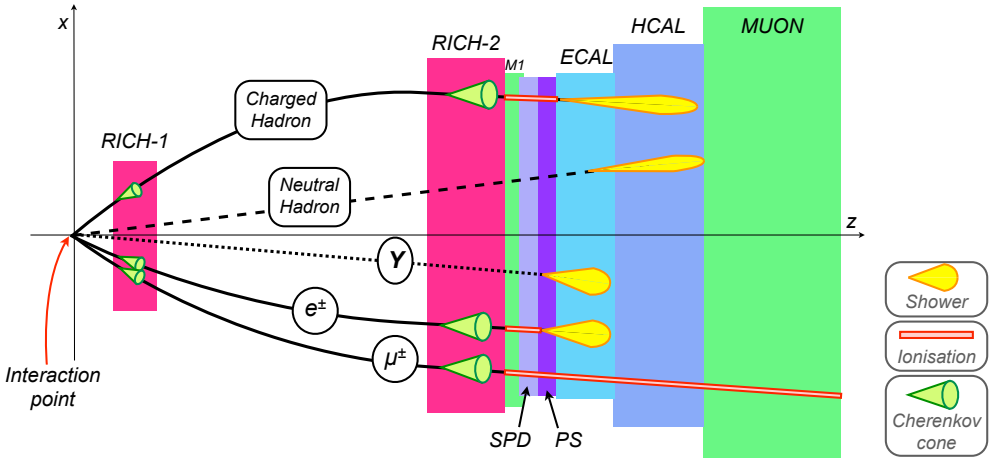

Figure 2.3: The scheme represent different particle interactions in the subdetectors of LHCb

The tracking algorithm takes into account hits from the VErtex LOcator (VELO), the Trigger Tracker (TT), the Inner Tracker (IT) and the Outer Tracker (OT).
Different track types are defined based on the different subdetectors involved. A schematic illustration of the LHCb track types is shown in Fig. 2.4. They are classified as: *Long, Upstream, Downstream, Velo* and *T* tracks.
In the following, some details of each track type are given.

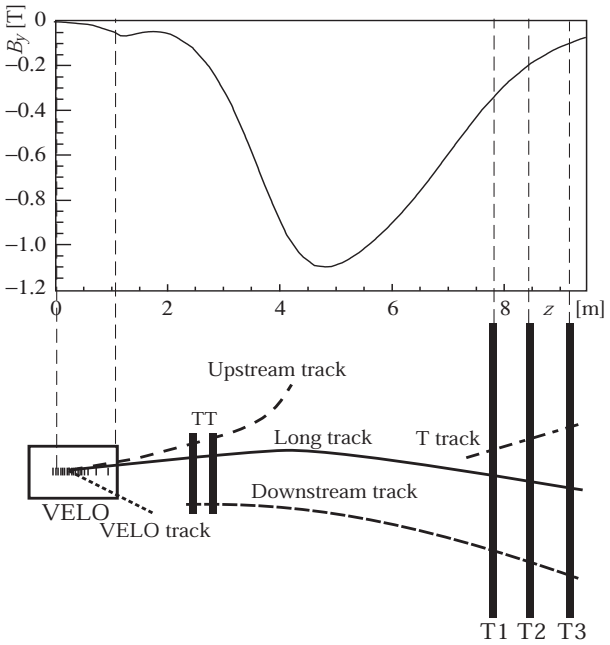

Figure 2.4: Schematic illustration of the LHCb track types together with the By component, in the top plot, of the magnetic field expected from VELO to the tracker stations

→ **Long tracks:** they traverse all the tracking system from the VELO up to the tracking stations. They have the most precise momentum reconstruction and they are used

for the B–decay studies. Long track reconstruction starts considering VELO seeds extrapolating trajectories combining the tracking station informations. This method reconstructs the 90% of these tracks, another 5% is obtained considering T seeds and requiring a match, in the VELO region, with the VELO seeds.
These two methods give a first estimation of the particle momentum. The efficiency is directly proportional to the particle momentum and it decreases for low momentum values, due to the multiple scattering in the material

→ **Upstream tracks:** they have hits only in VELO and TT stations. They present low momenta and are bent out the detector acceptance by the magnetic field. Upstream tracks are useful for tagging purpose, and since they go through the RICH1 detector, they can be used to study the performance of the particle identification. For this type TT is used to establish a momentum measurement with VELO information to confirm the correct track type

→ **Downstream tracks:** they traverse the TT and T stations. They have no hits in the VELO and they are mainly due to K_S^0 e Λ decays which decay outside the VELO acceptance. The reconstruction algorithm is the same as for the upstream case but with no momentum estimation

→ **VELO tracks:** they have hits only in the VELO detector. These tracks have a big polar angle or are backward tracks. They are useful for the Primary Vertex (PV) reconstruction

→ **T tracks:** they are produced in secondary interactions, they have hits only in the T stations and they are mainly used for the RICH2 pattern recognition

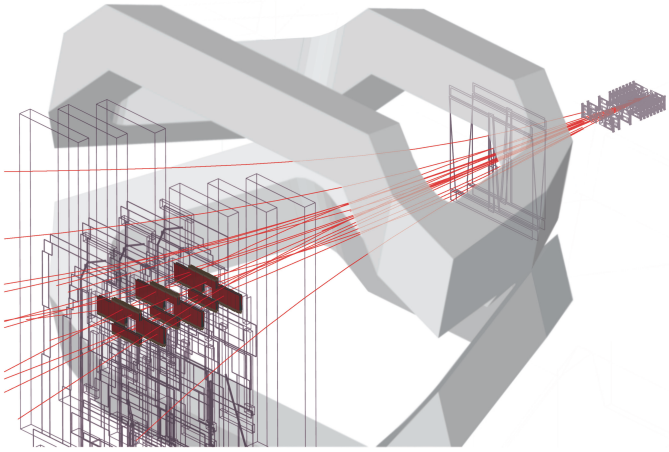

Figure 2.5: 3–D example of reconstructed tracks and detected in one event from VELO up to tracker stations obtained with 2010 data

Track reconstruction is performed considering contributions from different subdetectors, as can be nicely seen in Fig. 2.5. In the following pages the tracking system will be briefly described.

The track reconstruction starts with the search of track seeds in the VELO region and the T stations where the magnetic field is low and particles have straight trajectories.

→ **VELO seed:** it is obtained considering r and ϕ coordinates of the clusters, to reconstruct straight lines with no momentum information

→ **T seed:** it is obtained considering IT and OT hits. The magnetic field is weak but not negligible and it is taken into account by the software. An initial momentum can be assigned to the track seed either from the measured curvature or by assuming that the track originates from the nominal interaction point

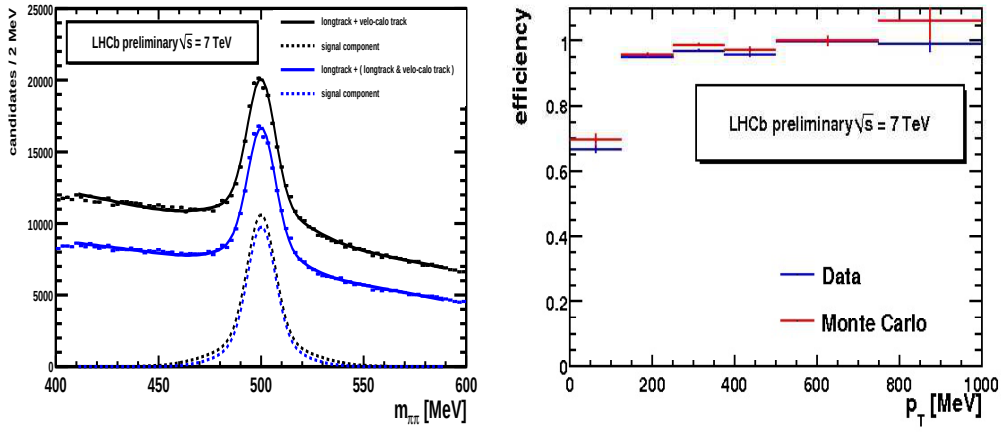

Figure 2.6: invariant mass plots produced considering collision events, for an integrated luminosity of $\mathcal{L} = 14\text{nb}^{-1}$ at 7 TeV. Only long tracks are considered for the K_s^0 reconstruction. On the left: invariant mass of $\pi^+\pi^-$ pair. On the right: efficiency plot for the K_s^0 reconstruction, as a function of the particle transverse momentum

After finding tracks, the trajectories are refitted applying corrections for the multiple scattering and for the dE/dx energy loss. The quality of the reconstructed tracks is monitored by the χ^2 of the fit. In Fig. 2.7 there are two examples of momentum and impact parameter resolution obtained with reconstructed tracks.
To be considered reconstructable must have a minimum number of hits in the relevant subdetectors. Tracks to be considered successfully reconstructed, a track must have at least 70% of associated hits originating from a single MonteCarlo particle.
The tracking performance is evaluated by MonteCarlo in terms of efficiencies and ghost rates. The *reconstruction efficiency* is defined as the fraction of reconstructable tracks that are successfully reconstructed, and the *ghost rate* is defined as the fraction of reconstructed tracks that are not matched with a true particle, shown in Fig. 2.6. One example is the efficiency plots obtained reconstructing K_s^0 selecting only long tracks. The comparison with MonteCarlo is given.

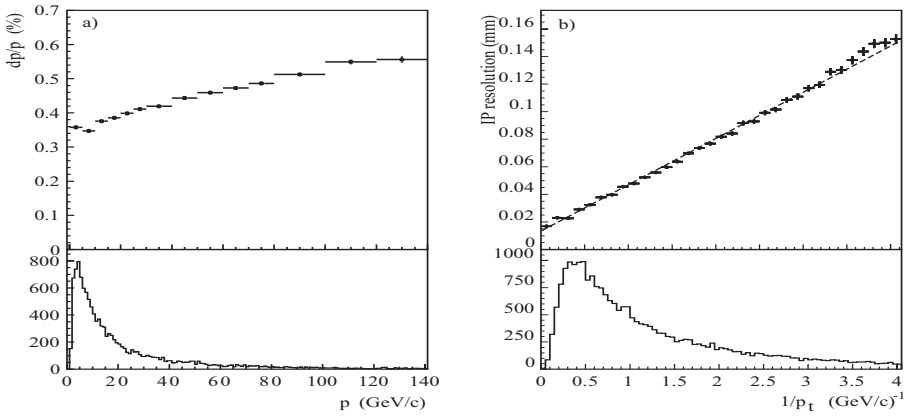

Figure 2.7: Resolutions on the reconstructed track: (a) momentum resolution as a function of track momentum showed in the lower histogram (b) impact parameter resolution at the production vertex of the track. For comparison, the $1/\mathrm{pT}$ spectra of B decay particles are shown in the lower part of the plots

2.3 The tracking system

The LHCb tracking system is based on the vertex locator and the tracking stations.
Excellent spatial resolution is required for the reconstruction of track direction and production vertices. For this reason, the vertex locator and the inner part of the tracking stations are designed with silicon technology. The outer part is equipped with straw–tubes.
The tracking system and the magnet are used to measure the momentum of the particles. For this purpose the VELO and one of the station are placed upstream and all the other stations are downstream the magnet. This configuration allows to calculate charged particle deflection due to the magnetic field. In the following section all these subdetectors will be presented.

2.3.1 The magnet

A dipole magnet [32–34] is used to measure the momentum of the charged particles from the curvature of their trajectories.
The magnetic field, up to 4 Tm, provides a full coverage of all the particles in the LHCb acceptance. The LHCb magnet is a warm resistive dipole designed with saddle–shaped coils placed mirror-symmetrically to each other in the magnet yoke, as shown in Fig. 2.8. The magnet is designed to generate a field in only one direction but with two polarities, positive and negative. The reversed field is used to study possible asymmetries in the detector, and systematics to be included in all the high–precision measurement.

2.3.2 The vertex locator

A fundamental requirement for the LHCb experiment is the high precision in the reconstruction of primary and secondary vertices of the b and c hadron decays, as shown as an example in Fig. 2.9. VELO [35] plays this important role.

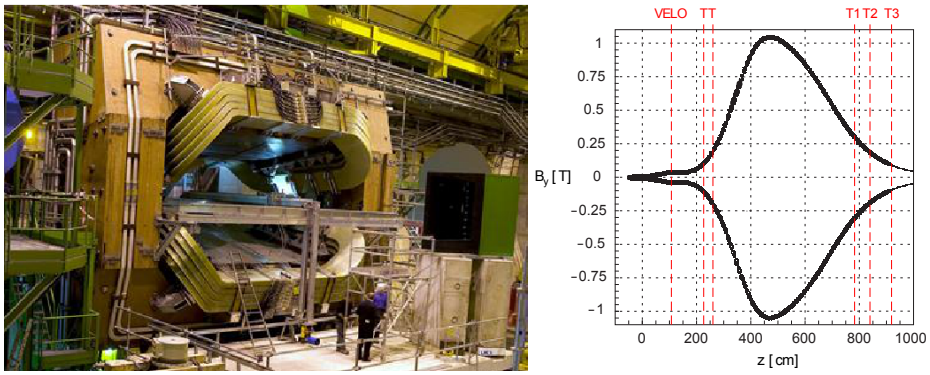

Figure 2.8: Right: magnet in place in the LHCb cavern. Left: Magnetic field map with some detector positions along z axis

It consist of a series of silicon modules placed around the interaction point as shown in Fig. 2.10. Some interesting parameters are listed in Tab. 2.1. It provides 3D coordinates of the vertices giving the r and ϕ coordinates along the beam (z) direction. A short track

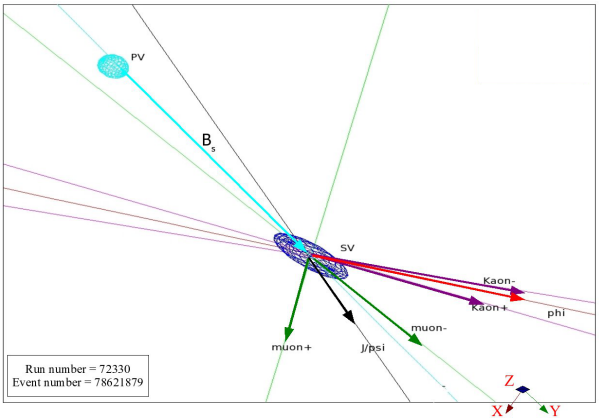

Figure 2.9: Reconstruction of a $B_s^0 \to J/\psi\phi$ decay from collision data. Primary and the secondary vertices are clearly well separated

extrapolation distance leads to a better impact parameter measurement. Therefore, the innermost radius of the sensors should be as small as possible. During physics running conditions, the RMS spread of the beams will be less than 100 μm, but for safety reasons, the closest approach allowed to the nominal beam axis is 5 mm due to the unknown closed-orbit variations of LHC beams. Furthermore, the repeatability of the beam positions could not be guaranteed, initially, to be better than a few millimeters. This imposed that the VELO detector to be mounted on a remote controllable positioning system, allowing adjustment in the x and y directions.
During injection the two detector halves are 3 cm away to avoid radiation damages.
At nominal conditions LHCb has, on average, one visible interaction per bunch crossing. For this reason the VELO has two other planes, placed backward and hardware identically to the others, used for the pile–up veto [36]. They are used to improve the performance and

	R sensor	ϕ-*sensor*
number of sensors	42 + 4 (VETO)	42
smallest pitch	40 μm	38 μm
largest pitch	102 μm	97 μm
inner (outer) radius of active area	8.2 (42) mm	8.2 (42) mm
angular coverage	182 deg	$\approx$ 182 deg
stereo angle	-	10-20 deg
ultra Vacuum Condition	10^{-8} mbar	
xy precision alignment	20 μm	
z precision alignment	100 μm	

Table 2.1: Technical parameters of the VELO sensors

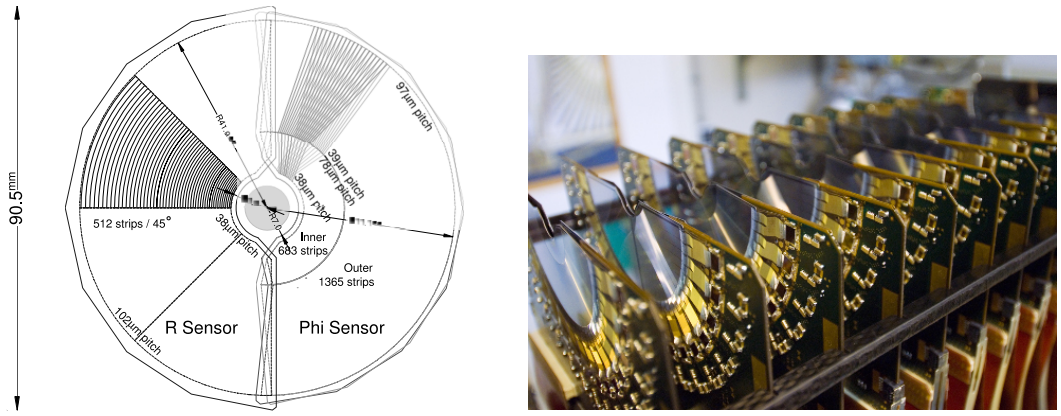

Figure 2.10: Left: technical design of the two pixel sensors in closed position. Right: picture of half size structure of the VELO box with all the sensors

to identify multi–interaction events.
VELO is also used to take decision at the L0 trigger level to accept or reject the event forcing its efficiency to be at least 99%. The readout chip [37, 38] was designed with a peak time and a sampling frequency respectively equal to the LHC crossing frequency of 40 MHz and with a readout of 1 MHz frequency of the L0 rate as requested [39]. All the layers, with the front–end electronics, are integrated in a vacuum vessel to reduce the possible beam–gas interactions that can occur.
This subdetector must detect all the particles inside the acceptance of the downstream detectors, with the highest precision, in the pseudorapidity region of $1.6 < |\eta| < 4.9$ and merging them from primary vertices in the range $|z| < 10.6$ cm. These tracks, inside the 300 mrad, cross in the VELO at least three stations and cover completely the azimuthal acceptance. To obtain the 3D coordinates there are two sensors: the *r* sensor provides the radial distance from the beam axis, the ϕ sensor provides the azimuthal angle coordinate around the beam and the z coordinate is provided by the position of each sensor plane, as shown in Fig 2.10. All the VELO sensors have a semi–circular shape and they must be perfectly aligned [40, 41], they are designed to resist for three years of LHC operations.

There are some possible sources of interference as the radio frequency picks up from the LHC beams, gas losses and the field generated by the bunch structure of the beams. To avoid these problems all the modules are separated by RF–foils.

2.3.3 The trackers

The second component of the tracking system is made by the tracking stations placed upstream and downstream the magnet.
The tracking stations are divided in three different subdetector designed and built with two different technologies:

→ Silicon tracker: Tracker Turicensis (TT)[1], located upstream the magnet covers all the LHCb acceptance, and Inner Tracker (IT) just behind the magnet surrounds the beam–pipe

→ Outer Tracker (OT): assembled with the IT in three T stations T_1, T_2 and T_3 downstream the magnet

The differences technologies are due to the necessity to have a good spatial resolution considering particle densities. Where the number of charged particles is high, silicon detectors were chosen. Drift–time tube were used to cover the remaining part of the acceptance, without loosing performance.

	TT	**IT**	**OT**
Width (m)	1.5	1.2	5.95
Height (m)	1.3	0.4	4.80
Diameter drift tube	⁄	⁄	4.9 mm
Drift time	⁄	⁄	<50 ns
Coordinate resolution[2]	200 μm		

Table 2.2: Technical parameters of the TT, IT and OT detectors

The silicon trackers

The Silicon Tracker (ST) [42, 43] is made up of TT and IT detectors. They have the same layout and are equipped with silicon micro–strip sensors working at 5°C. All the stations have four layers ($x-u-\nu-x$) with vertical strips in the first and the last layer, and strips rotated by a stereo angle of -5°and +5°in the second and the third layers. Some technical details are in Tab. 2.2.
These stations were designed and optimized considering the expected distributions of particles [44]. Some important parameters are the multiple scattering and the hit multiplicity. The density of the particles decreases from the beam–pipe zone to the external edge.

[1] TT is also known as Trigger Tracker
[2] the coordinate resolution in the TT and IT case represent the strip pitch

⇒ **Tracker Turicensis** [45, 46]*:* it is located between the first Cherenkov detector (RICH1) and the magnet. The symmetric drawing of the detector station consists of two halves shown in Fig. 2.11, one on each side of the LHC beam–pipe, divided in four layers. Each layer is also divided in two different pairs , (x,u) and (ν,x) to enable the reconstruction of three dimensional points previously described. The half stations are mounted on rails and can be retracted horizontally for detector maintenance.

⇒ **Inner Tracker** [47]*:* it is the innermost region of the T stations and is placed downstream the magnet and before the second Cherenkov detector (RICH2). It surrounds the beam–pipe with its four sectors. The bidimensional scheme and a three–dimensional reconstruction are shown in Fig. 2.12. Each sector is arranged in a cross shape configuration, overlapping in x, to avoid acceptance gaps and to facilitate the relative alignment. The four sectors are combined in group of two layers, top and bottom, A and C sides. The top and bottom parts consist of a single silicon sensor and a readout hybrid, otherwise A and C sides are equipped with two silicon sensors

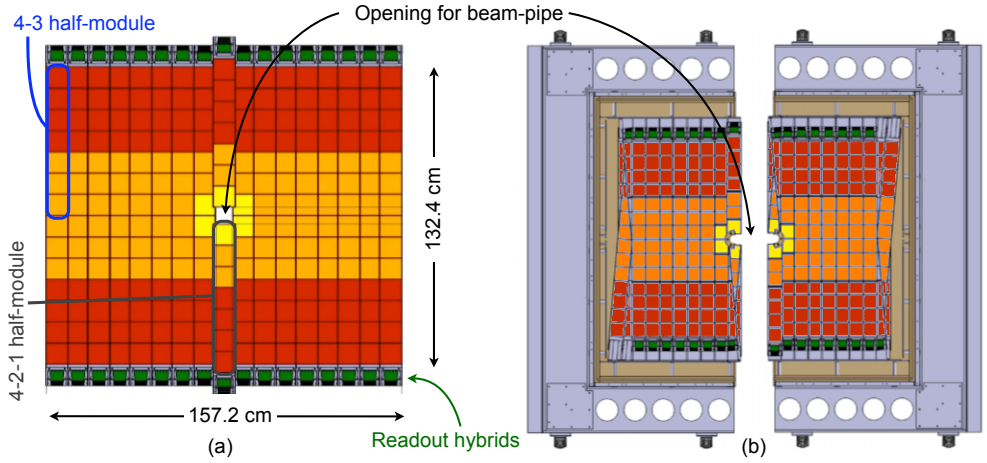

Figure 2.11: Trigger tracker layout. On the left: closed position of the tracker station. On the right: A and C side halves in the opened position, mounted on the external structure

The outer tracker

The external part of the tracking system is based on gas detectors. The Outer Tracker (OT) [48] is a drift–time detector equipped with straw–tubes. OT is made up of three stations placed downstream the magnet. All the stations have four layers ($x-u-\nu-x$) of monolayered straw–tubes. The geometry force to have the same structure of the ST Sect. (2.3.3) with x–layers vertically displaced and u and ν layers with a stereo angle of $\pm 5°$ with respect to the vertical, as shown in Fig. 2.13. The active volume is filled with a gas mixture of Argon (70%) and CO_2 (30%) to guarantee fast drift time and good space resolution [49–51]. Some technical parameters are reported in Tab. 2.2. Each station is divided into two segments A and C sides, mounted on a rail–lines that can be opened to access the inner part of the detector or the beam–pipe.

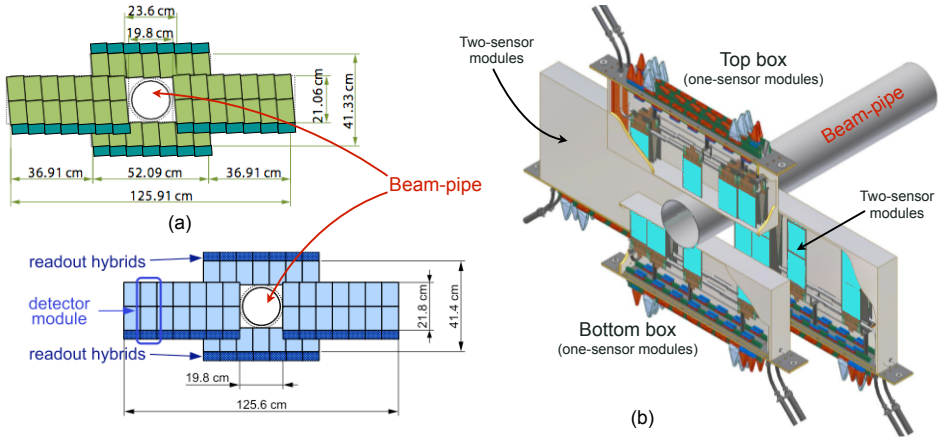

Figure 2.12: Inner tracker layout. On the left: 2–D u, v (top) and x (bottom) layer layout. On the right: 3–D layout of the inner tracker around the beam–pipe

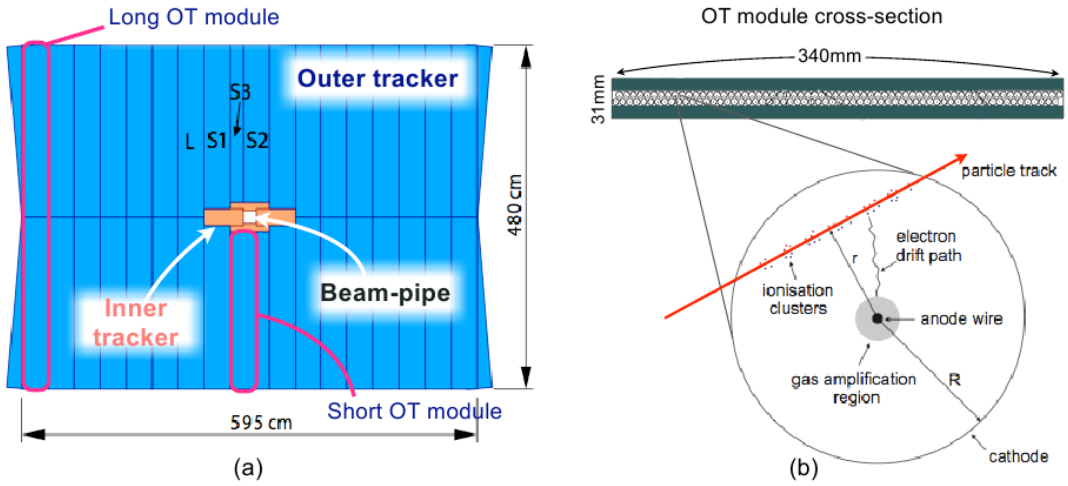

Figure 2.13: (a) outer tracker layout in closed position. (b) straw–tube structure and zoom on the particle interaction in the detector

2.4 Particle Identification

Particle identification is one of the most important aspects needed for the study of the rare decays. It is mandatory to identify all particles in the final states to distinguish signal from background.

A correct identification is obtained considering and combining different subdetector information. Different technologies are used. An example is the electron identification, in which case the main important subdetector is the electromagnetic calorimeter, but combining information with tracking and RICH it is possible to maximize the identification efficiency.

The hadron identification is provided by two stations of Ring Imaging CHerenchov (RICH) counters. These detectors, described in details in the following chapter, cover a wide mo-

mentum range (2–100 GeV/c). Cherenkov radiation is emitted in a cone when a charged particle passes through a radiator material with a velocity that is greater than the speed of light in that medium. The polar angle, at which this light is emitted, is reconstructed by photon detectors and combined with momentum information from the tracking system to calculate the mass of the particle. Two examples of RICH event are reported in Fig. 2.14 with MonteCarlo simulation and in Fig. 2.15 with data at $\sqrt{s} = 450$ GeV. In these figures reconstructed rings are superimposed to detected hits, one for each mass hypothesis. Par-

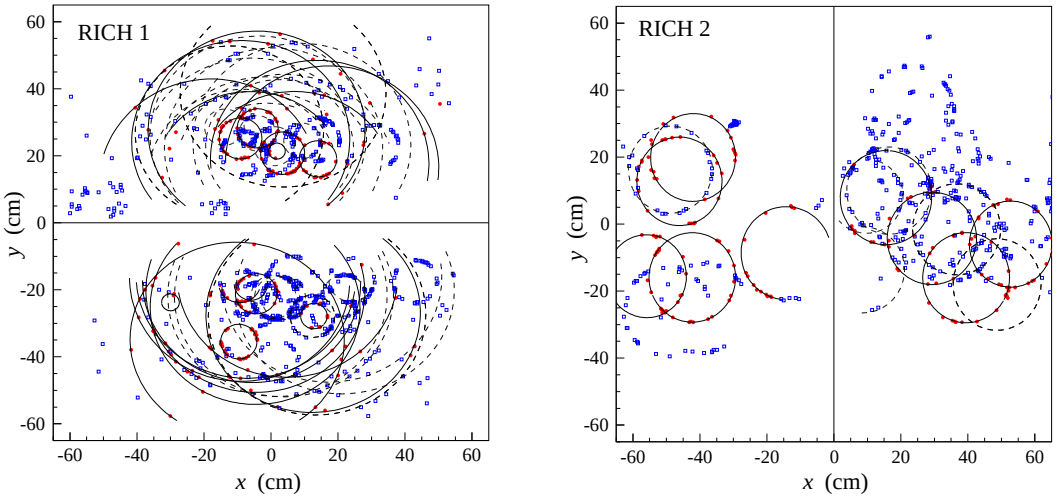

Figure 2.14: Event display of the detected photoelectrons for a typical event in RICH1 (left) and RICH2 (right) obtained with MonteCarlo data. The two detector plane halves are drawn next to each other, and fitted rings are superimposed, indicated by solid lines for rings from long tracks and dashed lines for other tracks

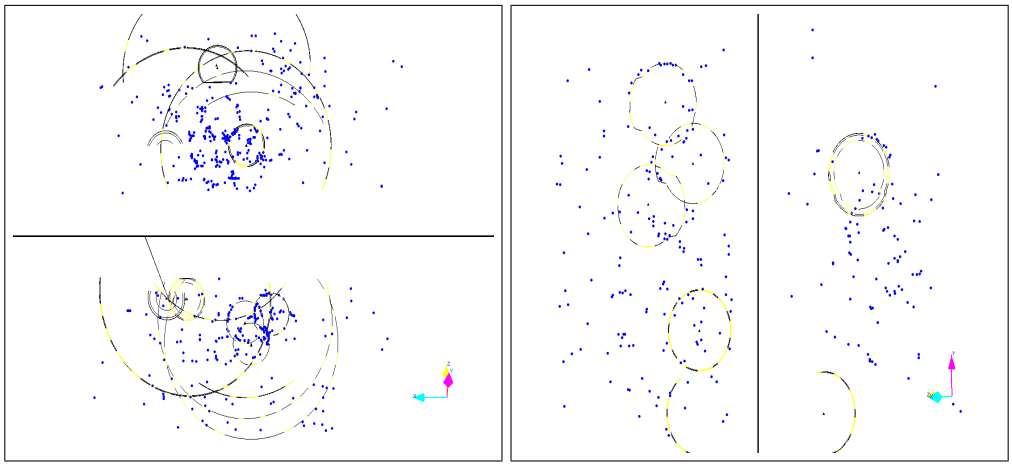

Figure 2.15: Event display of detected photoelectrons, for one of the first pp collision $\sqrt{s} =$ 450 GeV. There are superimposed the reconstructed rings for different mass particle hypothesis. In the RICH1 detector, on the left, rings detected have two different radii because of the two different radiators

ticle identification is performed considering the pattern of hit pixels. It is compared to the

expected pattern under a given mass hypothesis for the reconstructed tracks crossing the detectors. From this comparison a likelihood is maximized varying of the particle mass hypothesis.
The performance was studied, with MonteCarlo events, considering several decay channels. The log–likelihood ratio is calculated assuming pion and kaon mass hypothesis:

$$\Delta \ln \mathcal{L}_{K\pi} = \ln \mathcal{L}(K) - \ln \mathcal{L}(\pi) = \ln \frac{\mathcal{L}(K)}{\mathcal{L}(\pi)} \tag{2.1}$$

This relation describes the significance of π/K separation. Varying the $\ln \mathcal{L}$ cut used to K separation, the misidentification rate can be reduced improving the purity of the selected sample at the cost of reduction of the K identification efficiency. There is the possibility to change the cuts for the π/K selection. This is possible offline, depending on the analysis to be done.
The lepton identification is performed using information from more than one subdetector and the most important are calorimeters and muon chambers. For the electron identification the delta likelihood $\Delta\mathcal{L}$ is the calorimeter difference between electron and background hypothesis. Muon are identified using the muon system considering the difference between the muon and the non–muon hypothesis.
The final likelihoods are combined from the various detectors:

$$\mathcal{L}(\mathrm{e}) = \mathcal{L}^{RICH}(\mathrm{e})\mathcal{L}^{CALO}(\mathrm{e})\mathcal{L}^{MUON}(\mathrm{non}\mu) \tag{2.2}$$

$$\mathcal{L}(\mu) = \mathcal{L}^{RICH}(\mu)\mathcal{L}^{CALO}(\mathrm{non\ e})\mathcal{L}^{MUON}(\mu) \tag{2.3}$$

$$\mathcal{L}(\mathrm{h}) = \mathcal{L}^{RICH}(\mathrm{h})\mathcal{L}^{CALO}(\mathrm{non\ e})\mathcal{L}^{MUON}(\mathrm{non}\mu) \tag{2.4}$$

where h is an hadron. If there is more than one candidate for the same detector, the combination is the product of all the likelihood.
All the subdetectors involved in the particle identification will be described in the following sections.

The electrons

The electromagnetic calorimeter Sect. (2.5.3) is the most important detector for the electron and photon identification.
The identification algorithm combines the ECAL and the tracking system information. It considers the energy of the charged cluster detected by the calorimeter. The reconstruction system consider the comparison between the energy released and the reconstructed track direction and momentum.
The reconstruction algorithm starts with the identification of the prompt electrons. Charged particles release energy traversing materials but electrons have an high probability to loose part of the energy in the material by bremsstrahlung effect.
The material budget before the magnet is not too big. It is possible to estimate the bremsstrahlung effect studying cluster positions. The bremsstrahlung photons are directly correlated with the direction of the electron parent. The electrons deviate from their original trajectory for the bending magnetic field. A schematic description is shown in Fig. 2.16. When the two cluster are correctly reconstructed the real initial energy of the electron is obtained summing the two energies of the clusters detected if the effect happens after the magnet. The

bremsstrahlung photons emitted after the magnet cannot be identified as different clusters from the electron.

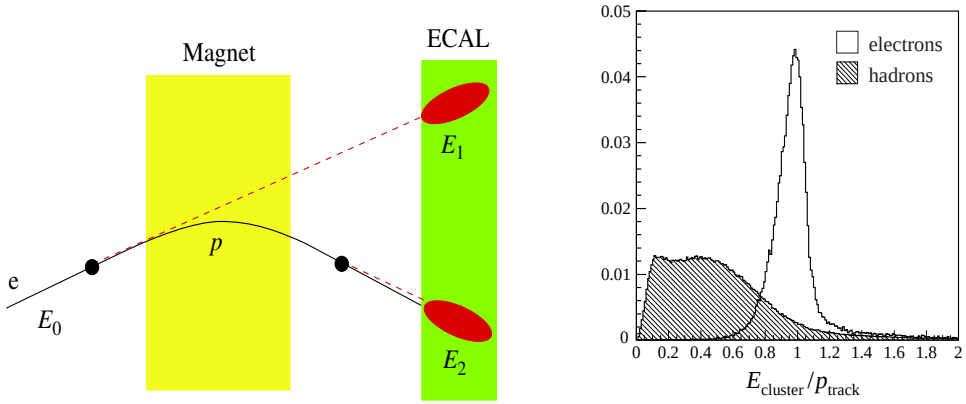

Figure 2.16: Left: illustration of the electron identification considering bremsstrahlung correction. The two clusters represent the showers detected by the ECAL coming from the same original trajectory of the electron. The second cluster detected is the bended electron itself. Right: histogram of the cluster energy over the momentum of the reconstructed track for electrons and hadrons

The photons

Photon reconstruction uses the same algorithm described previously for the electrons, but in this case the ECAL cluster is not associated to any track. All these clusters are considered photon candidates. The algorithm is optimized considering material before the ECAL and the shape of the electromagnetic shower. Longitudinal and transversal dimensions are considered to calculate the energy of the photon.

The neutral pions

Neutral pion reconstruction is another aspect to be considered. This particle decays into 2 photons and the ECAL detector plays again the most important role in its identification.
There are two different approaches, depending on the energy of the π^0.
First of all neutral pions are divided into two groups: resolved and merged π^0 in Fig 2.17.

→ **Resolved π^0:** they are pions with a 200 MeV/c$< p_T <$ 3 GeV/c. The lower limit is set because only particles with $pt >$ 200 MeV/c reach the calorimeters. These particles are mostly reconstructed as a resolved pair of well separated photons. As shown in Fig. 2.17 there is the peak of the combined photons at the π_0 mass due γ combinatorial background.

→ **Merged π^0:** they have transversal momentum larger than 3 GeV/c and the two photons cannot be separated. The identification algorithm is able to disentangle potential pair of photons merged in a single cluster. The energy of each cell of the cluster is shared between two virtual sub–clusters according to an iterative procedure based on

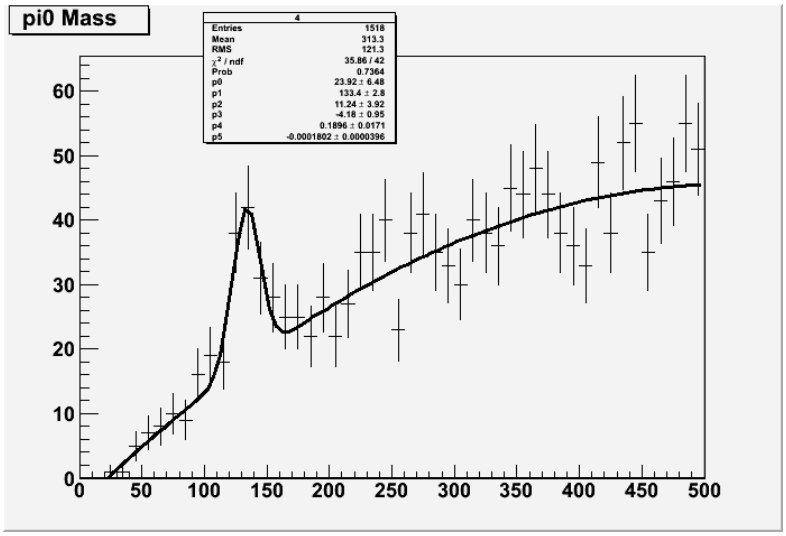

Figure 2.17: Reconstruction of the π_0 performed with first data at $\sqrt{s} = 450$ GeV. On the x axis there is the mass $M_{\gamma\gamma}$ in MeV

the expected transverse shape of photon showers. Each of the two sub-clusters is then reconstructed as coming from a photon, as for isolated photons.

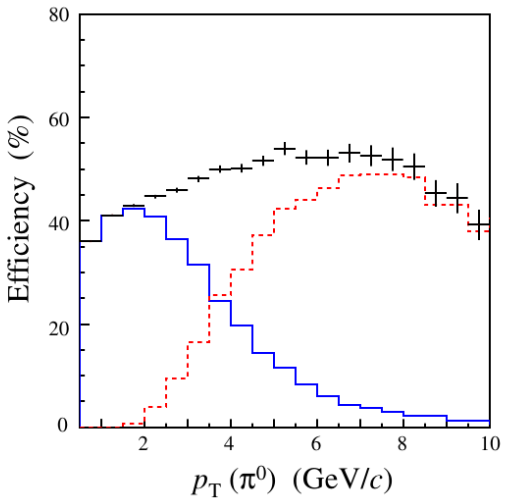

Figure 2.18: Reconstruction efficiency of the π^0 inside the geometrical acceptance of the LHCb experiment. the solid blue line is the contribution of the resolved π^0, the red dashed line represent the merged contribution. Cross points are the overall efficiency for all the transversal momentum range

The total neutral pion identification efficiency is described in the Fig. 2.18. There are the separated efficiencies of the two categories and, in black, the sum of the two different contributions.

The muon identification

In several final states of B–meson decays, like the flavor changing neutral current decay $B_s \to \mu^+\mu^-$ or the *golden channels* $B_d^0 \to J/\psi(\mu^+\mu^-)K_s^0$ and $B_s^0 \to J/\psi(\mu^+\mu^-)\phi$, there are muons. The muon system is fundamental. It is part of the LHCb trigger system providing a fast response for the highest p_T muons in the event for the L0 trigger and a muon identification for the HLT level.
These particles weakly interact with the material. For this reason the muon stations are placed at the end of the spectrometer. They are made up by absorber and active planes where muons leave tracks. To identify the particle as a muon candidate, two stations must have hits in the direction of the hypothetical track.
The efficiency calculated, as a function of the particle momenta, is a flat distribution with an average value around $\sim 94\%$ for p$>$ 10 GeV/c as shown in Fig. 2.19. Discriminating variables, helping to improve the muon selection purity, are constructed from the comparison of slopes in the muon system and the main tracker.

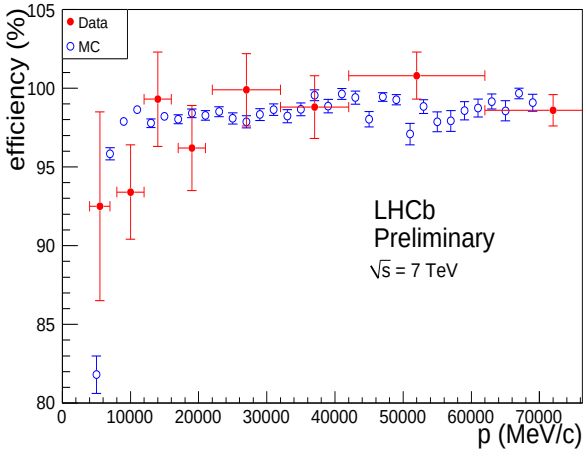

Figure 2.19: Comparison of the muon identification efficiency, using J/ψ, with MonteCarlo estimates as a function of the momentum of the muon

2.5 The calorimetry System

The calorimetry system made by an Electromagnetic CALorimeter (ECAL) and an Hadron CALorimeter (HCAL) [52] is used for the identification of neutral particles. They are part of the LHCb trigger [53, 54] where a readout electronics must be very fast and reliable. In the L0 trigger the energy deposited by the electrons are of the variables used to take the decision.
The system was designed to be able to identify photons, electrons and hadrons, detecting the transverse energy (E_T) released, and their spatial coordinate.
Each subdetector ECAL and HCAL is designed to select specific particle types based on their material interactions shown in Fig. 2.3.

The way to reconstruct and identify particles in the calorimeters is to estimate the energy lost traversing their material. The structure is from consecutive elements: Scintillator Pad Detector (SPD), PreShower detector (PS), Electromagnetic CALorimeter (ECAL) and Hadron CALorimeter (HCAL). Some of the parameters of these subdetectors are listed in Tab. 2.3.
All the energy transferred to the scintillator is converted in light collected by PMTs. The hit density varies by two orders of magnitude all over the surface. ECAL, SPD and PS, are divided in three cells labeled as inner, middle and outer. HCAL is segmented into two zones with larger cell size for the bigger dimensions of the hadronic showers, compared to ECAL. All the modules are divided in two halves moving on rails (A and C sides), the two parts can be easily opened to access the beam pipe.

	ECAL	*HCAL*	*PS/SPD*
radiation length (X_0)	25	5.6	2.5
wide (m)	7.76	6.8	7.6
high (m)	6.3	8.4	6.2

Table 2.3: Calorimetric system parameters

2.5.1 The scintillator pad detector

The first station of the calorimetry system is the Scintillator Pad Detector (SPD) [55] needed separate charged particles. It is used to distinguish between signals in the calorimeter associated to charged particles and those which are associated to neutral particles.

2.5.2 The preshower detector

The PreShower detector (PS) [55, 56] is the following station with small lead thickness used to reconstruct the starting point of the electromagnetic showers. It identifies electrons, rejecting the charged pion background. This detector has the same technology of the SPD equipped with PMTs[3] [57–59]. One of the main purposes for the electron identification, is the identification of the large background from charged pions. While a charged pion will interact minimally with the lead sheet, an electron passing through the lead will produce a shower of many secondary particles.

2.5.3 The electromagnetic calorimeter

ECAL [60] is the subdetector for photons and electrons identification. It is 12.5 m far away from the interaction point and it covers the acceptance of LHCb, but has a limitation at small polar angles. Near the beam–pipe, in the high particle density zone, there is an hole of 2.5 mrad not covered by the detector to avoid radiation problems due to the high particle flux.

[3] R5900-M64 manufactured by HAMAMATSU Photonis

Every module composing the entire system is made alternating a lead layer of scintillator tiles. The 66 layers of lead and scintillators compose the ECAL wall with 25 X_0. The light is collected by PMTs[4] [61]. After the simulations, these subdetectors were optimized with cosmic rays [62] and the energy resolution obtained is:

$$\frac{\sigma_E}{E}_{ECAL} = \frac{8.5\% < a < 9.5\%}{\sqrt{E}} \oplus 0.8\% \tag{2.5}$$

where the first term a stands for photoelectron statistics, called stochastic term and the second term represents the electronics noise, E is in GeV.

2.5.4 The hadronic calorimeter

The Hadronic CALorimiter (HCAL) [63] detects hadrons of high energies. It is a sampling calorimeter obtained combining an iron absorber layer with an active layer equipped with scintillating material.
Also in this case the energy resolution was checked during the commissioning phase with cosmic rays [62], and it is:

$$\frac{\sigma_E}{E}_{HCAL} = \frac{(69 \pm 5)\%}{\sqrt{E}} \oplus (9 \pm 2)\% \tag{2.6}$$

2.6 The muon system

Tracks traversing all the LHCb spectrometer are detected and identified as muon by the muon system [64–66].
It consists of five rectangular stations (M1–M5), M1 placed upstream and M2–M5 downstream the calorimeters. The system has detector planes or "stations" interleaved with iron absorber planes to obtain a total radiation length of about $X_0 \sim 20$. All the stations are divided in four regions placed at increasing distance from the beam axis. They are proportionally segmented in a way to have all the region covered by the same occupancy. This means that in the farest region from the beam axis, the spatial resolution is lower than near the beam–pipe, but the impact of the multiple scattering at large angles became relevant and an high resolution is less relevant.
All the stations cover the whole LHCb acceptance. They are able to provide spatial coordinates and transverse momentum of the traversing particles. The existence of the station M1 is required to improve the p_T resolution for the trigger decision [67].
The muon system is part of the trigger and the stations M1–M3 have an high granularity in the bending plane (x coordinate). This characteristic gives a 20% resolution for the muon candidates inside the LHCb acceptance. M4 and M5 are the last two stations, with a lower spatial resolution, used for the identification of the most penetrating particles.
All the downstream stations and the outer regions of the M1 station are equipped with Multi–Wire Proportional Chambers (MWPC) [68–70]. The M1 inner region uses triple–GEM (Gas Electron Multiplier) [71, 72] to limit aging problem due to the high particle

[4] R7899-20 manufactured by HAMAMATSU Photonis

Figure 2.20: Picture of muon system in the experimental area

flux. The gas mixtures were chosen to optimize the resolution and the velocity of the signal, for the MWPC the mixture is Ar (40%), CO_2 (55%) and CF_4 (5%). The same mixture, but with different percentage Ar (45%), CO_2 (15%) and CF_4 (40%) is used in the case of the GEM chambers.
Only tracks with momentum greater than 3 GeV/c reach the muon stations, and only particles with momentum greater than 6 GeV/c pass trough all the five stations.
As most of the other subdetectors, the muon stations are divided in two sides adjusted on rails that can be opened. They must be aligned to obtain the request $\sim$ 1 mm spatial resolution for the inner region of M1.
All the system was optimized using data obtained during test beam made with prototypes or using cosmic rays [73, 74] collected during the commissioning phase.

Active area	435 m^2	
Iron wall wide	80 cm	
	Bending	*not Bending*
Inner angular acceptance	20	16
Outer angular acceptance	306	258

Table 2.4: Technical parameters of the muon stations

2.7 The online and data acquisition systems

All the data coming from the detector and all the working condition parameters of the machine and of the experimental area must be transferred and synchronized to a permanent storage. All these tasks are made by the online system [75–77].
To fulfill these requests the online system is divided into three parts:

→ **Data AcQuisition system (DAQ):** it transfers all the events, selected by the trigger, from the front–end electronics to the permanent storage.

→ **Timing and Fast Control (TFC):** it checks the clock of all the system. It is the distributor of the beam–synchronous clock during the data transfer.

→ **Experiment Control System (ECS):** it controls the status of LHCb: detectors, working conditions (gas, temperature, voltages), LHC machine conditions, trigger, DAQ and TFC. All the controls made are registered to be simply checked by the user using PVSS II software [5]

The data obtained from the detector are analyzed by the users. Data are reconstructed and written on tape using the distributed computing technologies (GRID) [78].

[5]PVSS® is a SCADA (Supervisory Control And Data Acquisition) commercial system

CHAPTER 3

THE LHCb RICH DETECTORS AND THE HIGH VOLTAGE SYSTEM

Particle identification is a fundamental requirement of LHCb and the methods used are described in the previous chapter. Calorimeters, muon and two Ring Imaging CHerenkov (RICH) counters are the detectors involved. Calorimeter and muon detectors participate in the identification of leptons, photons and hadrons, but the fundamental π / K / p separation which is essential for the physics program of the LHCb experiment is carried out by the RICH detectors.
In the first part of this chapter a concise description of the Cherenkov effect and the system architecture are given, with a section dedicated to the high voltage distribution system, and the study of the performance with first data of the RICH detectors. In the second part there is the analysis and the optimization study done for the high voltage distribution system, necessary to assure good stability of the detector during data taking.

3.1 The Cherenkov effect

Charged particles traversing a material with a velocity greater than the velocity of the light in that material can emit photons. This phenomenon is called Cherenkov effect [79, 80].
Photons are created through the constructive interference of electromagnetic waves due to the interactions of the particle with the atoms or molecules of the medium. Their emission is in a cone along the trajectory of the particle. The emission angle, called Cherenkov angle θ_c is related to the speed of light v_l and to the speed of the particle v_p in that medium with the following relation:

$$\cos\theta_c = \frac{1}{n(E_\gamma)\beta} \tag{3.1}$$

were $n = c/v_l$ is the index of refraction, E_γ is the energy of the emitted photon, $\beta = v_p/c$ and c is the velocity of the light in the vacuum. The Cherenkov effect has a threshold, it appears when the charged particle speed is above a certain threshold given by $|\cos(\theta_C)| \leq 1$ which correspond to a threshold velocity of $\beta_{thr} = 1/n$. The Lorentz boost factor related to this

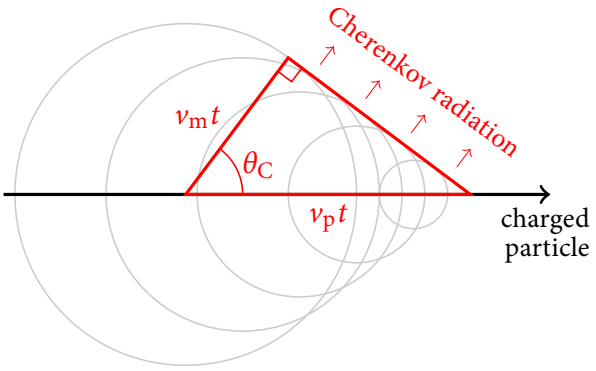

Figure 3.1: Geometrical description of the Cherenkov effect. The cones with the electromagnetic waves orthogonal to the wavefront of the Cherenkov radiation are sketched

condition is $\gamma_{thr} = 1/\sqrt{(1-1/n^2)}$. There is also a limit, the maximum Cherenkov angle due to particles with $\beta = 1$ corresponding to $V_p = c$ and $m_p = 0$. This value of β correspond to $\theta_c^{Max} = \arccos(1/n)$ and angles corresponding to charged particles with that speed are considered saturated.
The detection of the emitted photons and the following Cherenkov angle reconstruction are used to obtain the velocity of the particle. Combining the measured velocity of the particle with its momentum, independently measured by the tracking detectors in the magnetic field, the mass of the particle, can then be extracted:

$$\begin{aligned} p &= m\gamma\beta c \\ &= mc\frac{\beta}{\sqrt{1-\beta^2}} \end{aligned} \tag{3.2}$$

In the RICH detector a fundamental requirement is the spatial reconstruction of the photons. It is needed for the reconstruction of the Cherenkov angle. Another useful information is the knowledge of the number of photons produced by the charged particle in a given material. The photon radiated energy per unit of material is:

$$\frac{dE}{dx} = 2\pi\alpha z^2 \int_{\beta n>1} \left(1 - \frac{1}{\beta^2 n^2}\right) \frac{d\lambda}{\lambda^2} \tag{3.3}$$

with $\alpha = 1/137$ the fine structure constant and z the charge of the interacting particle. A natural cut–off exists for all the dielectric media due to the plasma state. For all the frequencies greater than the cut–off frequency, the value of the index of refraction is always lower than unit and the Cherenkov threshold cannot be satisfied by any physical particle. From Eq. 3.3 the number of photon created, per unit path length of a particle with charge ze and per unit energy of the photon is:

$$\begin{aligned} \frac{d^2N}{dE_\gamma dx} &= \frac{\alpha z^2}{\hbar c}\sin^2\theta_c \\ &\approx 370\,\sin^2\theta_c(E_\gamma)\,eV^{-1}cm^{-1} \qquad (z=1) \end{aligned} \tag{3.4}$$

Material		**Aerogel**	$\mathbf{C_4F_{10}}$	$\mathbf{CF_4}$
L	cm	5	85	167
n		1.03	1.0014	1.0005
θ_C^{max}	mrad	242	53	32
$p_{th}(\pi)$	GeV/c	0.6	2.6	4.4
$p_{th}(K)$	GeV/c	2.0	9.3	15.6
$\sigma_\theta^{emission}$	mrad	0.4	0.8	0.2
$\sigma_\theta^{chromatic}$	mrad	2.1	0.9	0.5
σ_θ^{pixel}	mrad	0.5	0.6	0.2
σ_θ^{trk}	mrad	0.4	0.4	0.4
σ_θ^{total}	mrad	2.6	1.5	0.7
$\mathcal{N}$		6.8	31.0	23.0

Table 3.1: Physical parameters of the radiators used in the RICH systems and the different contributions to the resolution determined from the simulation. The total resolution per photoelectron and the mean number of detected photoelectrons in the ring image are also reported

or equivalently:

$$\frac{d^2N}{dxd\lambda} = \frac{2\pi\alpha z^2}{\lambda^2}\left(1-\frac{1}{\beta^2 n^2(\lambda)}\right) \tag{3.5}$$

3.2 The RICH detectors at LHCb

The Cherenkov effect is a powerful phenomenon to identify charged particles, even if it is a weak source of photons. For this reason the radiator choice is an important aspect to be considered.
All the physical characteristics of the radiators chosen for the LHCb experiment, are listed in Tab. 3.1. In Fig. 3.2 Cherenkov angles are plotted as a function of the momentum for different particles and radiators. These plots chosen the different momentum ranges where the radiators are actively involved in particle identification.
The RICH geometry [81–84] includes spherical mirrors [85] to focus parallel rays on the same point in the focal plane and to create also Cherenkov rings. The optical layout [86] includes also flat mirrors, needed to deflect all the photons outside the LHCb acceptance to the photon detection plane and to reduce detector radiation length seen by the produced particles.
The number of photons expected per charged particle for a given radiator material of length L can be deduced from the Eq. 3.3 and it can be written as:

$$\mathcal{N} = \left(\frac{\alpha}{\hbar c}\right) L\varepsilon_A \int TRQ\sin^2\theta_C dE = \mathcal{N}_0 L\sin^2\theta_C \tag{3.6}$$

where is ε_A the fraction of the active area of the photon detector, T the transparency of the radiator and of the quartz windows, R the mirror reflectivity, Q the quantum efficiency of the photon detectors and $\mathcal{N}_0$ is the figure of merit of the detector.

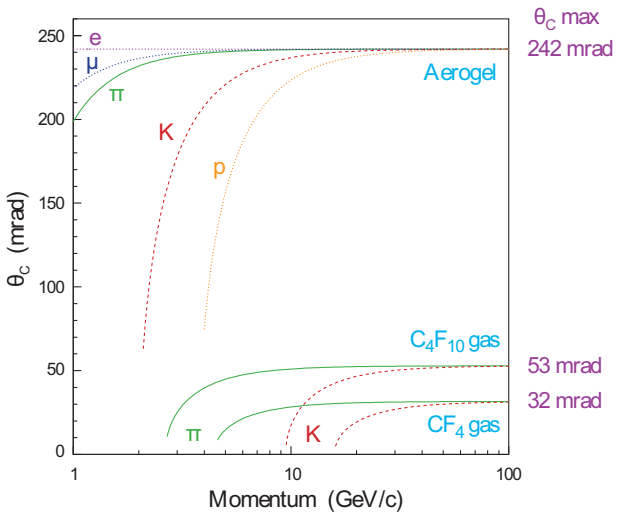

Figure 3.2: Cherenkov angle as a function of the particle momentum for μ, e, K, p and π, for the three different radiator materials used at LHCb

The expected number of photons for each radiator at LHCb is listed in Tab. 3.1.
The reconstruction of the velocity of the particle is evaluated starting from the θ_C angle reconstruction and from Eq. 3.1 and the resolution for a charged particle is:

$$\frac{\sigma_\beta}{\beta} = \frac{\sigma_{\theta_C}}{\sqrt{\mathcal{N}}} \tan(\theta_C) \tag{3.7}$$

σ_{θ_C} is the uncertainty on the emission angle per detected photons ($\mathcal{N}$).
The separating power between two particles of masses m_1 and m_2 at a given momentum p is:

$$\frac{\Delta\beta}{\beta} \simeq \frac{m_1^2 - m_2^2}{2p^2} \tag{3.8}$$

The resolution on the reconstructed Cherenkov angle has four main contributions to be considered:

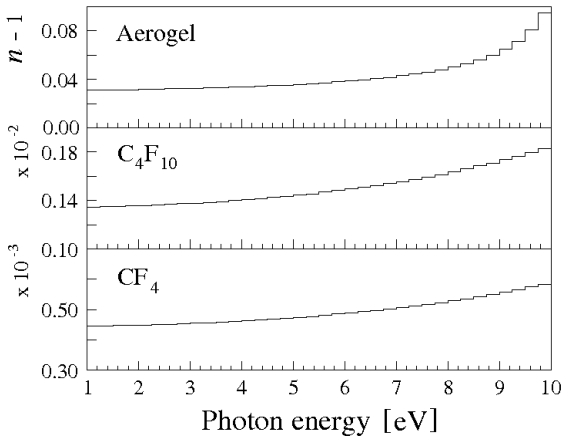

Figure 3.3: Chromatic dispersion distribution for the three radiator materials of the RICH detectors

→ $\sigma_{chromatic}$: the chromatic dispersion due to the dependence of the index of refraction of the radiator from the energy of the emitted photons. In Fig. 3.3 there are the three distributions of the index of refraction as a function of the photon energy for the three RICH radiators

→ σ_{mirror}: misalignment of the optical system and imperfections on the reflecting surfaces

→ σ_{pixel}: it is related to the finite granularity of the photon detectors (in general dictated by costs and number of channels in the readout system)

→ σ_{trk}: multiple scattering in the radiator and errors in the reconstructed track parameters

→ $\sigma_{emission}$: the finite length of the radiator material. Cherenkov photons are emitted all along the particle trajectory in the radiator, but they are assumed to be produced in the middle of the radiator

All these contributions are independent and generally added in quadrature as shown in Eq. 3.9:

$$\sigma_{\theta_C} = \sqrt{\sigma^2_{chromatic} + \sigma^2_{mirror} + \sigma^2_{pixel} + \sigma^2_{trk} + \sigma^2_{emission}} \tag{3.9}$$

Fig. 3.4 shows the correlation between momentum and polar angle of the produced particles. Two RICH detectors (called RICH 1 and RICH 2) were designed to cover the full momentum range 2–100 GeV/c.
The RICH 1 [87] is the detector upstream the magnet, placed between the VELO and the

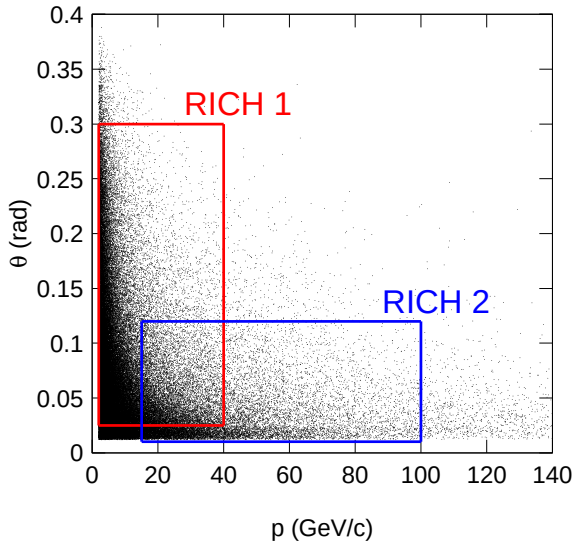

Figure 3.4: Polar angle as a function of the momentum of the incident charged particle. The two rectangles show the covered zones by the two RICH detectors

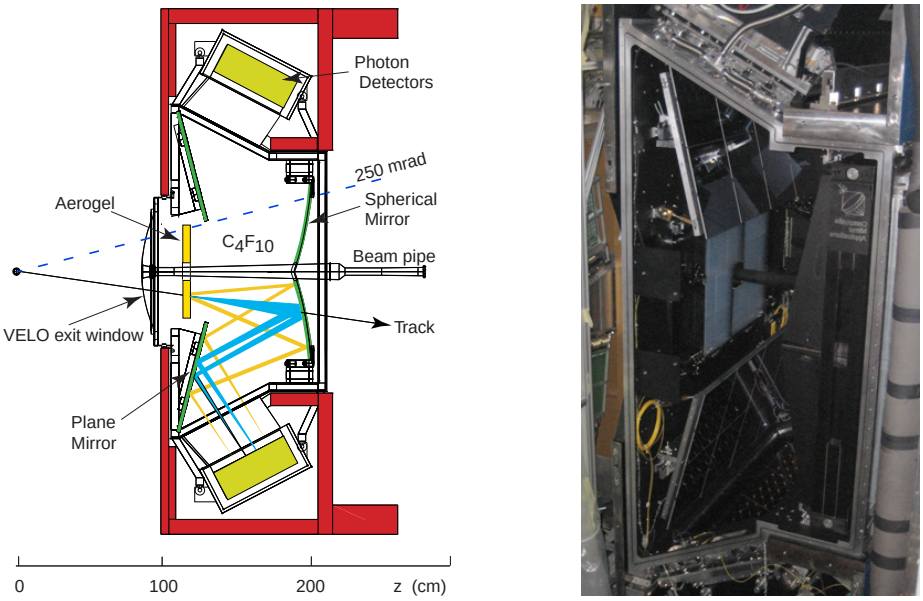

(a) (b)

Figure 3.5: Sketch of the RICH 1 detector. 3.5a is the RICH 1 design and 3.5b is the picture of the detector during the installation. In this picture is clearly visible the aerogel tiles inside the gas box, the 2 mirror planes and one of the two sides of the HPD photodetector planes

Trigger Tracker. It covers the lowest momentum range between 2 GeV/c and 40 GeV/c. Two radiator materials are used to cover this momentum range: solid silica aerogel (SiO_2) [88–93] of 5 cm thickness covers the momentum range 2–10 GeV/c. A gas radiator, 3.5 m^3 of per–fluorubutane C_4F_{10} [94, 95], is used for particles from 10 GeV/c up to 40 GeV/c. The detector structure is shown in Fig. 3.5. It covers the geometrical angular acceptance from $\pm$ 25 mrad to $\pm$300 mrad (horizontal) and $\pm$250 mrad (vertical). The gas enclosure has a quartz windows to separate the gas (at atmospheric pressure) from the photon detector plane.

The second detector, RICH 2 [96], is placed downstream the magnet, between the tracker and the first muon station. It covers the momentum range from $\sim$15 GeV/c up to 100 GeV/c using 95 m^3 of gaseous CF_4 radiator [94, 95]. As shown in Fig. 3.4 the highest momentum particles are produced at low polar angle. This feature is the main reason for the limited angular acceptance of $\sim \pm$15 mrad to $\pm$120 mrad (horizontal) and $\pm$100 mrad (vertical) of the RICH 2.

3.2.1 The RICH performance

As described before, the two RICH detectors have the same basic layout. The only difference is that RICH 1 is vertically oriented, while RICH 2 is horizontally oriented. In both cases photons are deflected and focused onto the photondetection plane placed outside the spectrometer acceptance, to limit material budget.

The two detectors are operational and preliminary data show the performance and the reliability of the system.

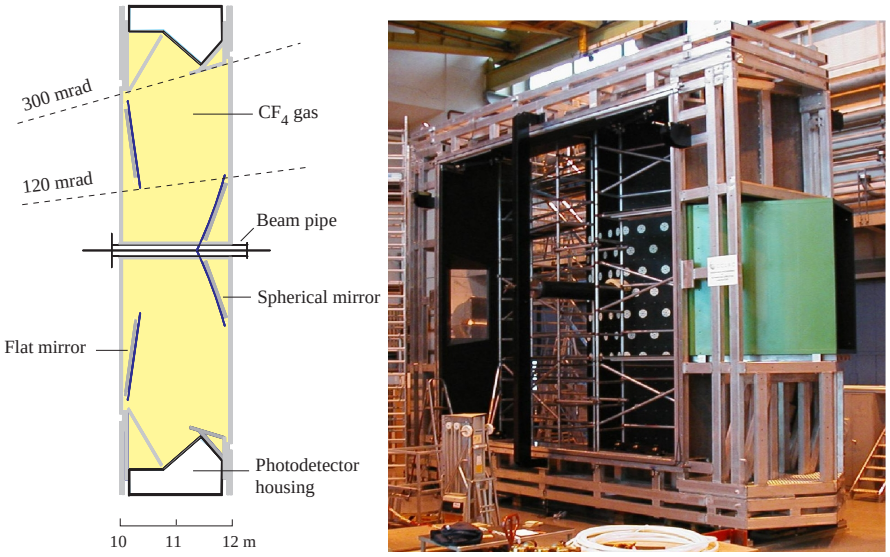

Figure 3.6: Sketch of the upper section, on the left, and picture of the RICH2 before the installation in the experimental area

The efficiency for the π/K separation obtained with data are shown in Fig 3.7, as a function of the particle momentum. A clear example of good and useful particle identification is shown in Fig. 3.8. The plots show the ϕ mass reconstruction obtained considering only the tracking system (Fig. 3.8a) and using also RICH information (Fig. 3.8b and Fig. 3.8c). The last plot the improvement obtained in resolution with the larger statistics available than at $\sqrt{s} = 7$ GeV.

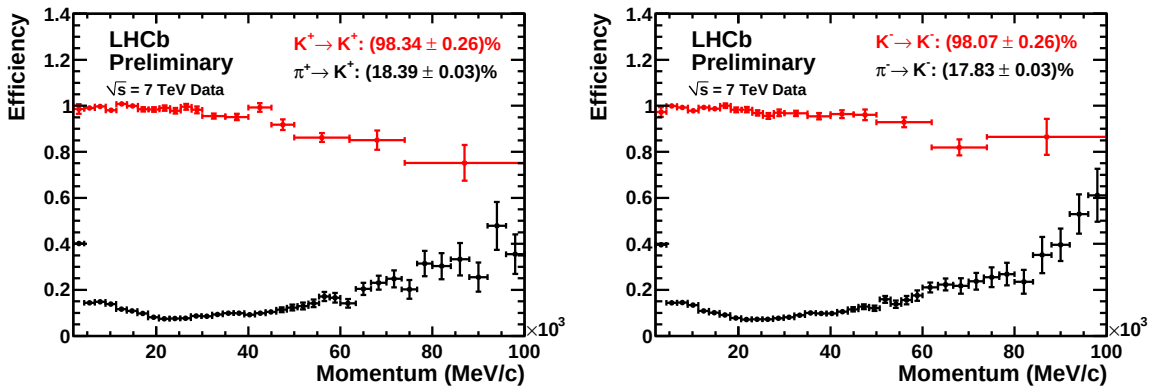

Figure 3.7: Efficiency plot for the π/K separation obtained with data at 7 TeV obtained with an integrated luminosity of $L \sim 14$ nb^{-1} for positive (on the left) and negative (on the right) particles

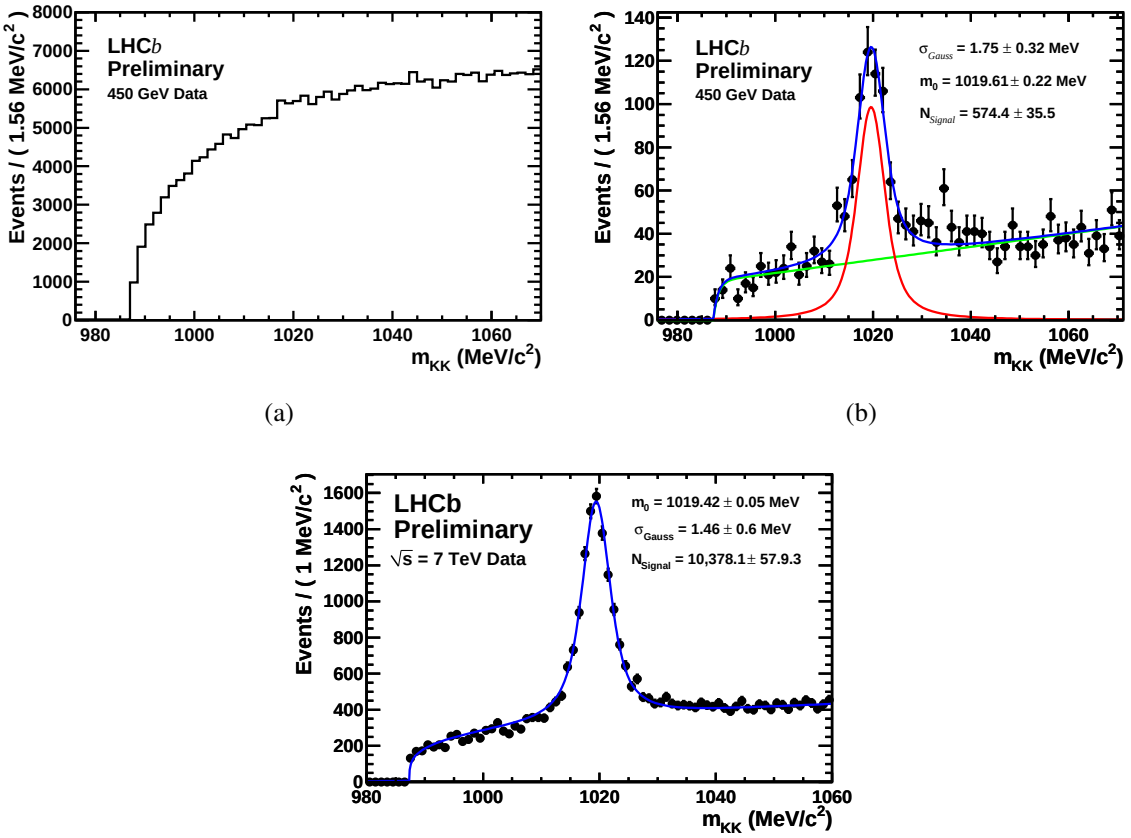

Figure 3.8: Invariant mass of the $\phi(1020) \rightarrow K^+K^-$ with only tracking information (Fig. 3.8a), and considering RICH information (Fig. 3.8b and Fig. 3.8c). The first two figures correspond to $\sqrt{s} = 900$ GeV data and Fig. 3.8c to $\sqrt{s} = 7$ TeV

3.3 The detection and monitoring systems

In the following section the RICH detection monitoring system implemented for the operations is briefly reviewed.
The key element is an HPD column shown in Fig. 3.9 where the elements and electronic boards (details in Tab. 3.2) are visible.

	RICH 1	***RICH 2***
Level–0	7	8
LV	4	4
HV	7	8
HPD	14	16

Table 3.2: Number of boards and HPDs per column for the two RICH detectors

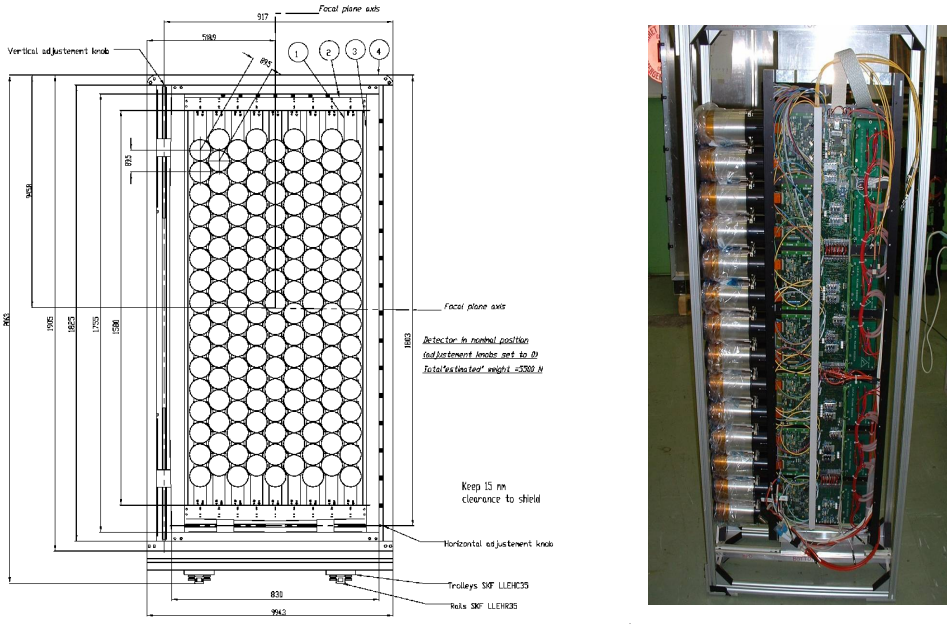

Figure 3.9: On the left: scheme of one side of RICH2 detector were the hexagonally packed layout of the HPDs is visible. On the right: an HPD's column with all the redout and supply circuitry, HPDs, L0, LV and HV, in place

3.3.1 The LHCb pixel Hybrid Photon Detector

The photon detector chosen for the RICHes is a pixel Hybrid Photon Detector (HPD) [97–102] developed in collaboration with industry. It is used to measure the spatial positions of emitted Cherenkov photons with a fast readout covering a total area of 2.6 m^2. They are arranged in 9 columns of 16 HPDs (see Fig. 3.9 and 7 columns of 14 HPDs on each side of RICH 2 and RICH 1 respectively.
HPDs are able to detect single photons with high efficiency, have high spatial granularity and are sensitive to Cherenkov photons in the visible and in the UV ranges of the electromagnetic spectrum (200–600 nm).
The structure of the HPD is a cylindrical vacuum tube with an overall diameter of 83 mm and a length of 115 mm. To decrease the residual magnetic field, individual HPDs are surrounded by MuMetal cylinders [103, 104]. These shields are important because the external magnetic field causes distortions of the photoelectron trajectory, resulting in a non–trivial correspondence between the position of the impinging photon on the photocathode and the pixel hit on the anode. Residual distortions will be regularly monitored during data taking and corrected using an offline analysis.
The HPD has a spherical quartz window which is the photocathode with a *S*20 multi–alkali deposited on the inner surface. After the photoelectric conversion of the incident photon, electrons are generated, accelerated and cross–focused into the silicon sensor by the potential difference between the grounded anode and the photocathode. The potential difference is set with three electrodes, the photocathode is at V_1 =-18 kV and the two others value are V_2 =-17.7 kV and V_3 =-14.8 kV. The chip is the anode at 80 kV. The voltage values and their ratios determine the cross–focusing and the demagnification factor of each tube. The

pixel chip is an array of 32×32 columns equal to 1024 pixels of 0.5×0.5 mm^2 corresponding to the 2.5×2.5 mm^2 image at the photocathode level due to the demagnification factor of 5. The anodic radial coordinate is obtained as:

$$r_a = 0.200 r_c - (4 \times 10^{-4}) r_c^2 \tag{3.10}$$

with r_c the the coordinate on the cathode The silicon pixel chip [105, 106] is bump–bonded

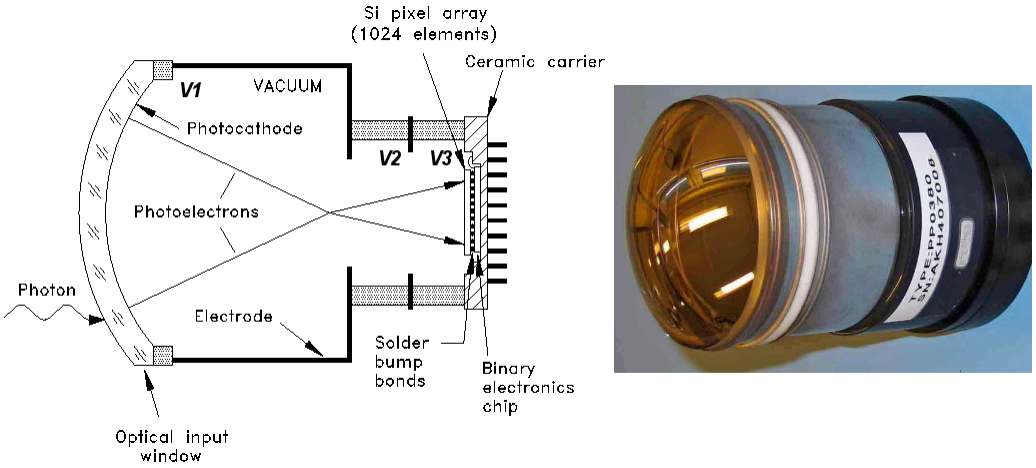

Figure 3.10: Design and picture of the pixel hybrid photodetector

to a binary redout chip mounted and wire bounded to a Pin Grip Array (PGA) ceramic carrier. In the 0.25 μm commercial CMOS front–end chip, the photoelectron dissipates the energy generating ∼5000 electron-hole pairs (3.6 eV is the threshold energy to generate one electron–hole pair and 19 keV is the incident photoelectron energy). The signal size to which every channel of the chip is sensitive, which is the minimum threshold, is 2000 electrons with a RMS spread of 200 electrons. It provides a binary readout signal with 4 μs latency. Every chip is read in ∼900 ns (32 rows × 25 ns + data headers) with 32 lines in parallel to reduce at the minimum level possible lost of data and reducing dead time at the order of 1%.
The detection efficiency obtained from laboratory and beam tests is of the order 88%. Results were obtained taking into account some effects that can affect the detection efficiency, namely:

Charge sharing: it is the probability that an electron does not release all the energy in a single pixel but also in an adjacent one causing a detectable signal. This effect gives counts in two adjacent pixels

Ion feedback: the effect occurs when a photoelectron ionizes a residual gas molecule in the tube, the ion being then accelerated to the cathode and focused in the central zone, where it release electrons, which then travel to the anode. This signal has a delay of ∼250 ns compared to the prompt one and it creates large pixel clusters because the number of electrons released by the ion is large

Dark counts: it is a noise effect due to a thermionic emission from the photocathode. The expected rate is low, below of 5 kHz/cm^2, but not negligible

3.3.2 The Level–0 and Level–1 boards

The redout and the transfer of the data from the HPD to the online system is made by two boards. The first one, the Level–0 (L0) [107, 108] board is placed on the HPD column, near the HPD itself, as shown in Fig. 3.11. It acts as an interface between the HPDs and the ECS (Experiment Control System), TFC (Timing and Fast Control) and data transmission systems. Its main tasks are to receive data from two HPDs, add headers containing event information and data-integrity checks, and transfer events to the data transmission system at 1 MHz trigger rate via optical fiber to the Level–1 board.
The RICH L1 [109] electronics, located in the counting room, has been designed to implement data compression and to serve as the interface between the custom data transmission protocol of the L0 electronics and the standard protocol used by the DAQ network. This board receives data from the L0 boards applying the zero-suppression algorithm in parallel. Each receives data from 36 HPDs reducing the information to multi HPD event packets and transmits them to the DAQ network.

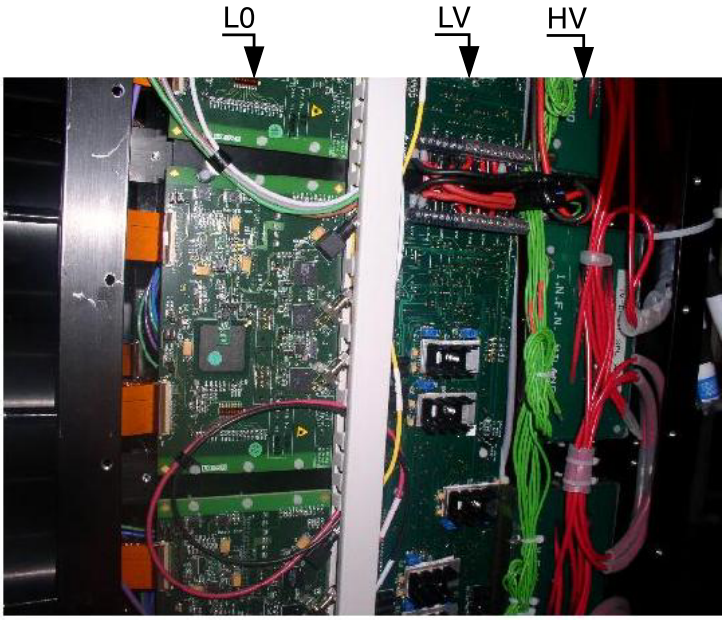

Figure 3.11: L0, LV and HV boards mounted on a RICH HPD column

3.3.3 The Low Voltage board

The necessity to supply the HPD chip and the L0 boards with low voltages is accomplished by the Low Voltage (LV) distribution system. This module is placed on the HPD column near the two boards to be supplied, as shown in Fig. 3.11. The LV board is composed by a system of regulators able to deliver low voltages from 1.5 V to 5 V.
Each column is equipped with 4 LV boards of different types which differs from each other by the number of regulators. Remotely it is possible to manage every LV board trough the SPECS [110] interface, located in the first board, which sends enabling commands to set

all the regulators. The SPECS is used to interface both the HPD and the L0 boards of the column and to switch on and off the voltage regulators, thus allowing careful control of the powering of the column.

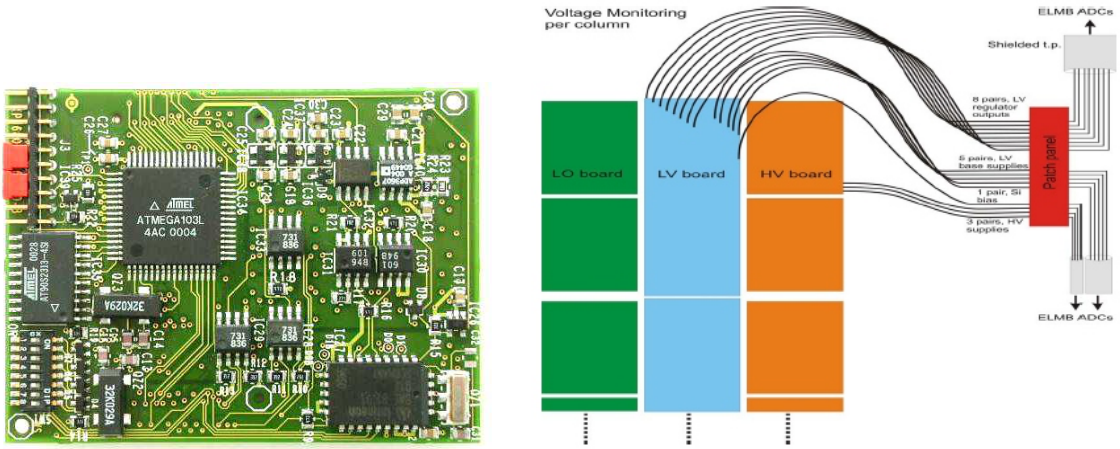

(a) (b)

Figure 3.12: Layout of the front side of the ELMB board in 3.12a and the scheme of the ELMB channel readout of the voltages for one column of the RICH in 3.12b

3.3.4 The ELMB and the protection boards

The Embedded Local Monitor Board (ELMB) is credit card sized, designed for various control and monitoring tasks in the LHC experiments. Several parameters of different modules can be monitored for the experimental safety and for the reliability of the data taking. All the ELMB modules of the whole experiment have the same structure and are part of the Detector Control System (DCS) of the experiment. They can be described starting from their 3 main parts: analog, digital and CAN. Each board is equipped with 64 differential analog inputs and 32 digital I/O lines redout with a 16 bit ADC (see in Fig. 3.12a) which can handle inputs between -2 V and +5 V and it run at 4 MHz. Examples of variables monitored by the ELMBs are temperature, humidity and pressure of the gases, voltages and currents.
For the RICH detector the ELMBs read both the LV and HV voltages.
As described in the previous section HPD electrodes are supplied with very high voltages, the highest is -18 kV delivered by the supply modules located at $\sim$40 m from the column, and it is necessary to monitor their stability. The input needed for the ELMB board is a signal of few volts, for this reason the high voltage distribution board was designed with a voltage attenuator to match the voltage levels to the monitoring device. The attenuators are limited in case of discharges to 100 V but this value is anyway outside the ELMB safety range. Further precautions must be taken to assure safe operation to the monitoring circuits implementing a protection board (PB) [111]. The board buffers the voltage lines, attenuated by about 12800 V/V in normal operating conditions, and limits the output voltage excursion to the ADCs of the monitoring system to a safe range in case of discharge.
During normal operation the board acts as a -1 gain buffer offering the needed positive

signal in input to the ELMB. In the anomalous case of a large voltage change, larger than 150 V, the circuitry saturates and produces a signal output acceptable from ELMB range.
The PB output channels are 7, of which 6 needed for the Top and Bottom HV half columns and one for the polarization of the silicon chip. This board is located in the experimental area and it has been designed to be radiation tolerant under the expected working conditions of LHCb.

3.4 The HV Boards

The High Voltage (HV) [112] distribution board system delivers the voltages needed to the HPDs to accelerate and focusing the photoelectrons onto the anode pixels. These boards are placed on the HPD column. Each column, for sake of the voltage distribution system, is segmented in two halves. The half–column unit is therefore the part of the detector to be disconnected in case of problems. The HV needed for the operations is delivered $\sim$40 m far from the column from the Very High Voltage (VHV) system. The VHV will be described in the following Chapter.
Each HV half column is independently powered by a voltage of -18 kV and has a splitter block from which the additional -17.7 kV and -14.8 kV lines, necessary to the HPD, are generated.
Each column is equipped, as listed in Tab. 3.2, with 8 HV boards (RICH 2) and 7 HV boards (RICH 1). There are two types of HV boards, Splitter (SB) and Monitoring (MB) blocks, made by three blocks (splitter, monitoring and bias). The boards are chained together to compose the half column having one SB at one edge and one MB at the other edge. The existence of different types of boards is the result of the limited space available for the electrical components. The splitter and the monitoring blocks cannot be contained in one board together with the bias block. Here there is the description of the three main blocks:

Splitter block: it is powered by the VHV at -18 kV and implements a custom high precision resistive dividers, shown in Fig. 3.13, to split the voltage in two other lower voltages ($V_1 = -18$ kV, $V_2 = -17.7$ kV and $V_3 = -14.8$ kV)

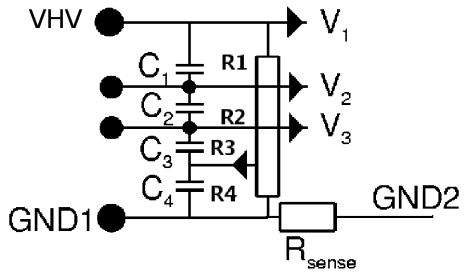

Figure 3.13: Circuit of the HV board splitter block

	C (nF)		R (MΩ)
C_1	30	R_1	4.12
C_2	2.2	R_2	47.9
C_3	1	R_3	125
C_4	1	R_4	125

Table 3.3: Parameters of the circuit of the splitter block of Fig. 3.13

Monitoring block: it provides low voltage outputs for the ELMBs, the external monitoring of the HV values. It consists in a voltage splitter, as shown in Fig. 3.14 (R_H =5 $G\Omega$

and R_L =392 $k\Omega$) implemented with HV precision resistors of ($\pm$1%). GND1 and GND2 are separated only during the test phase and are short–circuited connected together in normal operation. The Surge Arrestor (SA) protects the outputs against any possible discharge to $\pm$150 V

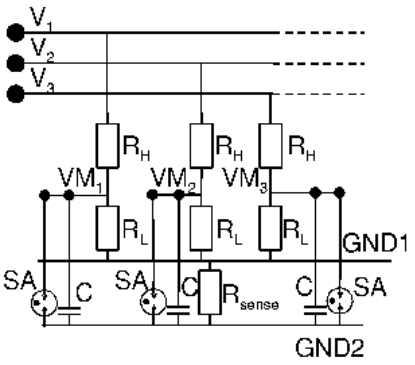

Figure 3.14: Schematic of the monitoring block circuitry of the HV boards

Delivered		Monitored	
V_1	-18.0 kV	VM_1	-1.41 V
V_2	-17.7 kV	VM_2	-1.39 V
V_3	-14.8 kV	VM_3	-1.16 V

Table 3.4: Delivered and monitored voltage values from the monitoring block of the HV boards

Bias block: it provides the HV distribution to a pair of HPDs. All the boards are equipped with this block. The bias block has three HV series resistors, each one connected to the HPD electrodes. They prevent from a large current flow in case of accident.

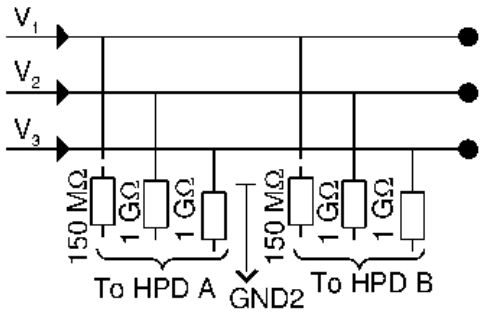

Figure 3.15: Scheme of the bias block of the HV board

The electrical components to be used in HV applications have large dimensions and the distance between nodes at very different potentials must respect minimal values. For the RICH HV boards, the available space is limited and the components used are forced to stay in close proximity. For this reason the HV boards are 4 layers Printed Circuit Board (PCB) completely dipped in an insulator material, Silicone Tough Gel (STG) [1], with a dielectric strength of 17 kV/mm.
These boards are placed in the experimental zone and all the components are radiation hard. It was tested that, after a radiation exposure, no appreciable damage has been observed in

[1] Sylgard DC 3-4241 by Dow Corning

the functional behaviour and on the surface of the insulator used to cover the boards. Other test were done to study the voltage behaviour, stability and the leakage current of the boards, and all these tests [113] fulfill the requirements of LHCb and satisfy the specifications of the design.

3.5 The HV board characterization

All PCBs of the system have been characterized with specific tests needed to study the behaviour of all the sensitive parameters. Leakage current, voltage stability and structural parameters were studied [114]. These tests were done in extreme working conditions which guarantee stable and reliable operations.
The set–up used supplied and monitored two columns (4 half columns) at the same time. As described in Sec. 3.4. the monitoring block has a custom resistive divider made by components with $\pm 1\%$ tolerance ($\pm 3\sigma$). In each measurement there was a channel dedicated to the voltage supply readout. This input line has a Reference Divider (RD), consisting of 2 GΩ and a 100 kΩ resistors with $\pm 1\%$ tolerance.
All the tests have been done with a voltage value of -21 kV. The set voltage was higher than the operating one to ensure the complete reliability of the boards. At the end of all tests, the characterization of the boards with respect to the voltage supply measured by RD, gave the voltage distribution shown in Fig. 3.16. All the plots have a RMS consistent with the expected tolerance, guarantying that all the boards have similar components and they are well manufactured.
To obtain a better accuracy, a statistical approach to the characterization was used, as it will be described in the following.
Although the voltage supply V_S, delivered by the HV module[2], may vary slightly from test to test, the RD attenuator factor β, the 2 GΩ–100 k Ω resistors, is always the same for all the tests. It depends only on temperature variations, which were anyway monitored. The RD measures the voltage V_j:

$$V_j = \beta V_S \tag{3.11}$$

Each half column has the same structure with its own resistive dividers embedded in the monitoring block, which give:

$$V_{Mij} = \alpha_{ij} V_S \tag{3.12}$$

where $i = 1,2,3$ is the index of the three output voltages and $j = 1 \rightarrow$ N with N the number of tested half columns. The value V_{Mij} in Eq. 3.12 can be known with a precision of 1% ($\pm 3\sigma$), the tolerance in α_{ij}. For a deeply investigation, a procedure has been established to exploit the whole ensemble of measurements.
Let's start by comparing the two equations above:

$$\frac{V_{Mij}}{V_j} = \frac{\alpha_{ij} V_S}{\beta V_S} \Longrightarrow \frac{V_{Mij}}{V_j} = \frac{\alpha_{ij}}{\beta} \tag{3.13}$$

the ratio V_{Mij}/V_j is independent of the input voltage V_S. This way the achievable accuracy is closed to that of the multimeter, of the order of 100 ppm/C.

[2] Iseg EXP 30020524_5$CLD0 \rightarrow 30$ kV

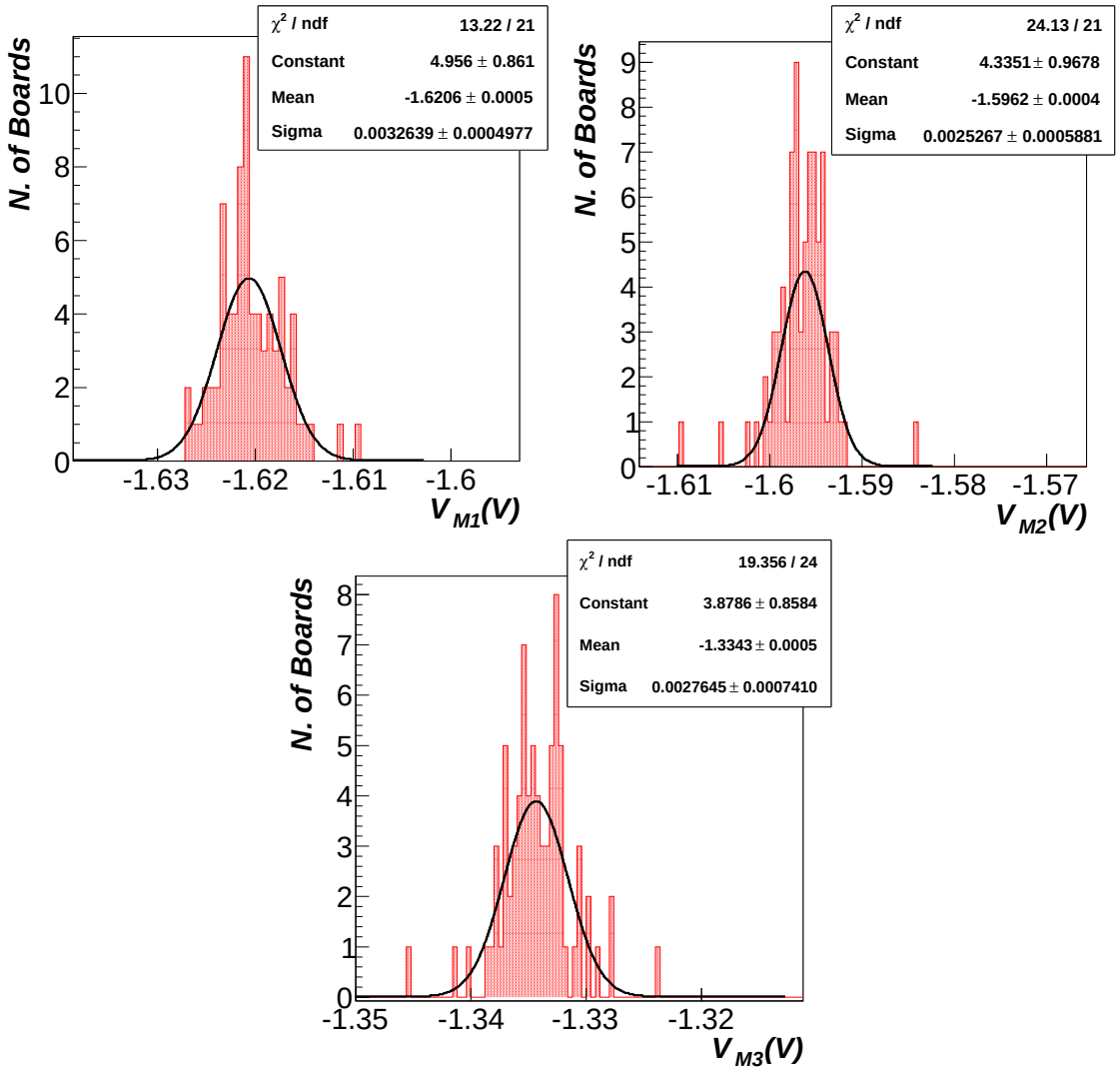

Figure 3.16: Histograms of the mean voltage values measured for all the columns

After the characterization of every column is done, the average value of the ratio $\left\langle \frac{V_{Mij}}{V_j} \right\rangle = \frac{\langle \alpha_{ij} \rangle}{\beta}$ is obtained by fitting the voltage distribution of all measurements. A calibration coefficient can be introduced:

$$\gamma_{ij} = \frac{\left\langle \frac{V_{Mij}}{V_j} \right\rangle}{\frac{V_{Mij}}{V_j}} = \frac{\langle \alpha_{ij} \rangle}{\alpha_{ij}} \tag{3.14}$$

The coefficients γ_{ij} are completely independent from the coefficient β of the RD monitoring resistor. If now Eq. 3.12 is multiplied by γ_{ij}, $\gamma_{ij} V_{Mij} = \langle \alpha_{ij} \rangle V_S$ is obtained having precision closed to that of the multimeter. Results are shown in Fig. 3.17.

The distributions, shown in Fig. 3.17 after the coefficient multiplication, are now very narrow. The gaussian fits implement the $\sim 80\%$ of the boards considered. These fits, centered about the set values, indicate that all the resistive dividers of the monitoring blocks differ

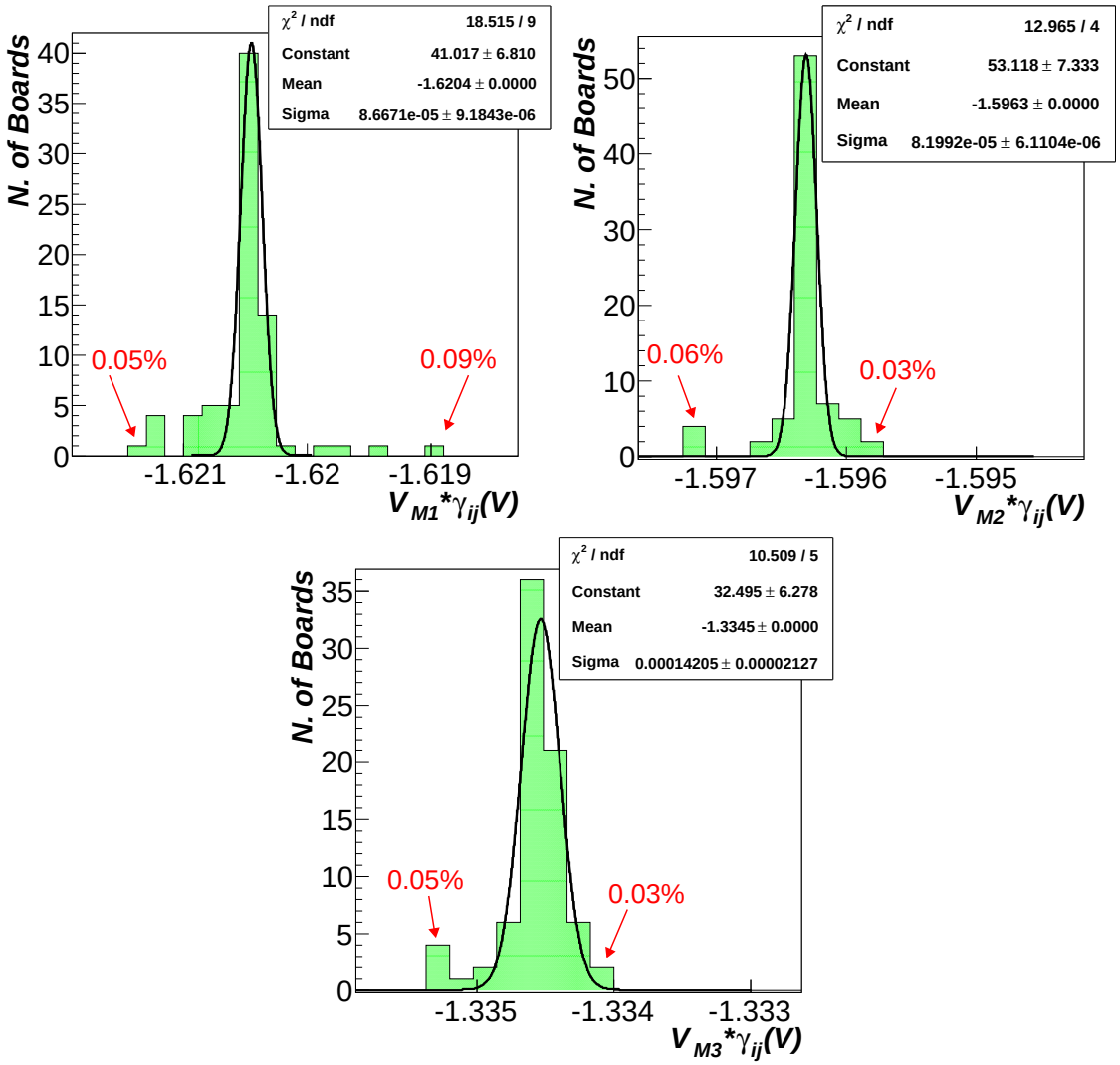

Figure 3.17: Comparison between the three different final voltage distributions after applying γ_{ij} coefficients

from each other by less than 0.005% for the first two highest voltages and 0.01% for the third one.

The most critical parameter to be measured is the voltage difference between the first two dynodes $\Delta V_{1,2} = 300$ V responsible of the cross focusing field of the HPDs. For $\Delta V_{1,2}$ the correspondent error is only ± 0.02 V. The other voltage difference $\Delta V_{1,3} = 3200$ V can be appreciated with an uncertainty of ± 0.36 V.

Looking at Fig. 3.17, the two arrows point to the largest errors obtained anyway well below 1%. Tab. 3.5 summarizes all the results of the fits.

To better appreciate the γ_{ij} effects, Fig. 3.18 shows superimposed the two histograms taken before and after the application of the coefficients γ_{ij}. The correspondent systematic errors, calculated at the operating voltages, are reported on the right of Tab. 3.5. Considering the three biasing voltages, the two smaller have larger errors. This effect is due to the presence

Voltage	*Mean(V)*	*Sigma*	*Mean(V)*	*Sigma*
V_{M1}	-1.6206	0.0033	-1.6205	0.00009
V_{M2}	-1.5962	0.0025	-1.59638	0.00008
V_{M3}	-1.3343	0.0028	-1.3347	0.0001

$\Rightarrow$

Voltage(V)	*Sigma(V)*
-18000	0.9
-17700	0.9
-16400	1.3

Table 3.5: Values obtained with data taken during the test phase. In the left part data of the measurements, in right part data optimized with gamma coefficients. In the right table the expected error at the nominal operational value induced by the monitoring block

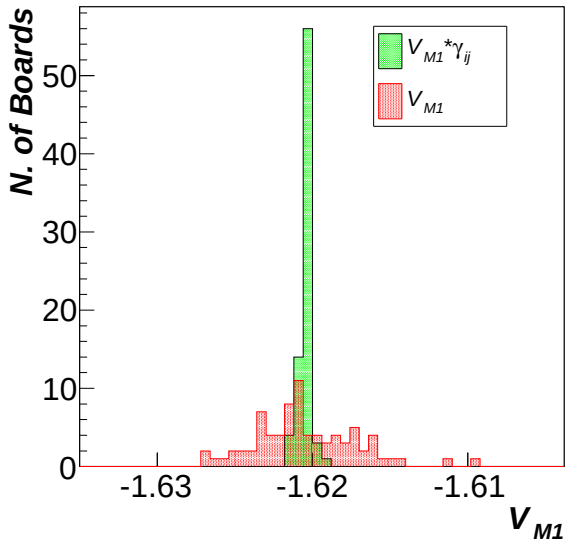

Figure 3.18: Superimpostition of the histograms: the red one is the V_{M1} voltage without correction coefficients applied; the green plot is the voltage V_{M1} corrected with coefficient γ_{1j}

of the bleeder chain which slightly degrades the accuracy. Nevertheless the final accuracy is, in the worst case smaller than 1.5 V, a remarkable result.
In the beginning there was the idea to disentangle the three voltage outputs to evaluate their accuracy independently. Nevertheless the very good results obtained with the described method made it needles.

CHAPTER 4

THE HV SYSTEM OPERATIONAL STABILITY

As described in the previous chapter, the very high voltage system for the hybrid photon detectors must be stable over time in order to ensure the best performance at detecting Cherenkov photons.
In this chapter the very high voltage system is described in details: the hardware infrastructure and the observed issues during operations. The analysis of the operational stability will conclude it.

4.1 The Very High Voltage system

The Very High Voltage (VHV) system is needed to supply voltages to the HPDs.
Stable high precision of the Cherenkov angle resolution is the challenge of the RICHes, so that voltage and current must be stable during data taking and present a low ripple. This has been extensively tested in the laboratory with the VHV module candidate. Before the assembling and the commissioning of the detector all units have been checked to ensure their reliability. Results were very promising, giving a voltage resolution of the order of $\sim$1 V at -20 kV [115].
The current drawn by each supply is 260 μA. This is needed by the resistive bleeder chain to bias the three HPD electrodes.
The VHV system [115] is located at about 40 m away from the experiment, outside the experimental zone, allowing the use of standard and non–radiation hard components. The control and monitoring system consists of two main parts as shown in Fig. 4.1: the Main Board and the Control Board with the VHV power supply unit.

4.1.1 The Main Board

The first part of the VHV system, on the left of Fig. 4.1, is the Main Board (MB) equipped with a Credit Card sized PC (CCPC) and a Glue Card (GC). There are two such MBs, one

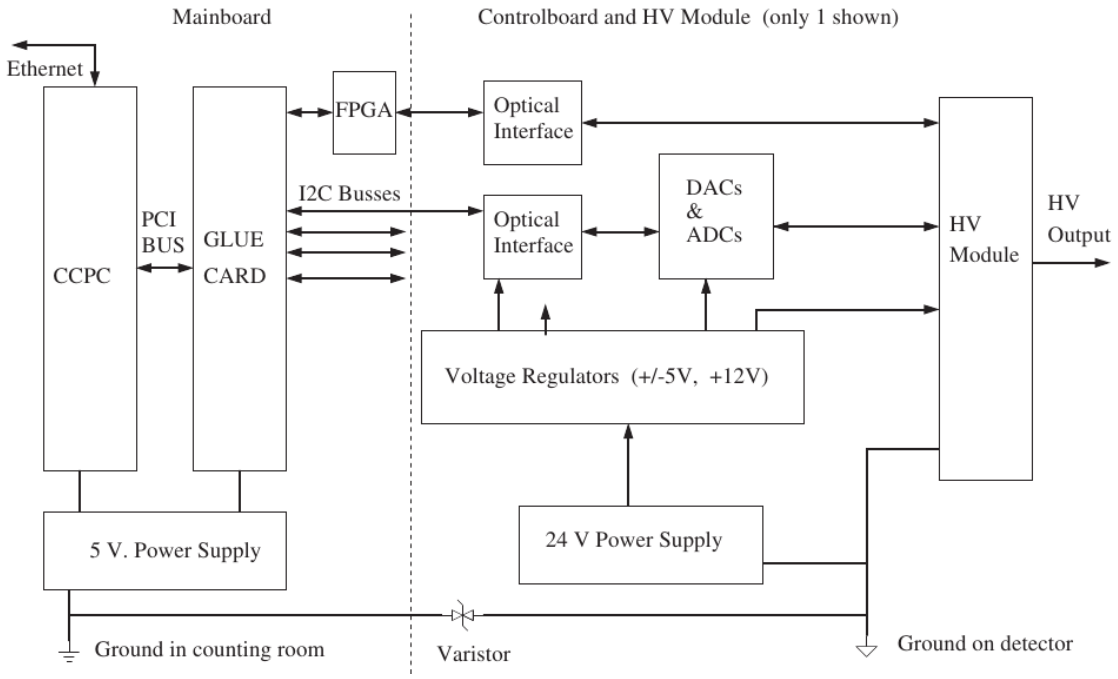

Figure 4.1: Schematic view of the VHV power supply system [115]. In evidence the two main parts: the Main Board on the left and the Control Board with the VHV supply module on the right

for each RICH detector and they manage all HV channels.
The MB is made of three blocks as seen on the schematic view sketched in Fig. 4.1:

FPGA: a XILINX XC3S200 provides the enabling signal for the HV units. It monitors the interlock command coming from the general LHCb Detector Safety System (DSS). In case of emergency, it applies the disabling command to all channels.
It runs also the so–called "watchdog" function which disables channels in case of hang or stuck of the CCPC

CCPC [116]: it provides the control of the whole HV system and allows the ethernet connection to the LHCb Experiment Control System (ECS). It is an embedded PC [1] on a Credit Card (CC) sized plug–in card.
The system relies on the AMD ELAN 520 microcontroller operating with a Linux system and includes also a controller for the ethernet connection. This device is not directly connected to the second part of the VHV system, but it has a PCI–Bus. All communications with custom designed devices are performed via this special parallel bus generated by the I/O Accelerator PLX9030

Glue Card [117]: it is the interface board used to interface the CCPC and the internal devices. It provides the I^2C [118], the JTAG [119] and the parallel busses needed for the interface. It is based on the PCI9030 module and a second FPGA, the XILINX SPARTAN XCS05XL. The PCI9030 acts as a bridge between the PCI bus of the CCPC and the parallel bus. The FPGA interfaces the I^2C and JTAG controllers. In

[1] SM520PC SmartModule produced by Digital–Logic, Inc.

case of CCPC reset, the GC is well separated from the CCPC in order to isolate the user electronics from the local bus

The whole HV system is controlled by a software running in the CCPC under a Linux platform environment. It uses the same protocol to connect all LHCb subsystems. More precisely the software runs on a ramdisk in order to be less affected by possible LHCb network disruptions. It also provides interface with PVSS via a DIM server, as described in Sect. 4.2. The software is divided in two parts. The first one permanently runs as a daemon in background. It reads values from a configuration file, initializes and enables all channels. After the initialization, a loop cycle checks the status of all channels and applies the commands issued by the user. The second part, "the client", is a low–level console interface to the users which runs independently from the previous part. It samples the channels giving the possibility to manage the system choosing from the main framework or a stand–alone mode. It is also possible to change voltage values, ramp–up and ramp–down rates of the whole system, of a single channel or manage all the other variables together. These client features are available to the user via a shared memory space which interconnects the two software parts.

4.1.2 The Control Board and the VHV module

The second part of the VHV system, displayed in the right part of Fig. 4.1, consist of a Control Board (CB) coupled to a VHV supply unit. Their coupling is in Fig. 4.2.

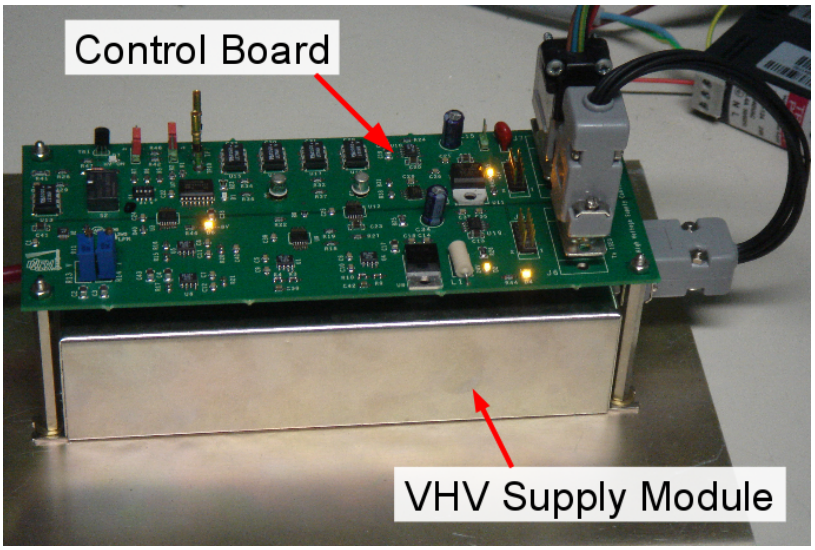

Figure 4.2: Example of a VHV module and CB composition

Control Board (CB): there is one for each VHV supply unit, as shown in Fig. 4.2. It provides remote control and monitoring of voltage and current of the VHV supply unit. This is achieved via the 16–bit DACs and ADCs respectively. To avoid ground loops, an optical fiber connection was introduced between the CB and the MB, implemented with standard optocouplers.

The block scheme is shown in Fig. 4.3. Control signals, received by the bi–directional I^2C bus, are routed to the 16–bit DACs to set the maximum current and the output voltage values. The monitoring of the variables (V_{Mon}, I_{Mon} and the 24 V power) is achieved by the 16–bit ADCs

VHV power supply: the VHV supply unit is produced by the German company ISEG [2]. The commercial type is equipped with a single output cable. For the LHCb experiment, ISEG produced customized units. Each supply module has two output cables to supply the two half columns. This modularity was required to minimize performance loss in case of severe VHV problems on a column. This double cable configuration was the initial baseline. These units are powered with a low voltage of 24 V and they are able to deliver an output voltage from 0 V up to -20 kV

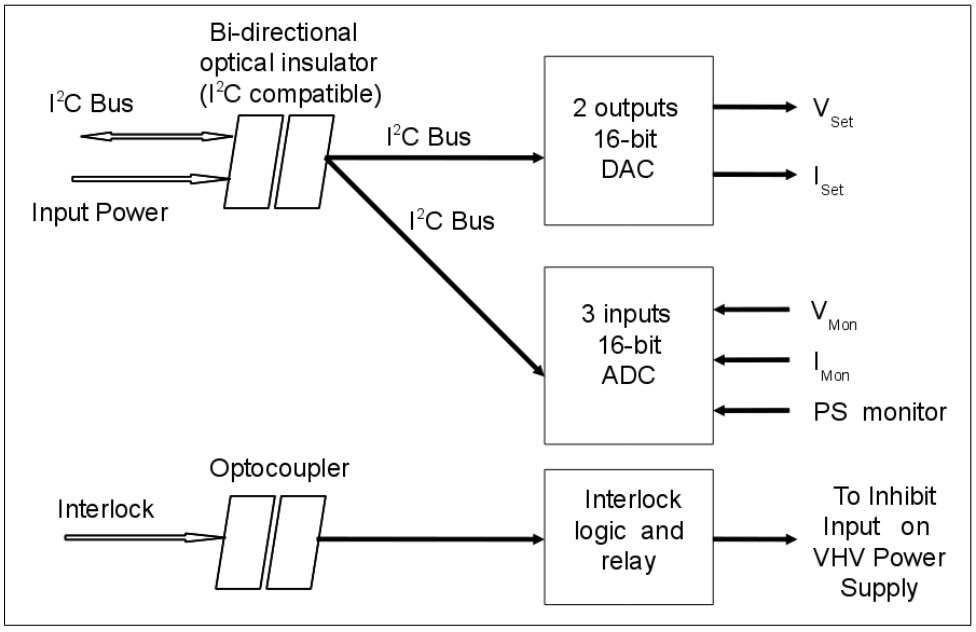

Figure 4.3: Schematic view of the CB. All the outputs and the inputs, "watchdog" function and all connections are displayed

4.2 PVSS and the High Voltage Projects

The LHCb Experiment Control System (ECS) is based on a commercial Supervisory Control And Data Acquisition (SCADA) system. The software application used is PVSS® [120, 121] which provides the operation of all LHC experiments.
An efficient system requires that all components are controlled with the same interface in a coherent way, given the system complexity. There is also the necessity to have a fast communication able to send and receive commands. Managing all facilities is achieved by a tree structure with a limited set of instructions, common to all systems. LHCb uses the PVSS

[2] CPn 200 504 24 10-K2

framework to access and control utilities, for data acquisition, logging, archiving and alarm handling. Therefore this is also valid for the RICH detectors. The whole infrastructure can be operated and the controlled variables can be grouped and archived in an Oracle database. Examples of such variables are pressure, temperature, humidity, voltages and currents.
The two RICHes have the same structure and the PVSS flexibility gives the possibility to control them as two different entities or simply as a single one. In the PVSS jargon, these entities are called projects.
The Detector Control System (DCS) for the RICH project [122] has the function to power the detector, ensure safe operations, collect and archive environmental information from sensors useful for the analysis. The basic detector unit is a HPD column. As explained in the previous chapter Sect. 3.4 the VHV system scheme is depicted with a VHV supply, which delivers the operational -18 kV and two operating HV splitter boards, simply called HV board, per column. The HV boards split the -18 kV voltage and supply the other two electrodes.
The main PVSS project which manages the HV modules is the HV project able to send and receive commands from the CCPC and from the users, as described in Sect. 4.1. This project is the direct manager of the voltage supply boards and allows remote control by the users via PVSS.
The column structure constrains the coexistence of high and low voltage boards in a narrow space. In that way the behaviour of the low voltage boards can be disturbed or influenced with a fast voltage change of the HVs. For the detector safety, ramp up and down rates are chosen to reduce at minimum level these effects. In Tab. 4.1 the different states available for the ramping of the HV system with the corresponding rates (identical for both RICHes) are reported. Columns are considered on at -18 kV, but to reach this value there are three transition steps (Tab. 4.1). The first two steps are faster than the third one to avoid stability problems. The ramp up takes typically 10 min for RICH 1 and RICH 2 to reach -18 kV.
There are two different projects for the VHV monitoring. The first one for the VHV supplies and the second one for the three HVs delivered to the HPDs located inside the HPD boxes.
The VHV system is a sensitive and important project requiring continuous monitoring. Its behaviour must be supervised and checked in two different steps. The first one is the on-line monitoring. It is important to access easily all the information and check the ramping phases and the status of the system. This feature is used by the normal user during the status check of the detector. The second step is the off–line stability analysis. In both cases the users have the possibility to check trend plots and retrieve old data.
The two projects are:

ELMB project: the ELMB, described in Sect. 3.3.4, archives all environmental values. Using the overview panel it is possible to retrieve all the ELMB voltage values of all the photocathodes and electrodes, and for all half columns. The voltages monitored are: $VM1_{Up/Down}$, $VM2_{Up/Down}$ and $VM3_{Up/Down}$

HV project: it is the HV manager and gives access to the HV module variables (voltage V_{Mon}, current I_{Mon} and status flags reported in Tab. 4.2 (b)) and to the ELMB ratios, $VM2/VM1_{Up/Down}$ and $VM3/VM1_{Up/Down}$. By default all variables are logged every 5 or 15 min. In addition any deviation larger than 5 or 10 V, 5 or 10 μA, compared to

the previous sampled value, is logged and/or displayed

Steps	Step (kV)	Ramp up (V/s)	Ramp down (V/s)
StandBy1	$0 \rightarrow 3$	50	100
StandBy2	$3 \rightarrow 13$	50	100
GoReady	$13 \rightarrow 18$	20	100
GoOFF	all $\rightarrow 0$	$10^{(3)}$	300
EmergencyOff	all $\rightarrow 0$	/	Disable unit

Table 4.1: HV states from the PVSS control. The first two columns present the initial and final values set for each step. The last two columns indicate the rate values of the ramping steps

(a)

	VHV	HV proj.	ELMB
Sampling period	5 min	2 s	10 s
Voltage storage (voltage threshold)	10 V	5 V	10 V
Voltage storage (time interval)	5 min	15 min	15 min
Current storage (current threshold)	5μA	10 μA	/
Current storage (time interval)	5 min	15 min	/

(b)

	Logical Status
ON	1
OFF	0
Over current	-3
Over voltage	-2
Under current	-4
Under voltage	-5
Alarm	-6
No network link	-1

Table 4.2: Table (a) reports logging criteria. Table (b) reports logical status of the VHV system and PVSS links

4.3 The online monitoring

The VHV system is controlled and monitored by the software running on the CCPC described in the previous section, Sect. 4.1. It gives the possibility to archive data in a separate file, simply enabling the logging option of the tool. All values are not recorded in the Oracle database, but saved in a text file in a temporary directory. These data coming directly from the HV supply units read out by the CB. Data stored are only voltage, current, alarm and error state messages. After the debugging phase of the system, the same data are also now

[3] Default settings not relevant in the corresponding configuration

available in the HV main project. an example is given in Fig. 4.4.
This archiving option is activated since the beginning of the commissioning period. Every

```
May 10 12:20:30 r2hv01.lbdaq.cern.ch hvcd[3038]:   ch  0: Vfinal 18000, Vmon  18040.7, Imon:  257.73
May 10 12:20:30 r2hv01.lbdaq.cern.ch hvcd[3038]:   ch  1: Vfinal 18000, Vmon  18109.6, Imon:  259.29
May 10 12:20:30 r2hv01.lbdaq.cern.ch hvcd[3038]:   ch  2: Vfinal 18000, Vmon  18044.2, Imon:  258.62
May 10 12:20:30 r2hv01.lbdaq.cern.ch hvcd[3038]:   ch  3: Vfinal 18000, Vmon  17944.9, Imon:  255.49
May 10 12:20:30 r2hv01.lbdaq.cern.ch hvcd[3038]:   ch  4: Vfinal 18000, Vmon  17998.3, Imon:  257.39
May 10 12:20:30 r2hv01.lbdaq.cern.ch hvcd[3038]:   ch  5: Vfinal 18000, Vmon  18058.2, Imon:  256.79
May 10 12:20:30 r2hv01.lbdaq.cern.ch hvcd[3038]:   ch  6: Vfinal 18000, Vmon  17980.7, Imon:  257.64
May 10 12:20:30 r2hv01.lbdaq.cern.ch hvcd[3038]:   ch  7: Vfinal 18000, Vmon  17884.2, Imon:  256.81
May 10 12:20:30 r2hv01.lbdaq.cern.ch hvcd[3038]:   ch  8: Vfinal 18000, Vmon  17970.6, Imon:  257.17
May 10 12:20:30 r2hv01.lbdaq.cern.ch hvcd[3038]:   ch 10: Vfinal 18000, Vmon  17732.0, Imon:  253.55
May 10 12:20:30 r2hv01.lbdaq.cern.ch hvcd[3038]:   ch 11: Vfinal 18000, Vmon  17970.2, Imon:  256.67
May 10 12:20:30 r2hv01.lbdaq.cern.ch hvcd[3038]:   ch 12: Vfinal 18000, Vmon  17995.2, Imon:  257.25
May 10 12:20:30 r2hv01.lbdaq.cern.ch hvcd[3038]:   ch 13: Vfinal 18000, Vmon  17987.0, Imon:  257.82
May 10 12:20:30 r2hv01.lbdaq.cern.ch hvcd[3038]:   ch 14: Vfinal 18000, Vmon  18000.6, Imon:  258.86
May 10 12:20:30 r2hv01.lbdaq.cern.ch hvcd[3038]:   ch 15: Vfinal 18000, Vmon  18024.7, Imon:  258.77
May 10 12:20:30 r2hv01.lbdaq.cern.ch hvcd[3038]:   ch 16: Vfinal 18000, Vmon  18019.3, Imon:  258.78
May 10 12:20:30 r2hv01.lbdaq.cern.ch hvcd[3038]:   ch 17: Vfinal 18000, Vmon  17895.1, Imon:  256.83
May 10 12:20:30 r2hv01.lbdaq.cern.ch hvcd[3038]:   ch 18: Vfinal 18000, Vmon  18046.5, Imon:  257.64
May 10 12:20:30 r2hv01.lbdaq.cern.ch hvcd[3038]:   ch  2: Vfinal 18000, Vmon  18055.1, Imon:  258.61
May 10 12:20:34 r2hv01.lbdaq.cern.ch hvcd[3038]:   ch  2: Vfinal 18000, Vmon  18044.2, Imon:  258.54
May 10 12:23:03 r2hv01.lbdaq.cern.ch hvcd[3038]:   PVSS Switching off Ch.   8
May 10 12:23:03 r2hv01.lbdaq.cern.ch hvcd[3038]:  PVSS - set_param, ch. 8, vset = 0.000000
May 10 12:23:03 r2hv01.lbdaq.cern.ch hvcd[3038]:   PVSS Switching off Ch.   8
May 10 12:23:03 r2hv01.lbdaq.cern.ch hvcd[3038]:   PVSS Switching off Ch.   1
May 10 12:23:03 r2hv01.lbdaq.cern.ch hvcd[3038]:  PVSS - set_param, ch. 1, vset = 0.000000
May 10 12:23:03 r2hv01.lbdaq.cern.ch hvcd[3038]:   PVSS Switching off Ch.   1
```

Figure 4.4: Example of few lines of the archived log file of RICH 2

time the VHV daemon on the CCPC is re–started a new log file is created. The study that will be described in the following sections is the work that covers about two years starting from the commissioning period of LHCb up to the end of 2010. It is performed considering these data. During this period, especially during the commissioning phase, all PVSS projects were in constant evolution. Not all the display panels were available, nor all the alarms and all parameter values were being optimized. Consequently the availability of the log tool was essential. Since the CCPC software runs independently from PVSS, it gives the possibility to study the system directly. Therefore it is possible to test the link between the main framework and the daemon running on the CCPC and to debug the whole system.

4.4 Voltage and current behaviour

The study of the high voltage system distribution covers three important periods for LHCb: commissioning, first pp collisions with LHC in machine development mode and collisions for physics.
In the first period, everything was evolving: all projects, the software and the RICH project. For the HV project the main issue was the debugging and the optimization of the running parameters and alarms.
During the first collisions all detectors worked with good stability under global control. Moreover during this second period the highest priority for the experiment was detector safety. For the HV point of view the main issue was to check stability and possible correlations observed between variables, such as temperature [123] or low voltage issues.
During the last period, everything was running smoothly in global mode and most parameters were only monitored to control the global status.
The VHV software gives all the information needed to check the status of the VHV system

and the link with the external PVSS control software. All possible statuses that can be identified are reported in Tab. 4.2 (b). The analysis is performed starting from these values and considering only voltages in the plateau after stabilization. The following section describes the main observed features and the analysis done for the optimization of the whole system.

4.4.1 Stable columns

The RICH detector was designed to achieve the best possible operational condition, with particular emphasis on high voltage stability.
One example of a stable column is column U5. Fig. 4.5 shows the voltage trend plots. The corresponding gaussian fits yield small widths (0.89 V and 0.05 μA for voltage and current), as shown in Fig. 4.6.
Ripples are lower than the detection system resolution and lower than the 1% specification. These values are comparable with the values obtained during the test phase reported in Sect. 4.1.

Figure 4.5: Example of a stable column: U5. Trend plot of the ELMB voltages in June 2010

4.4.2 Saturation spikes

Once the voltages of each column have reached the plateau, at the operational voltage of -18 kV and current of 260 μA, the expected behaviour is stability of both voltage and current about these values.
This is the optimal behaviour, but during the year spurious effects appeared on some channels. The present section describes the observed feature. During operation events with an overcurrent status and a large undervoltage were registered. The current increases to its

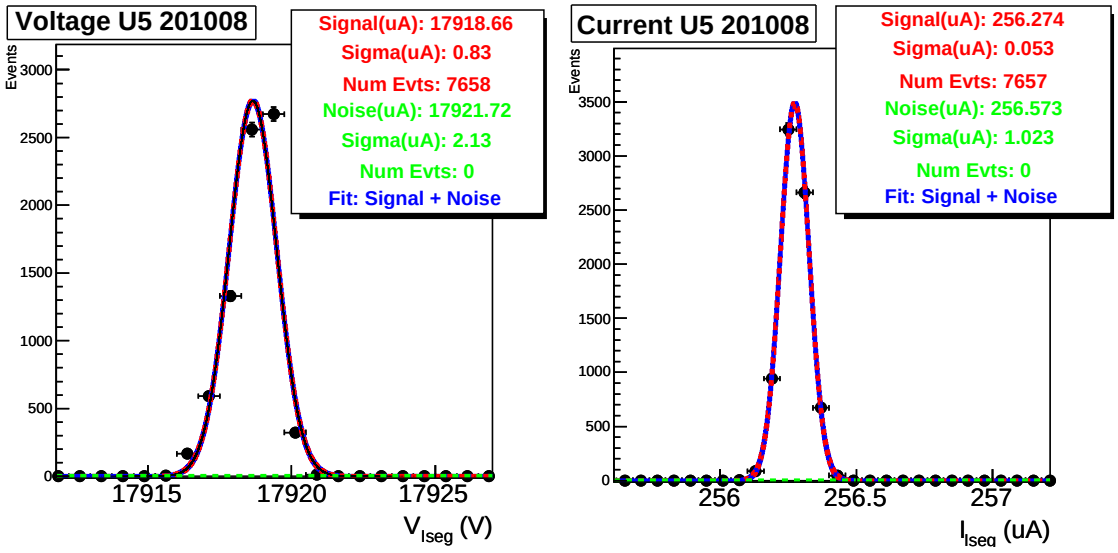

Figure 4.6: Voltage and current histograms fitted considering gaussian model for both signal and noise. In this case the noise is negligible and the corresponding fit parameters not relevant

maximum limit set to 350 μA. The supply unit in this case is operating in current–limit mode, resulting in an output voltage drop larger than 10 kV. In the following, these events are referred to as ”saturation spikes”. Fig. 4.7 displays the log file output lines with data before, during and after the detected spike. After a short while the plateau of -18 kV is reached again.
Saturation spikes may induce instabilities inside the HPD. Most of the times they also upset the Level–0 boards and/or the pixel readout chip.
Up to now spikes have not caused serious problems, but had the consequence of HPDs being disabled during data taking. The disabled HPDs are usually restored with a power cycle of the L0 boards at the end of a run.
Over the last year several studies and hypotheses were made to try to understand the cause

```
Dec 14 06:04:40 r2hv01.lbdaq.cern.ch hvcd[3321]:   ch 12: Vfinal 18000, Vmon  17994.4, Imon:  258.73
Dec 14 06:05:41 r2hv01.lbdaq.cern.ch hvcd[3321]:   ch 12: Vfinal 18000, Vmon  17993.6, Imon:  258.81
Dec 14 06:06:39 r2hv01.lbdaq.cern.ch hvcd[3321]:   ch 12: Vfinal 18000, Vmon   3479.1, Imon:  345.93
Dec 14 06:06:39 r2hv01.lbdaq.cern.ch hvcd[3321]:  SPIKE!!! detected on  channnel  12, V= 3479.1, I=  345.9
Dec 14 06:06:41 r2hv01.lbdaq.cern.ch last message repeated 16 times
Dec 14 06:06:41 r2hv01.lbdaq.cern.ch hvcd[3321]:   ch 12: Vfinal 18000, Vmon  17990.5, Imon:  260.70
Dec 14 06:06:42 r2hv01.lbdaq.cern.ch hvcd[3321]:   ch 12: Vfinal 18000, Vmon  17990.5, Imon:  260.70
Dec 14 06:07:43 r2hv01.lbdaq.cern.ch hvcd[3321]:   ch 12: Vfinal 18000, Vmon  17993.2, Imon:  258.79
```

Figure 4.7: Lines from the text log file of a detected saturation spike

and to find a way to solve or reduce this undesired behaviour.
Some hypotheses taken into account are:

Magnetic shielding: all HPDs are surrounded with individual magnetic shields. Their close proximity to photocathodes could possibly generate breakdown discharges. Three layers of Kapton foil insulate the grounded shield from the HPD electrodes. This insulation has been tested up to -22 kV during shield production [124]. So far, there has

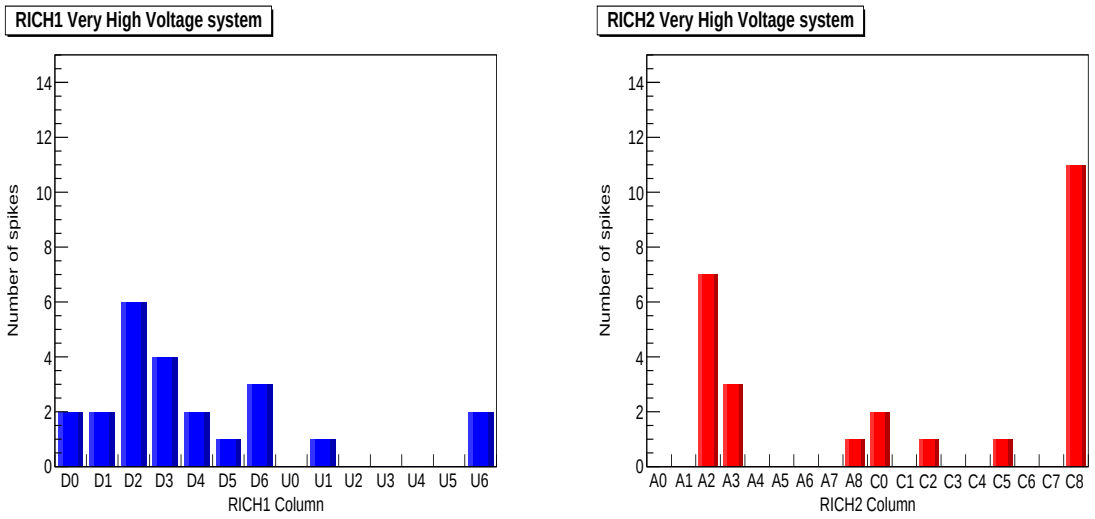

Figure 4.8: Number of spikes for all HPD columns in the two RICH detectors (left plot for RICH1, right plot for RICH2)

not been any evidence of a discharge in this insulation layer.
Detection limitation is due to the ELMB sampling rate and the asynchronous method. ELMBs are not, in fact, the best spike detection probes

High voltage splitter board: these boards are printed circuit boards populated with high voltage resistors and capacitors described in Sect. 3.4. All boards are embedded in silicone rubber to minimize possible discharges. All boards were tested in the laboratory at -21 kV [113], also in extreme conditions of humidity and temperature. All tests showed the required stability and reliability, no single spike was observed.
A saturation spike in the HV splitter board should induce an overcurrent status. As a consequence, the CB enables the current limit mode for both half columns managed

Cables and connectors: they are usually and routinely operated at -20 kV satisfying the CERN rating [4] [5]

ELMB: these boards are used for the readout of environmental parameters. They read many channels and if the board is the cause of a spike, more than one channel should be affected at the same time. Similar common effects have been observed for close–by columns, but they are attributed to pick–up noise. It should be pointed out at this stage that, most of the time, spike data are not recorded by the ELMBs since these are sampled asynchronously. Consequently these data points are not archived by the ELMB project

Readout system: in this case the spike should be caused by a trivial electronic noise feature. It would never produce any effect in the system. This is not the case, the spikes

[4] LEMO connector, cable plug, FFR.1Y.416.CFAE67G,
`http://intra.lemo.ch/catalog/ROW/UK_English/high_voltage.pdf`

[5] coaxial high voltage cable, HTC-50-2-1,
`http://communications.draka.com/sites/eu/Datasheets/hf44e.pdf`

are real and cause malfunctions in the detector

Control board: another possibility is a feature on the readout system or on the CB connected to the HV unit. They are the VHV manager. A voltage control converts small signal into a large output voltage. A badly soldered component or an ADC converter problem can introduce noise or, with a wrong bit as described in the following section, a wrong voltage value. This last idea implies that if the CB should be the cause of the spike, it can be detected with a certain frequency for the wrong bit generation. This behaviour was never observed

Environmental parameters: humidity and temperature might modify properties of the materials used to manufacture the supply units. In the barrack, where the HV modules are installed, a sensor monitors humidity and temperature of each electronics rack. The corresponding output data are not archived in the database. Thorough laboratory tests identified a clear correlation between humidity and temperature, and small–amplitude noise glitches [123]. The air flow in the rack was improved to keep temperature and relative humidity as low as possible, but direct correlation with the spike probability was not fully established

VHV supply unit: this is the most probable source of saturation spikes. The supply units are customized for LHCb and equipped with two output cables. This feature implies the use of a cable fanout embedded inside the HV block filled with potting material. VHV units supply voltages for long periods with frequent ramp up and down phases. On a long time scale the resulting temperature variations inside the unit modify the potting resin properties with the consequence of causing spikes.
For this reason a subset of modules was once more sent back to ISEG for a new refurbishment. LHCb required to revert to single cabled units with a home made external splitter. In parallel the company decided to use a new potting material and replaced the HV block of all these supplies. This material will be used by default for any new production or refurbishment. In addition the module case has been re–designed and comprises lateral openings for better heat dissipation

There are currently two single cabled units operating in the RICH detectors. They are installed in columns A0 (old potting material) and D3 (new potting material). Both of them are very stable. Another nine similarly refurbished units are available to replace problematic ones. They all have been tested successfully in the laboratory.
For completeness it should be noted that the spikes are not always observed on a noisy column. The column behaviour before and after a spike is also different for different columns. As an example, column A2 is one of the worst column spike–affected as shown in Fig. 4.8. There were no clear signal fluctuations before and after the detected spikes. In that case it was not possible to establish if or when the spike will happen.
There are other cases where the spikes are correlated to the presence of noise. In these cases the symptom is noise itself increasing with time and stopping when a spike occurs. After, the voltage is seen stable until the next spike. An example of such an effect is illustrated in Fig. 4.10 for column D4.

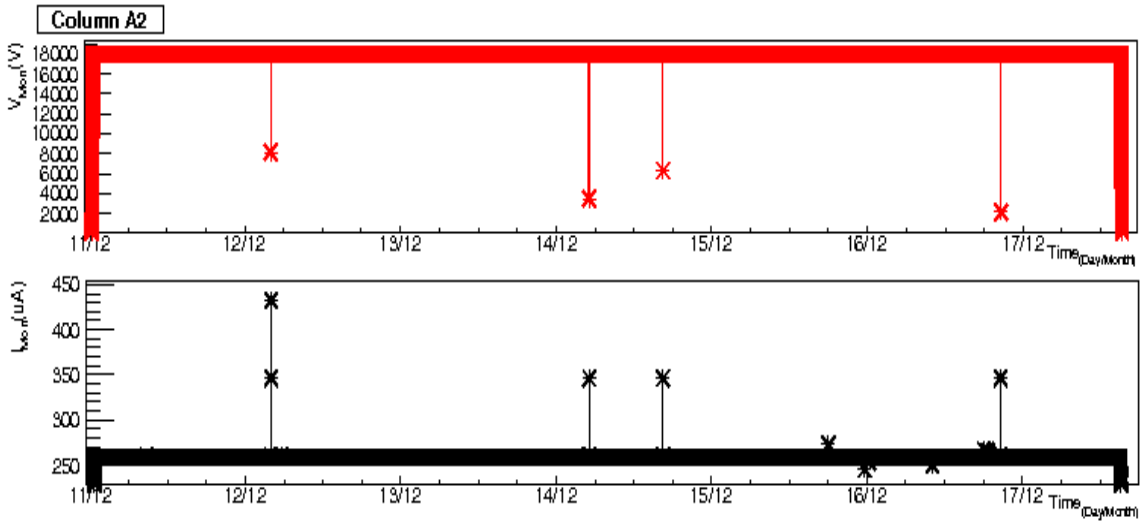

Figure 4.9: Trend plot of column A2 recorded in December 2009 with 4 saturation spikes. Before and after the spikes both voltage and current are extremely stables

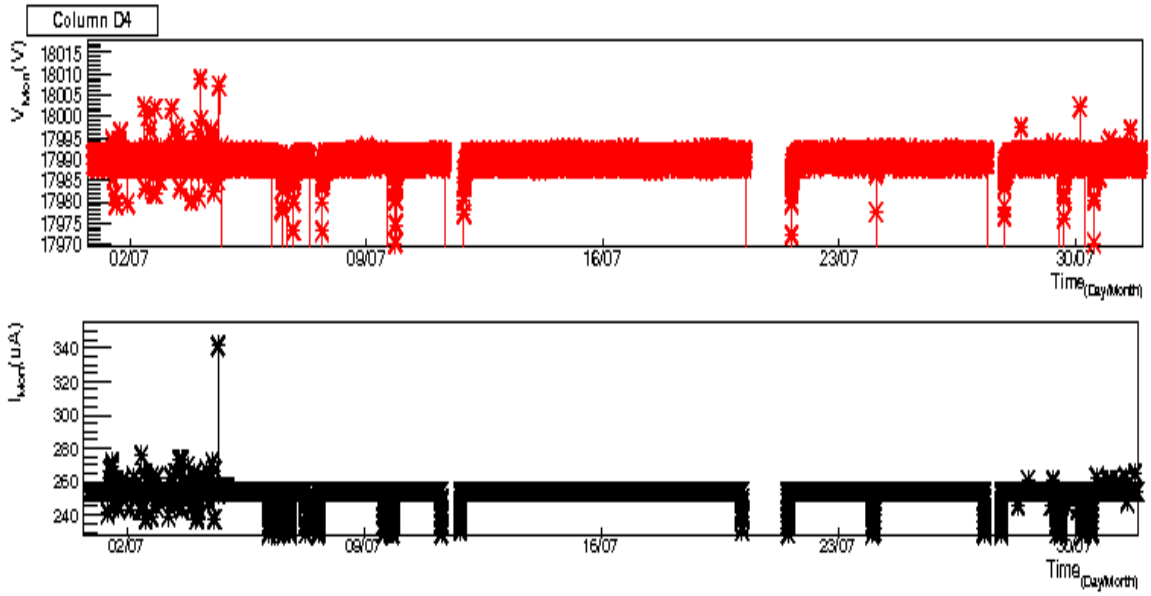

Figure 4.10: Trend plot of July 2010 for column D4. It shows noise before the saturation spike. The voltage scale is zoomed about the mean value to appreciate the voltage behaviour before and after the saturation spike. After the spike there is very good stability. Noise restarts after 20 days

4.4.3 The noise effect

Another behaviour observed at the plateau is noise. What is called noise are fluctuations with various frequencies of voltage and current about a mean stable value. Not all columns are affected and those columns showing this effect, have not the same behaviour.
These variations are visible as voltage and current excursions of the order of $\sim$10 V and few μA. These fluctuations are, in the worst cases, also detected by ELMBs despite their lower sampling rate.

The high sensitivity required by the system implies an analysis of this behaviour.
In the following pages examples of noisy columns are presented in order to illustrate the different behaviours observed and the operation complexity.
Another open question is the correlation between saturation spikes and noise behaviour. These effects are uncorrelated in most cases, but not for all of them. One example is column A2 that shows a high number of spikes, but is otherwise stable as shown in Fig. 4.9.

Constant noise

A constant noise is characterized by small voltage and current fluctuations, with typical amplitudes of a few V and a few μA. To better illustrate it, one example is column U6. Fig. 4.11 shows voltage and current trend plots for June 2010. Fluctuations about the mean values are clearly visible. The noise ripple is actually present since February 2010 and its amplitude has been seen increasing since then, as described in Fig.4.12 (trend plots of voltage and current noise percentage).
This unit was replaced in November 2010 with a new single cabled unit manufactured with a new potting material.

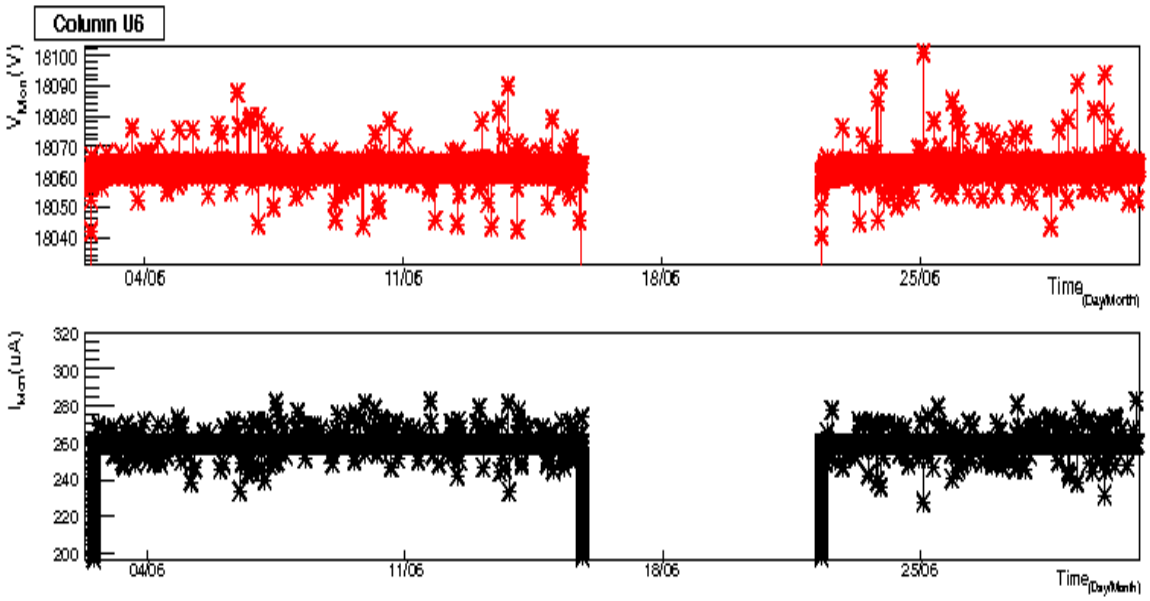

Figure 4.11: Column U6 behaviour in June 2010. Noise fluctuations are clearly visible and constant during the whole range considered

Bunches of noise

Column A0 has a different behaviour compared to the other noisy columns since the very beginning. Fig. 4.13 shows the time graph of voltage and current recorded in December 2009. The difference between this column and the previous case is that noise ripples are not always present. The noise starts at random times after a stable period. The differences were seen not only on frequency but also on time lengths and on fluctuation amplitudes.

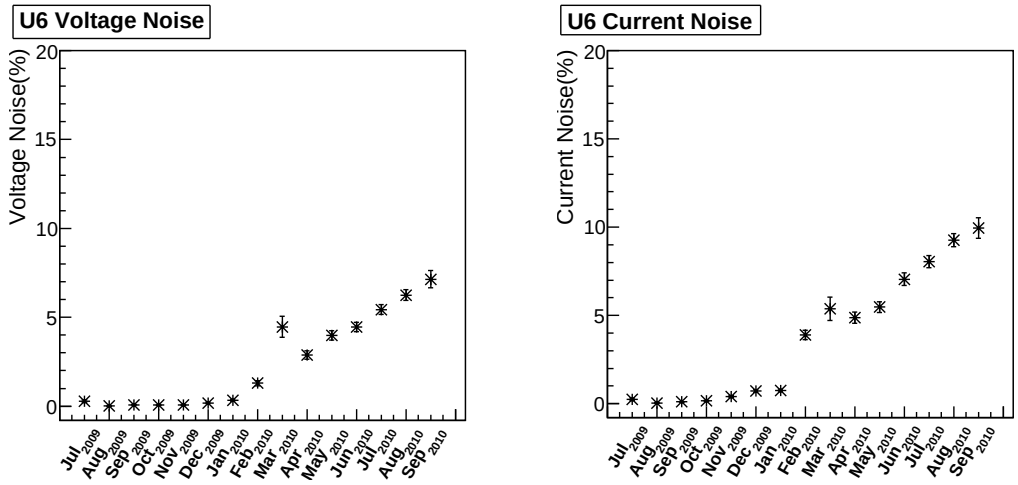

Figure 4.12: On the left: voltage noise percentage as a function of time. On the right: current noise percentage for the same period considered

The corresponding CB was exchanged in April 2010 but the noisy behaviour remained unchanged. The cause was attributed to the ISEG unit itself and it was substituted.
The noise bunches could be due to a cumulative effect caused by changes in the physical properties of the potting material in the HV block. A larger noise glitch will stabilize the system and the noise will again start to accumulate.
This behaviour is not correlated with a saturation spike since no one was detected during the whole operating period.
After replacement, this noisy unit was further tested in the laboratory where the same behaviour was observed.
The replacing VHV unit is a commercial supply unit with a single output cable. An external fanout was designed and made at CERN to connect the two half columns. Column A0 is perfectly stable since this operation.

4.4.4 Glitches and other behaviour

While the main issues detected during the RICH operation period are saturation spikes and noise, other effects were also detected. In this section these effects are briefly described.

Glitches: this behaviour is characterized by rare fluctuations detected in current and voltage. If a column is affected, the histograms show a narrow peak corresponding to the stable behaviour with a few outlying points (a few standard deviations away from the mean value). In this case the ripple amplitudes are larger than for the constant noise, but the frequency is much smaller

Control board upset: this behaviour is specific to column U4 and is clearly visible on the trend plots in Fig. 4.14. Every time the column was switched on and off, the operating point was stable but had a different mean value. The current showed the same behaviour, as was also reported in the ELMB plots. During a technical stop of the LHC machine in May 2010, the voltage supply unit and the CB were removed and tested in laboratory. The supply was seen to be working properly. A bad soldering

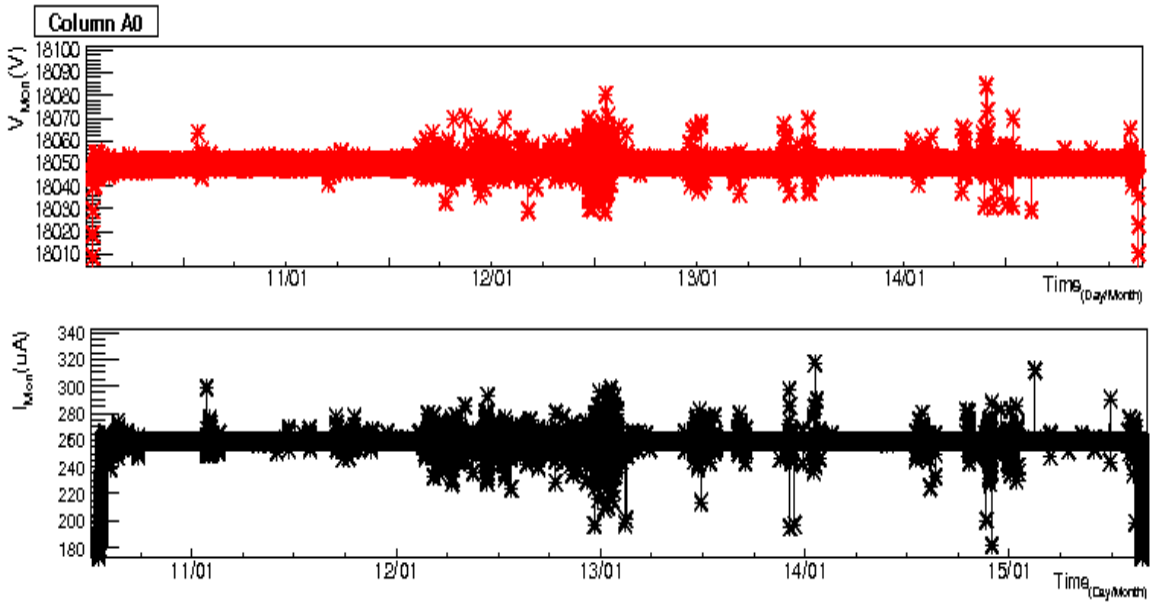

Figure 4.13: Example of bunches of noise in column A0. This behaviour is a feature specific to this column and was always present. Trend plots recorded in January 2010

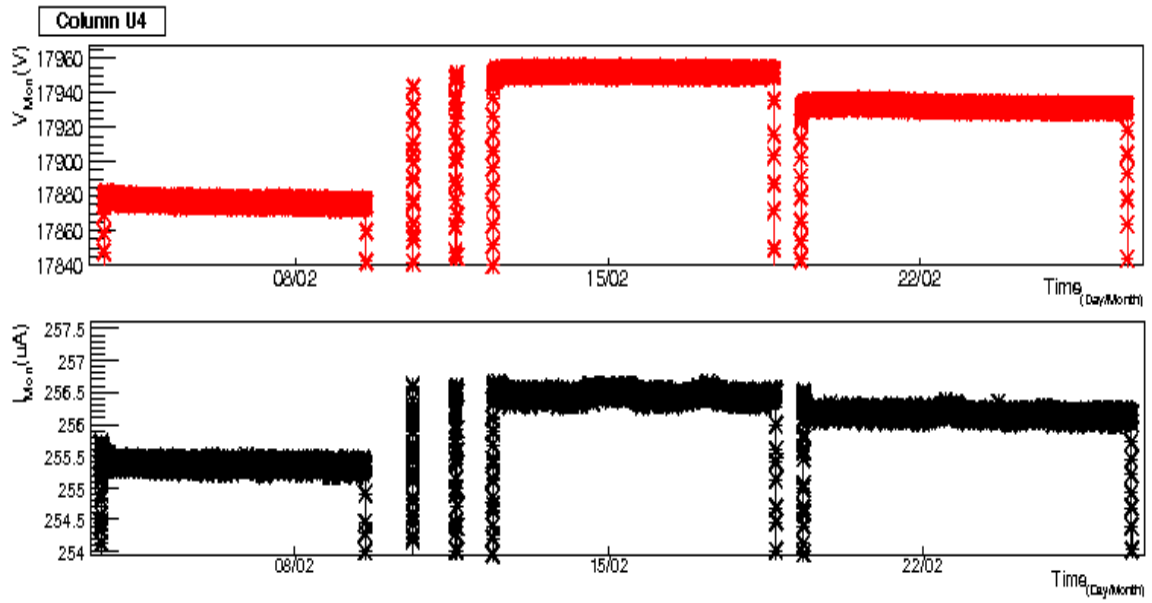

Figure 4.14: U4 trend plots showing different operating points. This behaviour, identified in February 2010, was caused by a bad solder on the CB

was identified on a trimmer on the CB. This CB was replaced with a spare one and since, this column U4 is operating optimally.

The C2 anomaly: Column C2 is an anomalous case. The voltage histograms in Fig. 4.15 show two narrow peaks separated by ∼10 V. This anomaly is also seen in the ELMB voltages, $VM1_{Up/Down}$, $VM2_{Up/Down}$ and $VM3_{Up/Down}$ displayed in Fig. 4.16. Since the V_{Mon} trend plots use 0.1V resolution the monitored values constantly flip

from one peak value to the other, shown in Fig. 4.17.

ELMB voltage trends displayed in Fig. 4.16 show jumps. This effect is the result of

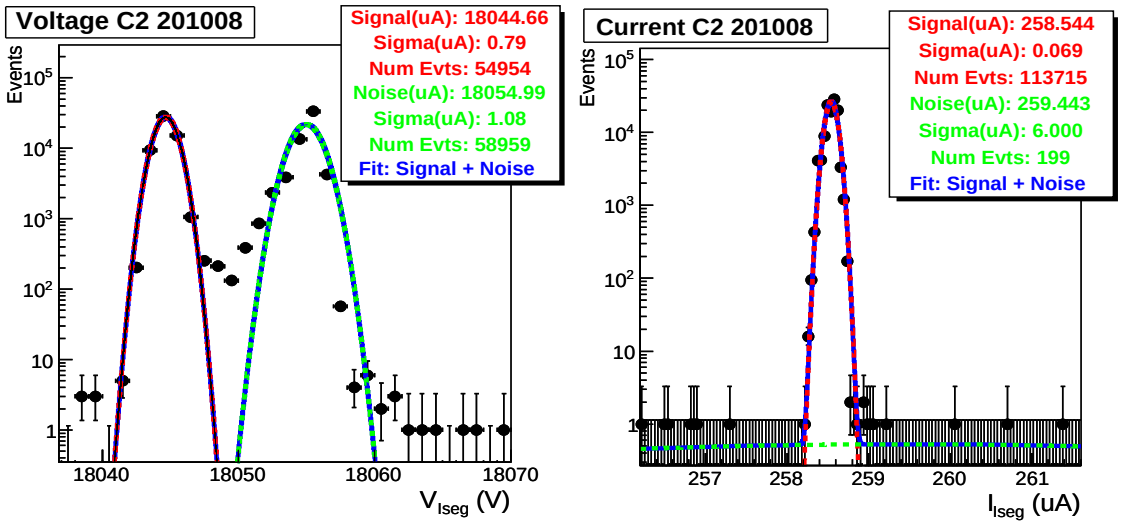

Figure 4.15: Histogram of the C2 column (August 2010). On the left the voltage histogram with the double peak divided by 10 V. On the right the single current peak with a larger standard deviation of 0.74 μA

the ELMB sampling method. The step amplitudes (10 V for VM1 and smaller values for the other two channels) are related to the resistive bleeder chain of the HV board. This double–peak effect could possibly be caused by the 16–bit DAC on the CB that sets the output voltage (more precisely with one of its conversion bits).

The ISEG unit is believed to operate properly since, with the exception of the above double peak, both current and voltage are stable. The corresponding CB has been replaced only recently (November 2010) and the whole VHV system not operated since the replacement.

The voltage feature detected in Fig. 4.15 should be also valid for the current. In the second plot there is a single gaussian due to the intrinsic resolution of the system. The standard deviation (0.074 μA) is larger than the expected of $\approx$0.05 μA.

Considering a Gaussian distribution:

$$P(x) = \frac{1}{\sigma\sqrt{2\pi}} e^{-\frac{(x-\mu)^2}{2\sigma^2}} \tag{4.1}$$

$$W = 2\sigma\sqrt{2ln2} \backsimeq 2.35\sigma \tag{4.2}$$

with mean value μ, standard deviation σ and W the Full Width at Half Maximum (FWHM) at the peak.

To resolve two gaussian distribution:

$$|\mu_2 - \mu_1| > \frac{|W_1 + W_2|}{2} \tag{4.3}$$

they do not overlap or meet at their FWHM.

Considering column C2, $|\mu_2 - \mu_1|_{Voltage} \simeq 10$ V is larger than $(|W_1 + W_2|/2)_{Voltage} \simeq$

2.2 V and the two contributions can be identified. The corresponding current peak separation is $|\mu_2 - \mu_1|_{Current} \simeq 0.13\ \mu$A. The standard deviation of a stable column is $\langle \sigma_I \rangle \approx 0.05\ \mu$A or $\langle W_I \rangle \approx 0.12\ \mu$A preventing a clear double peak identification

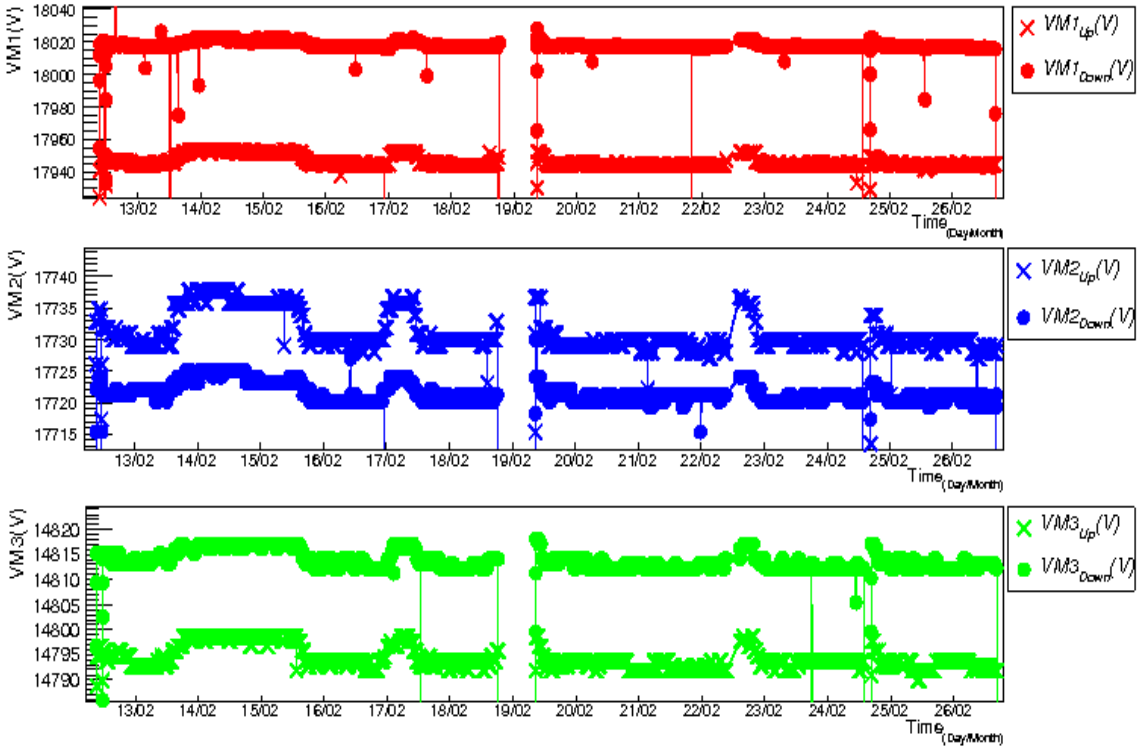

Figure 4.16: ELMB voltages for the three photocathodes of each half column (February 2010)

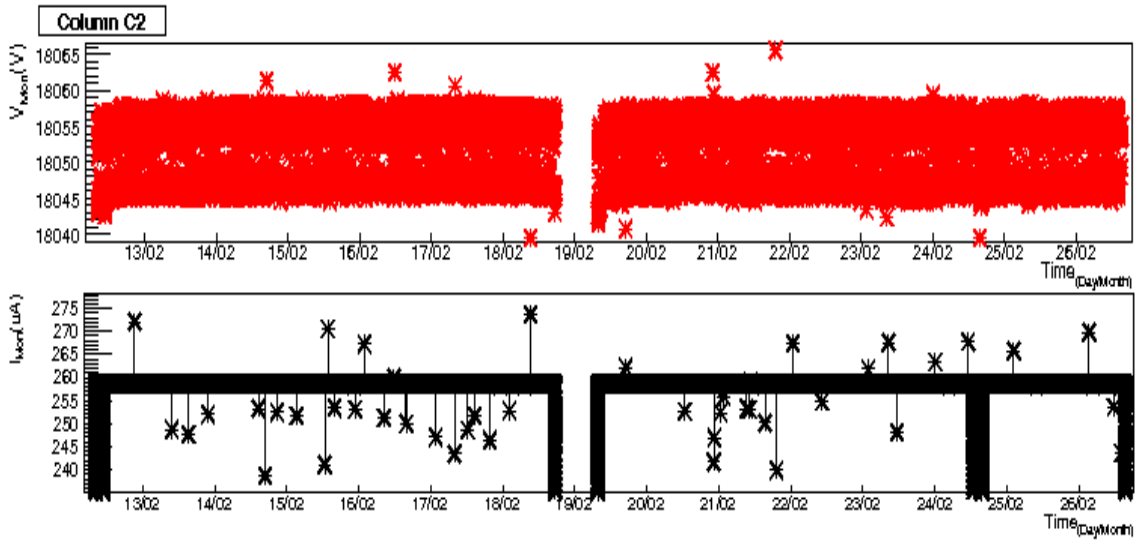

Figure 4.17: Voltage and current log file data February 2010 trend plots

ELMB floating channel: Since the commissioning period in the year 2007 the $VM3_{Down}$ channel of column A0 shows an unexpected behaviour. The values detected by this channel are unstable (see Fig. 4.18). This behaviour is already known and is probably due to a readout ELMB channel badly connected. It has been deeply investigated during an access in the experimental zone but the cause has not been identified. This unstable value has been masked in the alarm tools and is, in this way, not compromising the operations

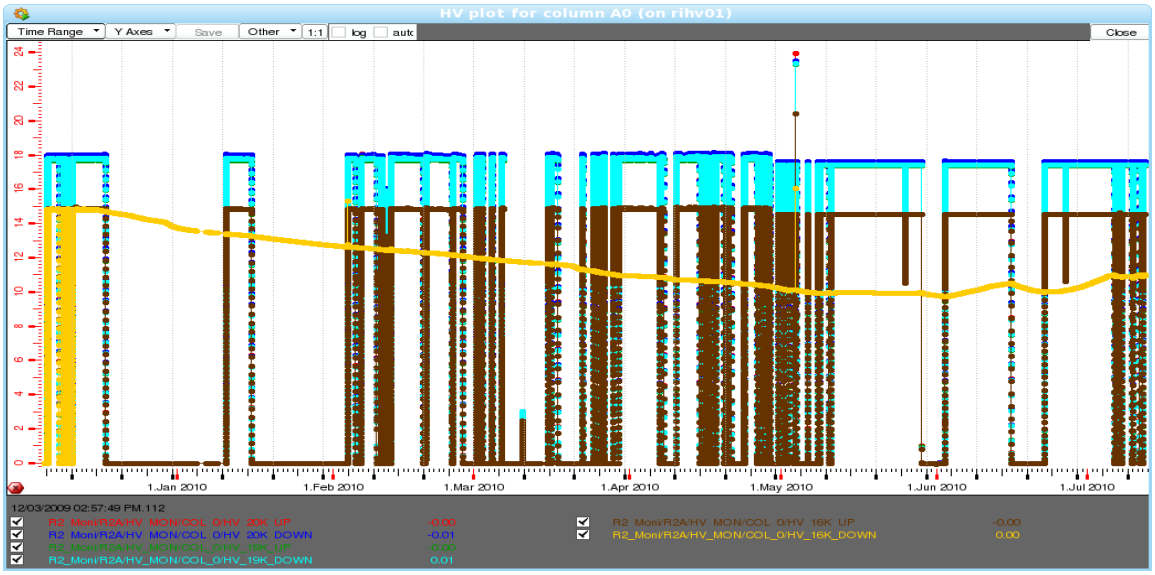

Figure 4.18: Trend plot of the ELMB values for the column A0. The yellow floating points are the $VM3_{Down}$ channel values (December 2009 - August 2010). The ELMB showed the same behaviour more than one year ago

Noise glitch detected by the ELMB: another feature has been observed only in the ELMBs in the form of several glitches with unphysical amplitude. They are attributed to pick–up noise in the monitoring lines. The apparent detected voltages can be larger than -21 kV, a value that cannot be delivered by the ISEG supplies

4.5 The analysis method

This section describes the analysis of the VHV stability and the noise after the refurbishment of July 2009.
The idea is to consider only data in the plateau at -18 kV excluding all ramp up/down values. Before explaining the procedure, some aspect considered in the analysis will be briefly described.
The high voltage system is a complex system of electronic boards connected all together. All power supply units are placed far from the detector. The HV splitter system is close to the photon detectors. These considerations are important to understand the voltage and current behaviour.
To study the stability is not only necessary to use data in the plateau, but it is essential to

be in a very stable range. Moreover looking at the end of the ramp up, voltage and current are not completely yet stabilized as displayed in Fig. 4.19. The $\sim$ 15 V voltage difference corresponds to 0.1% of the plateau value.

The total wiring resistance and the total capacitance of the system, might increase the sig-

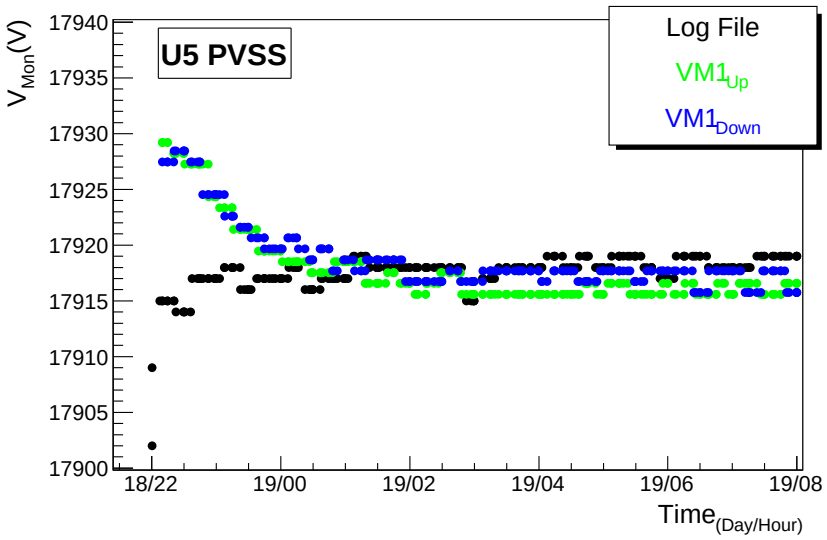

Figure 4.19: Zoomed voltage trend plots for the U5 column (May 2010). Thermal dissipation effect at the end of a ramp–up. In black the log file data, in green and blue the $VM1_{Up/Down}$ HV project values

nal rise time. The effect introduces a delay when the transition crosses the logic threshold of the -18 kV.

The HV system can be described as a RC circuit and energy dissipated in the wiring resistance is [125]:

$$E = \int i^2(t) R dt \tag{4.4}$$

with the following current flows for a ramp into the cables:

$$i(t) = \frac{V}{R} e^{\frac{t}{\tau}} \tag{4.5}$$

Eq. 4.5 has an exponential behaviour with time constant $\tau = RC$. Here R is the resistive impedance and C the line system capacity.

The main contribution to the RC is coming from the HV boards splitter block. Characteristics are reported in Sect. 3.4 giving, for each column, a $R_{Tot} \approx 75$ MΩ and a $C_{Tot} \approx 10$ nF corresponding to a $\tau \approx 1$ s. This effect is completely negligible.

It is therefore believed that the exponential behaviour seen on Fig. 4.19 is a temperature effect induced by the power dissipated in the HV board. Its circuits are, in fact, dipped into a silicone rubber [6] and when the HV units are switched on board temperature increases of few °C. Considering the 5 $G\Omega$ monitoring block impedance, it has a temperature coefficient

[6] Sylgar DC 3-4241 `http://www.dowcorning.com/`

of 100 ppm/°C [7]. The expected voltage variation is about $10-20$ V and correspond to the registered value.
All columns have V_{Mon} voltages completely stable after 2 h from the ON status.
The analysis is done considering only log file data and excludes the exponential shape range avoiding any possible bias.
The first step is the database creation obtained considering the flag status stored by the HV project and contains all the initial and final points of the plateau. The HV project and log file data have different archiving resolutions reported in Tab. 4.3. Log file data have a higher precision and are used for the analysis. The HV project data are the only used for comparisons.
The period considered extends from the beginning of July 2009 until the end of September

	Log file	**HV project**
Voltage(V)	0.1	1
Current(μA)	0.01	1

Table 4.3: Precision of the archiving projects

2010. During this time all columns remained ON for $\sim$60% of the time.
All VHV channels of both RICH detectors were considered. The study was also performed for both voltage and current.
Data are processed on a monthly basis and the procedure is iterated to understand effects as a function of time. After database production, the second step is the creation of histograms with selected data, followed by the fitting procedure.
All sampled data are assumed to have a gaussian shape about a stable mean value. The width depends on the voltage supply stability and on the sampling system precision. This is the expected behaviour for a stable column. In the real situation saturation spikes and noise effects, described in the previous sections, modify the optimal single gaussian shape.
Spikes contribute with a few points several standard deviations away from the mean value. In a first approximation they do not affect the main signal shape.
The most important aspect to take into account is the noise. This can be modeled by a second gaussian superimposed on the previous one. The main noise characteristics are the mean value that should be in the same position as the previous one, the lower integrated number of events and a standard deviation larger by a few volts and a few μA. An example of this model is given in Fig. 4.20. In the right plot black points are sampled data. Red and green gaussian distributions are signal and noise contributions respectively. On the left plot, in blue is simply the total distribution considered. It is the sum of the two previous gaussian shapes.

[7] http://www.vishay.com/docs/68000/trtd.pdf

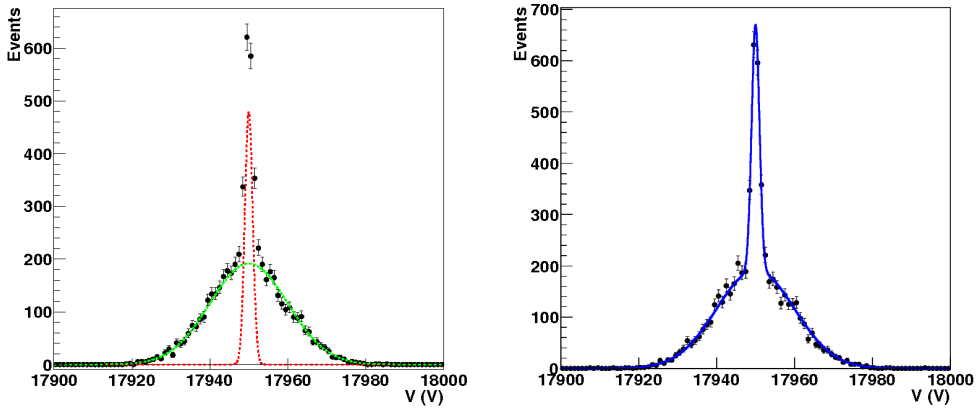

Figure 4.20: Illustration of the analysis method. On the left: data points in black, in red the signal and in green the noise contributions. For both of them gaussian distributions are considered. On the right: data points and the total fit obtained considering a double gaussian distribution

4.6 The stability analysis

The generally observed behaviour is good stability of both voltage and current over the year. Two examples are columns U6 and U0. The importance to choose these two plots is that column U0 is stable, and column U6 is one of the noisiest of the RICH 1 detector.
The trend plots of the fitted values are reported in Fig. 4.21 and in Fig. 4.22. Looking at the plots they have same behaviour with very small standard deviations. A small drop happens in March, at the time the air flow in the HV racks was improved and this drop is the consequence of a temperature effect (seasonal changes were not detected). Following this intervention however the signal fluctuations were not affected.

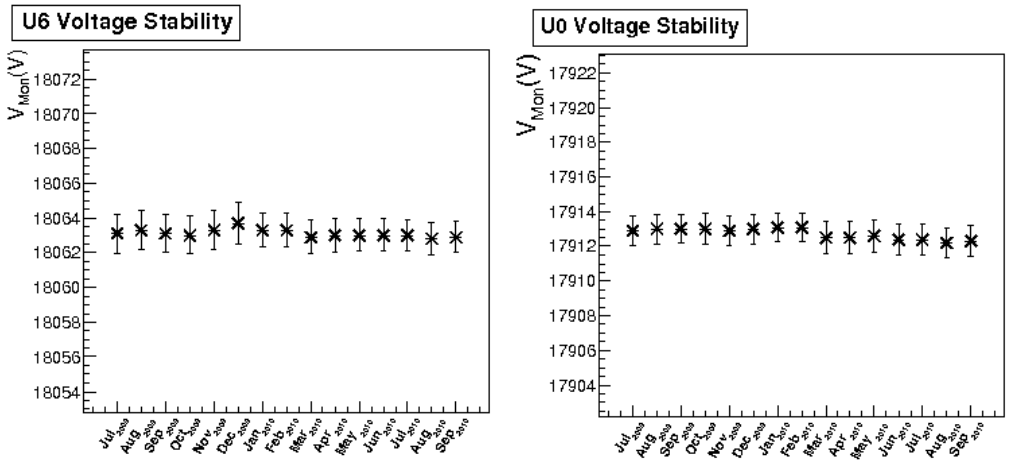

Figure 4.21: Voltage trend plots of columns U6 and U0. Comparison between the U6 noisy column with a U0 stable column

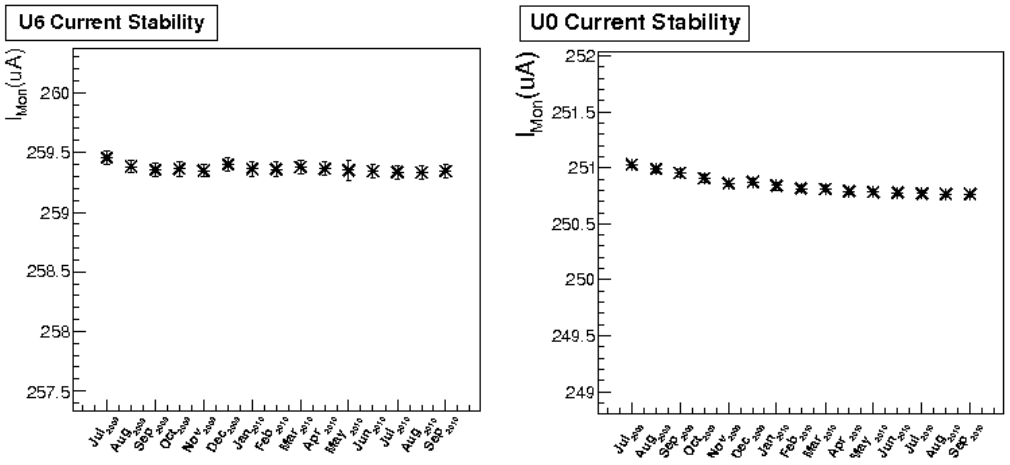

Figure 4.22: Current trend plots of U6 and U0 columns

4.7 The noise analysis

Noisy columns are in limited number, but they cannot be neglected. In this second analysis the main important point is to try to estimate the noise behaviour and study its evolution over time.
In Sect.4.4.3 different types of noise were described, but the analysis is relevant only for the constant and bunch noises. Glitches are included but have well separated points far away from the mean signal value.
As described in Sect. 4.5 this method emphasizes noise contribution on the second gaussian with a larger standard deviation. To appreciate the study two examples of noisy columns are reported in this section: D2 and U6.
To better understand the following plots a deeper description of the sample and archiving method must be done.
Tab. 4.2 listed the archiving settings used by the different projects. Considering log file data for the analysis, basically two settings have been used. The first one is a recursive archiving every 5 min. The second one was introduced to detect under–current, over–current and voltage effects. In this case the system archives data if at least one of the two values deviates by more than ± 10 V or ± 5 μA with respect to the previous sampled values.
As described in the previous section, data points were fitted using a double gaussian distribution. The noise contribution is completely described by the larger gaussian distribution.
To establish if a column is noisy a ratio percentage is calculated.
From the fit it is possible to evaluate the event number corresponding to each contribution. Noise is calculated as follow:

$$Noise = \frac{N_{NoiseEvts}}{N_{TOTEvts}} \tag{4.6}$$

where $N_{NoiseEvts}$ is the noise event number, $N_{TOTEvts} = N_{NoiseEvts} + N_{SignalEvts}$ and $N_{SignalEvts}$ is the number of signal event number. We define a column as noisy if the ratio exceeds 3%. This noise study has an intrinsic bias due to the sampling method resulting in a noise over–estimation.

If a column is noisy the overthreshold sampling is more frequent than the 5 min or constant sampling. This is represented with a higher number of noisy events compared to signal points. The real weight can be appreciated looking at the constant sampling data points far from the main signal peak. Noise should be equally distributed over the whole range. Considering Fig. 4.23, the real noise contribution should be done by all events in the two ranges (with few points) close to the signal peak not considered by the fit. This behaviour is known but, at this level, it is not considered in the noise calculation. The choice was done thinking to the experimental operations. Trend plots obtained are the same used by the users to check the RICH status. They are used to control any possible HV deviation from the nominal behaviour. The detected noise is what they can appreciate.
The relevant aspect is that the noise is less frequent than the observed one. In the following subsections there are two examples to better understand the study. As all the other columns, U6 was stable just after the refurbishment done in July 2009. It started to be noisy from February 2010.

Column U6

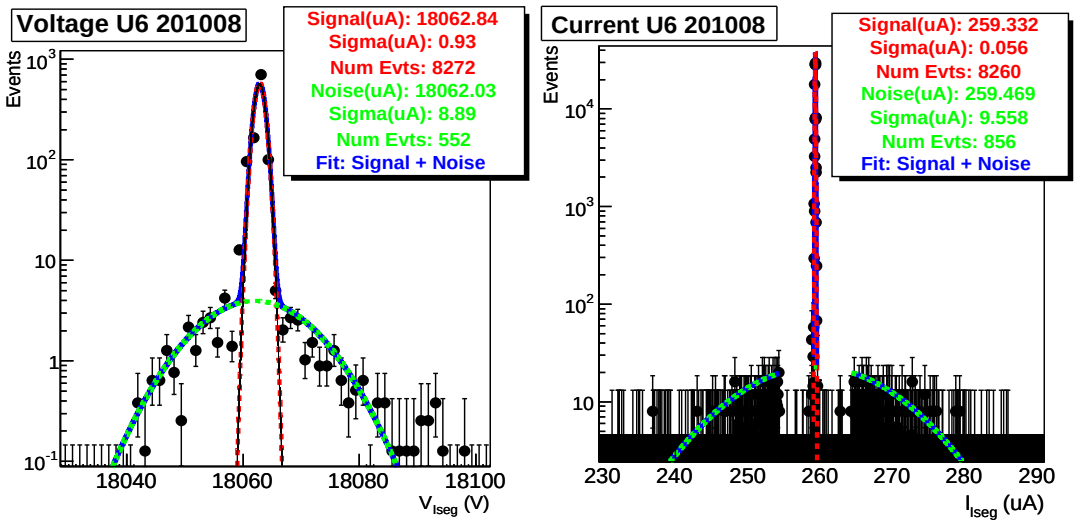

Figure 4.23: Voltage and Current fit with a double gaussian. In blue the total fit, in red the gaussian fit of the signal and in green the noise gaussian

The shape previously described is shown in Fig. 4.23. In the left plot, the voltage histogram shows the double gaussian shape. Slightly different is the current histogram on the right. The main signal peak is in the center surrounded by two gaps, filled with few events. For larger values, there are overthreshold or noisy events. These three features can be described in this way: the main narrow peak is the signal peak randomly sampled. The two gaps, large 5 μA each surrounding the main signal peak, are noisy events randomly sampled. They indicate the real impact noise as described before. The two ranges at values larger than 5 μA (threshold value) from the main peak, are noisy points. They are used to evaluate the noise gaussian contribution.

For the noise analysis it is not correct to weight all these ranges in the same way. The solution is to exclude, from the fit, the gap zones. In that way it is possible to consider correctly the archived noise behaviour. Demonstration is the blue curve of the total fit. It is superimposed to green and red curves, that well describe data points.
Noise trend plots of this column are reported in Fig. 4.12. The column exceeds the noise threshold (set to 3%) after a few months since the refurbishment. The noise percentage increases with time for both voltage and current. The increase behaviour displayed indicates a correlation between current and voltage. A current noise event induces a change in the voltage and viceversa. This is another demonstration of an HV internal cause. This means that the effect is real and related to the supply system.
Another important aspect is the air flow improvement of March 2010. It does not seem to reduce the noise rather than the test made in laboratory, but stability has apparently improved.
The HV module of this column was replaced in November 2010.

Column D2

Another example of constant noisy column is given by D2. Also in this case it does not show noise after refurbishment. In Fig. 4.24 noise plots display a fast and large voltage degradation. The decision was to change the power supply, on 27 September 2010. After the intervention this channel became stable.
Fig. 4.25 shows its performance. The voltage shape is the expected one, a double gaussian

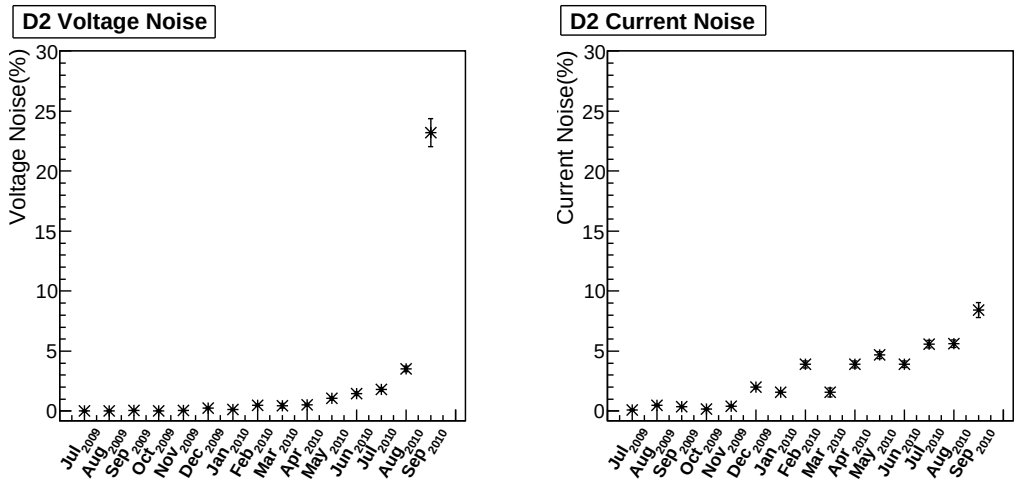

Figure 4.24: Percentage of the noise in function of the time for the voltage, on the left, and for the current, on the right of column D2

distribution. The current plot, on the right, appears different from the U6 case. It shows the current signal peak, two 5 μA gaps apart and the noise signal tails. The main difference from U6 case is the gaps filled with several events. They have two well defined peaks at ± 1 μA and ± 3 μA from the current mean value. The last gap part (from ± 3 μA up to ± 5 μA) is empty.
As described before, this range is excluded by the fit to not introduce systematics in the noise evaluation. Also in this case this range was not considered, but a deeper analysis was

done to try to better understand the behaviour.
There are two possible reasons which can explain these points. The first one is the 5 minutes sampling interval and the second should be a voltage effect.
Fig. 4.26 shows voltage and current plots obtained applying different selection criteria. The three different colors represent the three main sampling methods. Blue data are events with current values above $I_{Thr} = \pm 5\ \mu$A. The corresponding voltage points are spread over the whole voltage spectrum. Considering voltage plot, green points are 5 minutes sampled data. They correspond to the main current signal peak and include the two adjacent peaks. The few red points have voltage values larger than $V_{Thr} = \pm 10$ V and they are the main current noise contribution.
Fig. 4.27 shows the previous plot with different selection criteria applied. Taken into account current plot, green and red points are the two current peaks detected in each gap contributions. Considering voltage plots these points correspond to voltage values in the tails of the main signal, causing a wider gaussian shape.
As a consequence a correct evaluation of the noise is very difficult. In fact, in the current fit peaks in the gaps are not considered and evaluated, but voltage fits include their induced modifications.

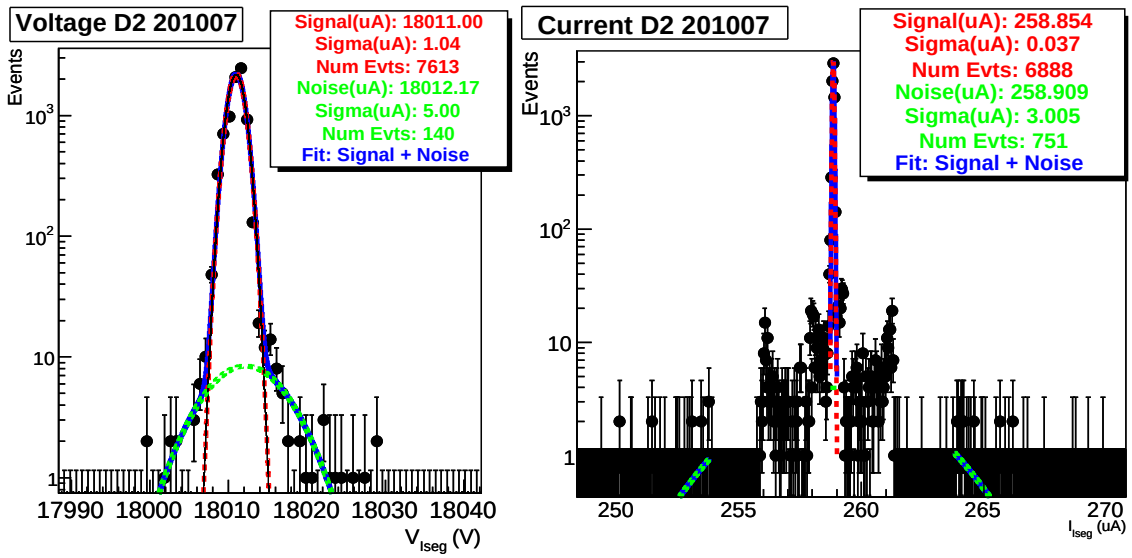

Figure 4.25: Voltage and Current fit with a double gaussian. In blue the total fit, in red the gaussian fit of the signal and in green the noise gaussian of column D2

Column A0

The last example is column A0. It was noisy since the July 2009 refurbishment. Its characteristic is the "bunch noise" previously displayed in Fig. 4.13 and described in Sect. 4.4.3. The unit was substituted in April 2010. The new power supply is a single cabled and commercial ISEG module with an external splitter. After the substitution voltage and current are stable.
Fig. 4.28 shows the noise percentage trend plots of voltage and current. For both of them an

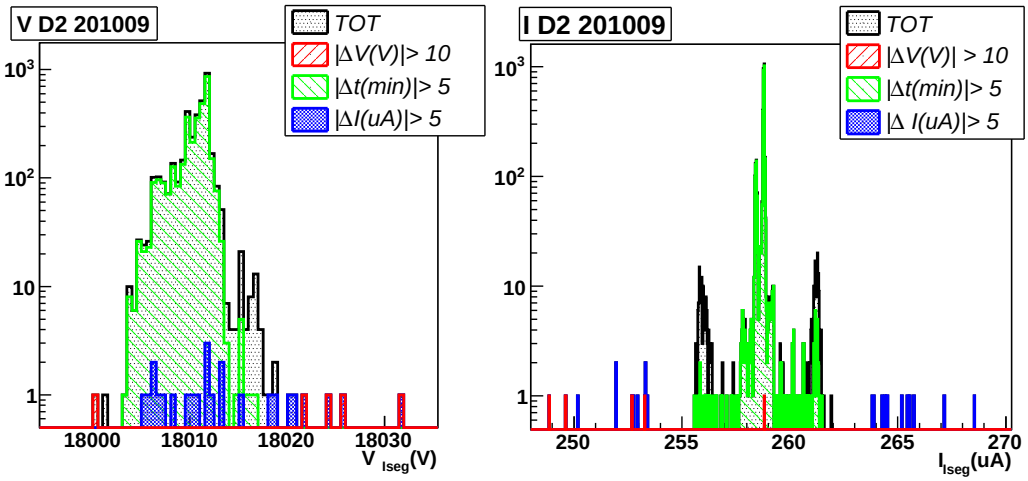

Figure 4.26: Plots of the voltage, on the right, and of the current on the left for the D2 column for July 2010. Different contribution are evaluated. The black contribution is the total of all the events at the plateau. In red the contribution of the events detected having the voltage value above the voltage threshold. In blue all the events above the current threshold. All the differences are obtained considering the mean value of the fitted signal in Fig. 4.25

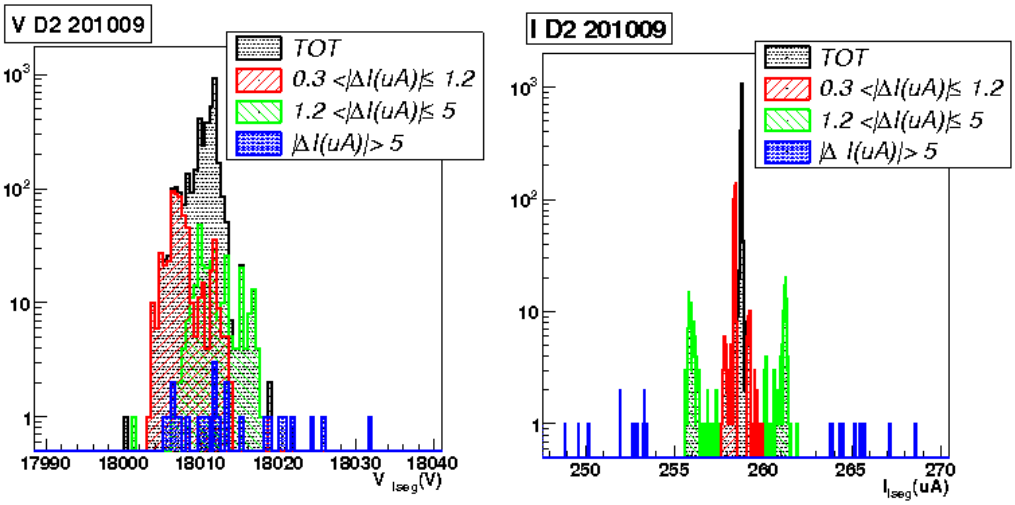

Figure 4.27: Plots of the voltage, on the right, and current on the left for the D2 column. The black is the contribution of the total events of the time range taking into account. Considering as the signal value the mean value of the fit in Fig. 4.25, in red there are all the events with a current larger in the range $0.3 < \Delta I(\mu A) \leq 1.2$. In green there is the contribution of the events with $1.2 < \Delta I(\mu A) \leq 5$. In blue all the events above the setting current threshold for the storage, $\Delta I(\mu A) > 5$

increase in time of the noise is shown. On the right voltage plot, a maximum was reached in March 2010 with 22.8% of noise. In April, the noise slightly decreases (18.2%), a consequence of the air flow improvement in the rack. This behaviour is not seen in the current plot. It increases quickly reaching 56.4% in April 2010 before the refurbishment. Considering the noise behaviour there is not only a noise percentage increase, but also a standard deviation growing. This effect is shown in Fig. 4.29. The noise becomes more frequent and

its glitches have larger amplitudes. This effect becomes more important with time and reduces the system stability. The only solution was the unit substitution.

Every unit has its own operational voltage and current values displayed in Fig. 4.29. In the

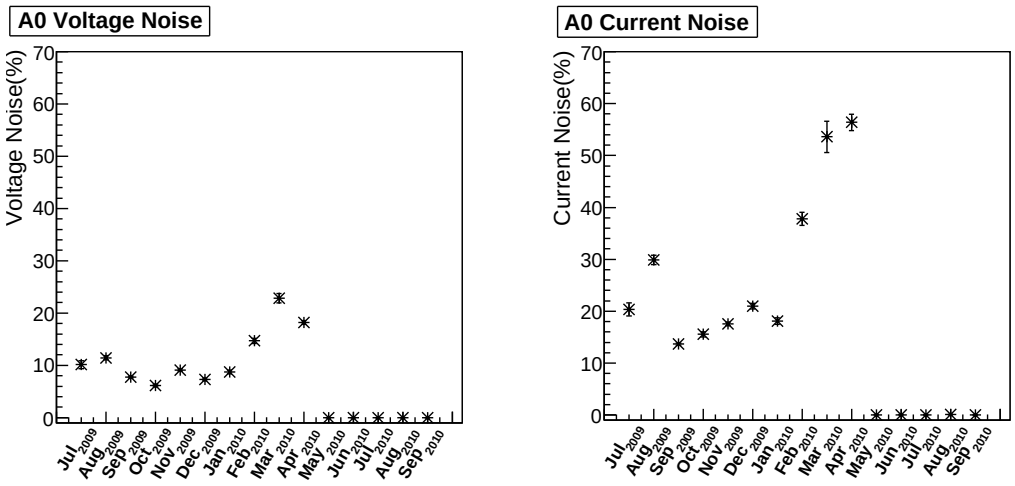

Figure 4.28: A0 Noise percentage. On the right voltage and, on the left, current trend plots

	Voltage(V)	**σ(V)**	**Current(μA)**	**σ(μA)**	**Noise$_I$(%)**	**Noise$_V$(%)**
Before	18050.2	1.7	259.30	0.59	56.4	18.2
After	17731.8	1.1	253.58	0.07	0	0

Table 4.4: A0 fit value obtained before and after the HV power unit substitution

two plots mean values changed from April to May 2010. This is the gap due to the HV unit substitution.

After the refurbishment, standard deviations are very small and values are stable. Before the substitution, the behaviour is completely different.

Considering the left plot in Fig.4.30 is visible the standard deviation increase. This is a system degradation symptom. The same behaviour is also seen in the voltage plot shown in the right zoomed plot in fig. 4.30. The voltage operational value after the substitution is reported in Tab. 4.4.

The noise increase affects the stability of the column. During time this noise increase its frequency and the bunch lengths. It also induced two different behaviours. The first is small glitch amplitudes which enlarge signal distribution. The second effect is the increasing of the noise standard deviations. These glitches with bigger voltage and current amplitudes reduced the stability and the reliability of the channel.

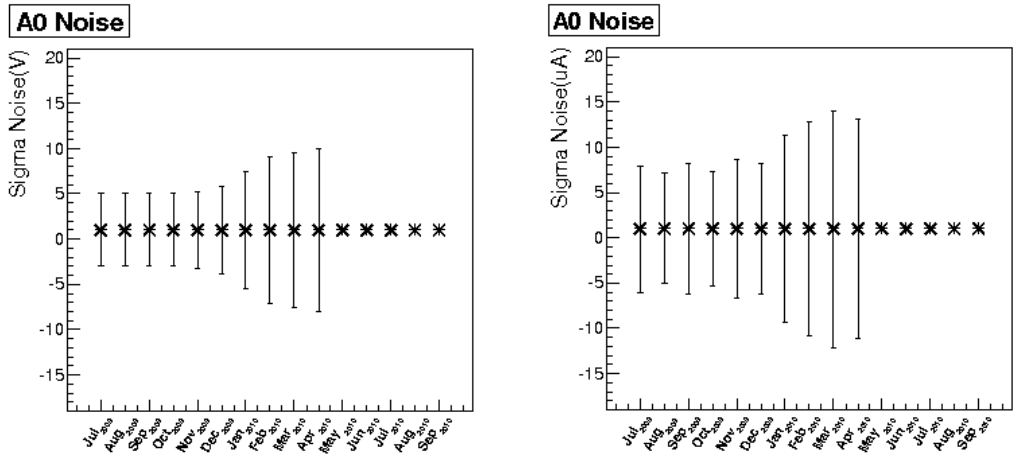

Figure 4.29: A0 standard deviations. The increase of the standard deviations follow the increase of the noise percentage for both voltage and current

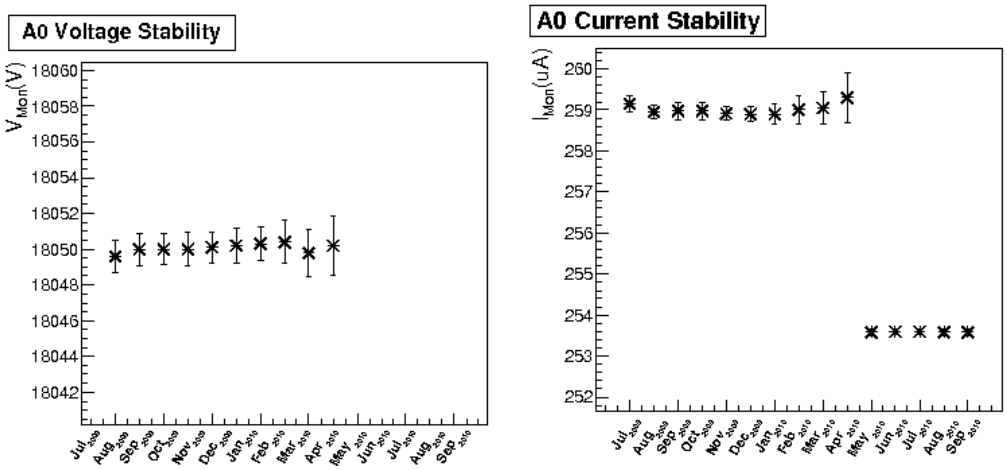

Figure 4.30: On the left: voltage stability plot. It is zoomed about the operational value before the supply unit substitution (the new voltage values, after the substitution, are out of scale). In evidence the standard deviation increase. On the left: current stability plot

4.8 Final results and conclusions

The VHV system has been fully analyzed and characterized in terms of stability and noise. Most columns are stable with very good operational conditions.
During the period considered system debugging and alarm optimization were completed to guarantee the RICH safety needed. Consequently voltage and current were investigated. Detected effects were taken into account considering the RICH system safety and stability. The most relevant are saturation spikes and noise.
For both of them it was possible to restrict the cause to the VHV supply unit. From this study the most probable cause is the potting material used. It protects and shields the internal splitter avoiding possible breakdown discharges. This hypothesis is supported by the manufacture of new power supply units, already operational, with new potting material.

Considering the described method, it was possible to study, independently, stability and noise behaviours.
Fig. 4.31 shows voltage and current distributions for all columns and for the whole period considered. Values obtained are comparable with the test done before the installation at the

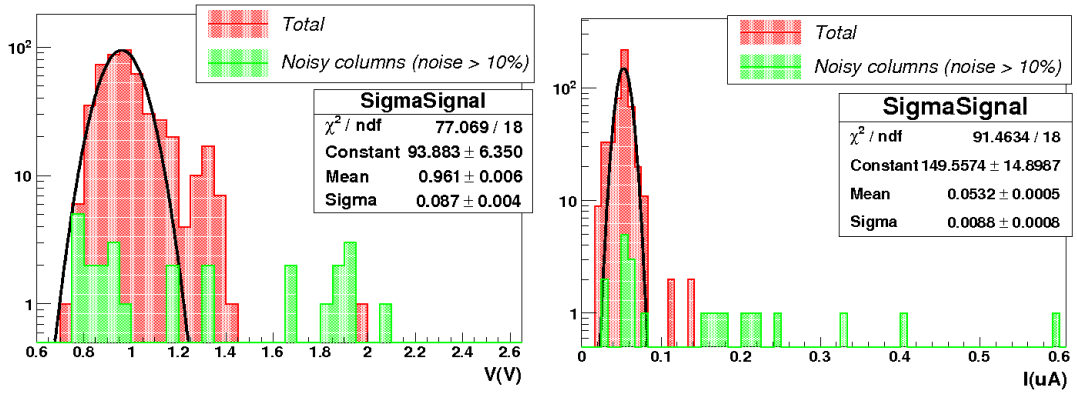

Figure 4.31: Voltage and current resolutions for all columns. In red all the fit considered. In green value from very noisy columns (limit fixed to 10%). Points far from the gaussian mean are due to these very noisy columns. On the left: voltage. The second main peak at 1.3 V is due to columns A2, A6 and C2. A2 and A6 are good columns with the only exception of a wider voltage gaussian distribution. C2 is one of the problematic column described before. On the right: current

pit [115].
With a noise threshold set to 3 %, 12 % of the units show a voltage noise and 15 % a current noise. This analysis is useful to understand the system behaviour and reliability.
New batch production units are in place (one is operational in column D2) and other will be substituted soon. This intervention is planned to complete the RICH system optimization guaranteeing high quality during data taking.
Units still in place are giving a positive feedback, but more time is needed to appreciate their operational behaviour.

CHAPTER 5

A NEW POSSIBLE PHOTONDETECTION SYSTEM FOR THE RICH UPGRADE

The ring imaging Cherenkov detector is now readout by hybrid photon–detectors. In view of its upgrade a possible option is the adoption of a flat panel multi anode photon–multipliers tubes [99]. An important requirement for a good Cherenkov rings reconstruction is a limited level of cross–talk. The cross–talk from the 16×16 *pixels of the Hamamatsu H9500 PMT has been studied. Results have shown that for the single photon signal, as expected in a ring imaging Cherenkov detector, the statistics tied to the small number of electrons generated at the first dynode of the photon–multiplier chain, leads to a number of CT signals that are a small fraction of those of fired pixel. Due to the discrete nature of the electron charge, those few cross–talk signals have amplitude that could be a significant fraction of the main signal.*

5.1 The LHCb upgrade

LHCb was designed to work at a luminosity of $\mathcal{L} = 2 \times 10^{32}\text{cm}^{-2}\text{s}^{-1}$ with ~ 0.7 interactions per bunch–crossing rate of ~ 30 MHz [126]. Due to the LHC bunch structure and luminosity, the LHCb crossing frequency with visible interactions, detected by the VELO and the T stations, is about 10 MHz [81].
The necessity to obtain more statistics for the B–physics studies, to be more sensitive to flavour observables and to reach new physics probes through loop processes, suggests the idea to upgrade LHCb [127, 128]. It will operate at ~ 5 times the foreseen luminosity, therefore at $\mathcal{L} = 10^{33} cm^{-2} s^{-1}$.
The machine can deliver a luminosity of $\mathcal{L} = 5 \times 10^{33}\text{cm}^{-2}\text{s}^{-1}$, a factor 20 times larger luminosity than that LHCb was designed.
If at the nominal luminosity the expected rate is ~ 10 MHz, with the upgrade there will be 40 MHz of data available. This means that LHCb has to read data at 40 MHz from all the detectors.
The relation between the number of crossing and the number of visible interaction is shown

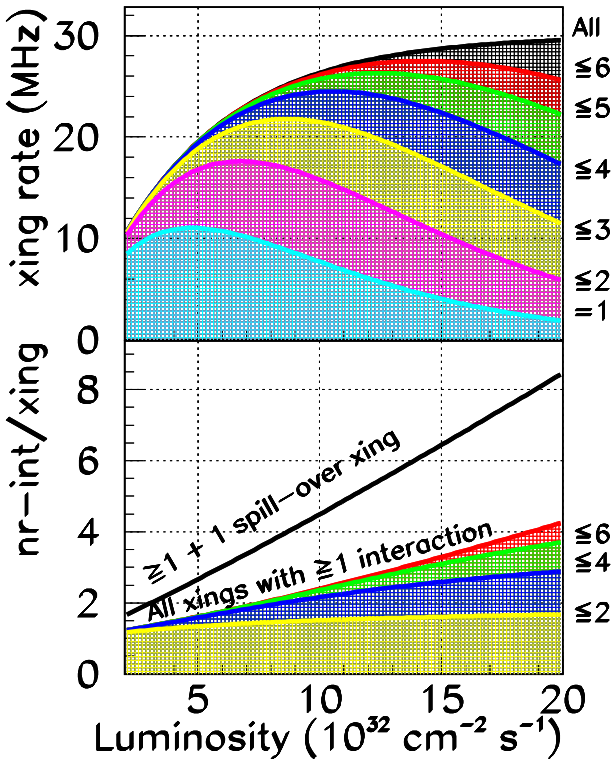

Figure 5.1: Top: number of visible collisions as a function of the luminosity. Bottom: average number of visible *pp* collisions, per event, with at least one *pp* interaction [127]

in Fig. 5.1. This graph shows the number of crossings on the top graph and the mean number of visible interaction per crossing with at least one visible interaction as a function of luminosity.
An important aspect to be taken into account is the increase of the detector occupancy. Some detectors, as the RICHes, are sensitive to the occupancy level. The pile–up is not the only relevant effect, also the spill–over must be considered which increases linearly with luminosity.
The pile–up effect is the existence of an additional pp interaction in a given bunch crossing and the spill–over is the effect referred to hits coming from preceding and/or following bunch crossings.
This luminosity increase involves also some upgrades of the whole front–end electronics to read out the detector at 40 MHz and the development of a more radiation hard vertex detector sensor technology.
As a consequence, the whole acquisition architecture [129] must be re–designed.

5.2 The multi anode photomultiplier tube

The particle identification is an important aspect of the LHCb experiment and increasing the luminosity by a factor of 5, from 2×10^{32} to 10^{33} cm^{-2}s^{-1}, results in a factor 2.3 increase in the detector occupancy as shown in Fig. 5.1.
The RICH detectors need that HPDs front–end, at present encapsulated in the vacuum tube,

is changed to satisfy the new requirements. This implies the photon detection system replacement with a new photon–detector and a new front–end electronics, on which the The Milano group is involved.
The idea is to test a commercial Multi anode Photon Multiplier (MaPMT): two candidates

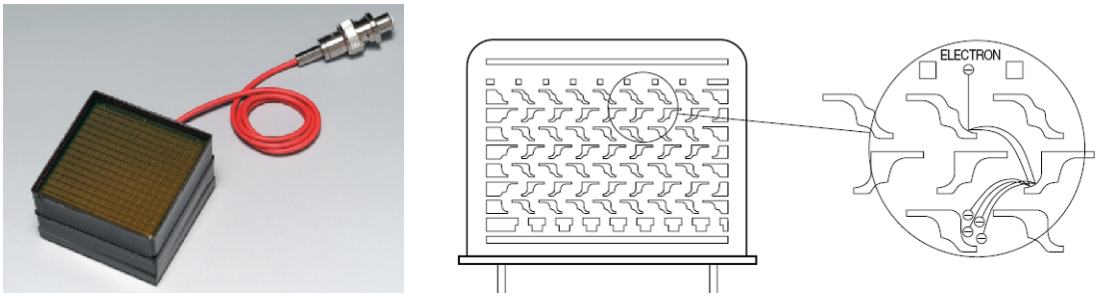

Figure 5.2: On the left: the Hamamatsu H9500 with high voltage cable and connector. On the right: schematic view of the MaPMT with its dynodes multiplier chain

are the Hamamatsu® H9500 and R7600. Results obtained from the first are reported in the following section. A schematic drawing is shown in Fig. 5.2.
The choice for a new phototube must consider as relevant requirements the granularity, the fast acquisition and the economic aspect.
The H9500 has a flat window with a bialkali photocathode, a focusing system composed of 12 steps of multiplying dynodes and a pixelized anode. For the dynode chain the supply voltage can be -1100 V and the current consumption is lower than 200 μA, dissipated by the resistive divider chain.
The spectral response covers the wavelength range of 300–650 nm, that satisfies the requirement of a high granularity, with a matrix of 16×16 pixels anode with an effective area of 9 mm^2 each and a low CT of 5 % obtained illuminating the phototube with a signal containing a large number of photons.
In the following section there is the description of the experimental set–up used to test the photomultiplier and the results obtained.

5.3 The experimental set–up

The Cherenkov signal from the RICH contains about 20 photons distributed along a ring as reported in Tab. [3.1]. Each photon hits a single pixel whose signal gives the ring pattern.
The characteristics of the PMT need therefore to be tested to the single photon response.
The acquisition system adopted for this study was designed and tested for the BTeV experiment [130, 131].
The front–end board, shown in Fig. 5.3 is a printed circuit board hosting two monolithic 64 channels VA64MaPMT ASICS chips developed by IDEAS [1]. The analog inputs are routed via flat cables to the MaPMT photon–detectors dynodes.
Both hybrids incorporate level shifter circuits that translate the current output from the ASICs into voltage requirements of the XILINX FPGA, used to initialize and to transfer

[1] www.ideas.no

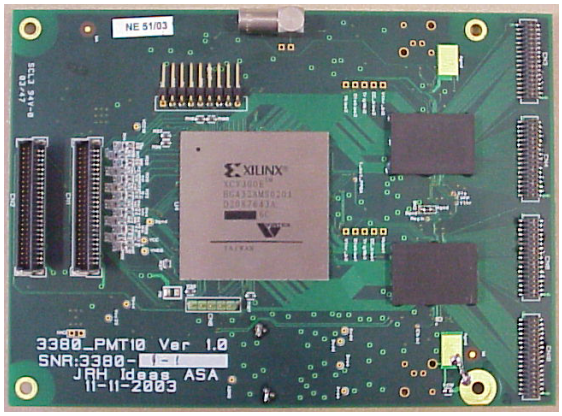

Figure 5.3: Front–end board with the FPGA and the two VA64MaPMT ASICS chips, on the right, mounted on it. It is a printed circuit board with 64 mixed analog and digital processors with parallel inputs and parallel outputs [131]

data to the back–end circuit.
All the 64 analogue channels are composed by a charge sensitive preamplifier followed by a CR–RC like shaping filter having about 70 ns peaking time. A comparator is AC coupled to this filter. The triggering threshold voltage is common to each comparator of the chip and can be set at an input pin. A fine tuning of the threshold to each channel is possible by means of few bits DAC, one per channel embedded in the chip, that is able to add/subtract a current to a corresponding resistor in series in the chip to the above pin.
This version of the front-end chip used does not have analog outputs.
Digital output from the chip is processed by a FPGA and sent to a PCI board developed at FERMILAB. The set–up dumps, when full, a memory present on the FPGA board filled with the trigger hits from each channel. The memory is written at every given reading–strobe that can be set in a window range from a few Hz up to tens of KHz.
Evaluation of CT and noise [132, 133] were done measuring the rate of the signals as a trigger threshold voltage function, as explained in the next section.
At the beginning it is necessary to calibrate the system. The calibration is done injecting at the preamplifier input a known charge through a test capacitance. Fig. 5.4 shows the threshold voltage, Vth, as a function of the injected charge. Vth was the level for which the frequency of the acquired signals dropped to half maximum. As can be seen the saturation of the input preamplifier is just above 4 Me^- (e^-=electron). Using this method, the response to a single photon event was available for the study.
Considering the MaPM structure, a clusters of 9 pixels was selected to study the CT: a central pixel and its 8 lateral neighbors, as shown in Fig. 5.5. The coloured pixels have the highest probability to detect the induced cross–talk signals.
A black plastic mask of 1 cm thickness with 256 holes, patterned like the pixel matrix (top right of Fig. 5.6), was put in front and in contact with the PMT window. All the holes were covered with a black tape except the central pixel of the selected cluster. A commercial 1 mm diameter optical fiber was fitted in the hole on one side. On the other side it was tiny coupled to a blue diode that simulates Cherenkov light. The diode was biased just above threshold to generate a very small amount of light with a low rate of few Hz. The arrange-

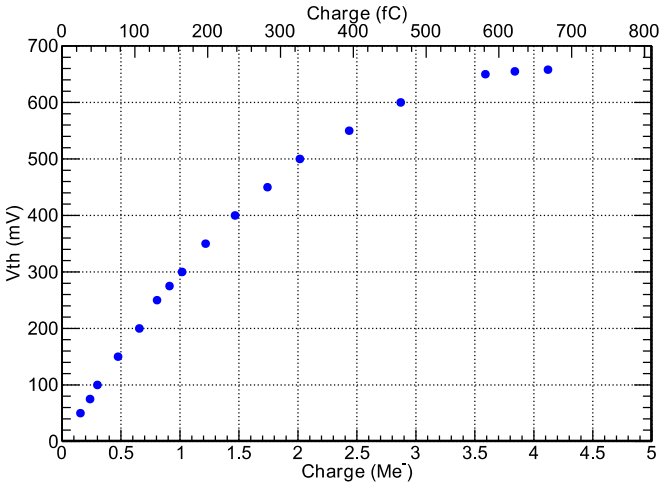

Figure 5.4: Calibration of one channel of the VA64MaPMT. The threshold is calibrated as a function of the input charge expressed in Me^- (e^-=electron) at the bottom, and in femto–Coulomb (fC) at the top

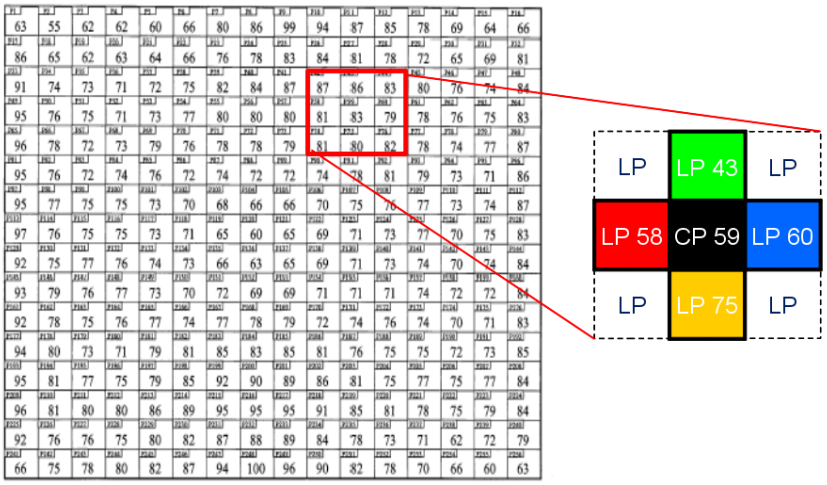

Figure 5.5: Example of a cluster of pixels readout for the CT and noise studies

ment allowed lighting only the central pixel of the cluster. The PMT was also put inside a light-tight metallic box and for further precaution a thick black–cloth covered completely the box. The whole experimental set–up is shown in Fig. 5.6. Very short shielded connections were used from the PMT to the external of the box where a short high-density flat cable was connected to the front–end. A fed through 25–pins connector was used on the box and the whole set–up was put inside a Faraday cage.

For an accurate characterization any possible CT coming from a source other than the pixels must be suppressed. The connecting links are the main source of additional CT, whose level depends on the input impedance of the charge sensitive preamplifier. A characterization of the high–density flat cable that connects the preamplifier input was done. A test charge was injected at the input of one channel and a fake signal was read at the channel outputs connected to the adjacent wires on flat cable. Without connecting the PMT. It was

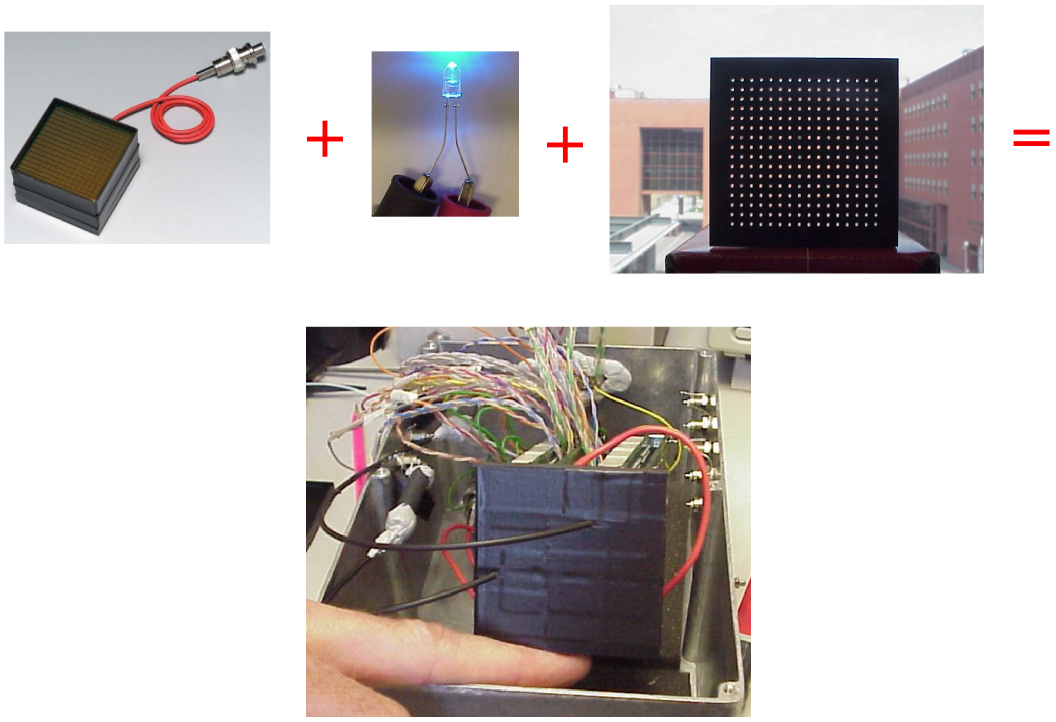

Figure 5.6: Set–up used for the tests. The MaPMT used, the blue commercial LED used as a light source and the mask wit 256 holes made up the set–up under study. In the bottom, there is the total assembled set–up inside the metallic box. It is evident the optical fiber enlightening the central pixel of the cluster under study

verified that the CT started to be seen when input charge was about 1.1 Me^- for a 25 cm flat cable and 2.4 Me^- for a 10 cm flat cable. To suppress this contribution the 9 pixels of the clusters under study were connected one every 5 wires of the flat cable. This configuration assures that their contribution to the adjacent pixels was negligible. A similar pattern was adopted also for the 25–pins fed through connector.

5.4 The characterization of the PMT with a single photon signal

The set–up described in the previous section was used not only for CT study but also to evaluate the signal response. The output from the VA64MaPMT is a digital signal that indicates only if the output of the corresponding channel had exceeded the trigger threshold. Considering the single photon response as a gaussian distribution and fixing the threshold Vth, it is possible to count all the signals in the distribution above it. The frequency of the events was set smaller than the capacity of the reading strobe. Mathematically this is equivalent to evaluate the following integral:

$$F(V_{th}) = \int_{V_{th}}^{\infty} N(V)dv = \int_{0}^{\infty} N(V)dv - \int_{0}^{V_{th}} N(V)dv \tag{5.1}$$

Where $N(V)dv$ is the part of signal that can be found with amplitude between V and

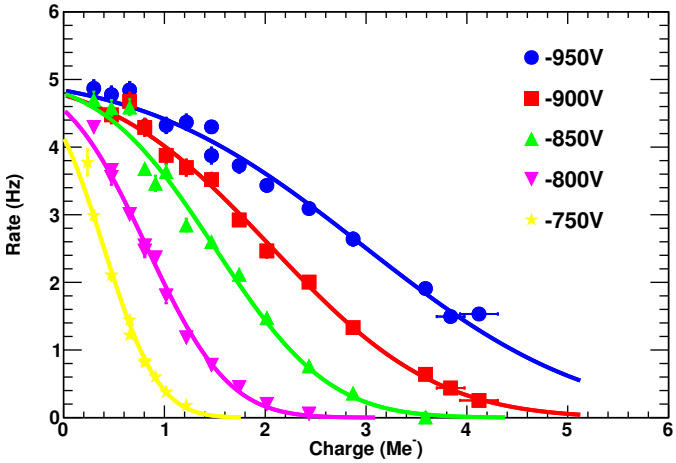

Figure 5.7: Frequency of the triggered events from the central pixel as a function of the trigger threshold, expressed in Me^-, taken at different biasing voltages of the H9500. The fit was obtained considering Eq. 5.1

$V + dV$. Fig. 5.7 shows the signal rate as a function of the trigger threshold.
The curves were obtained at different values of the PMT biasing voltage, which ranged from -750 V to -950 V.
The smallest bias level was selected to have the lowest acceptable signal to noise ratio, while at the larger bias we found the limit of the set–up dynamics.
In Fig. 5.7 the fitting curve $F(V_{th})$ of Eq. 5.1 is superimposed to data. In Fig. 5.8 the

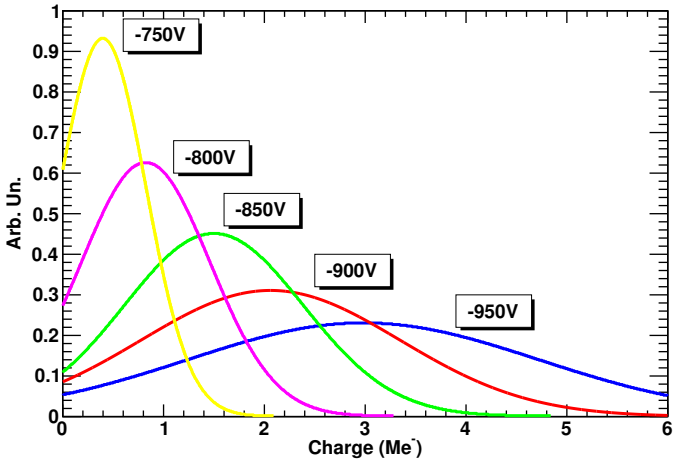

Figure 5.8: Gaussian distribution functions $N(V)$ that better fit data of Fig. 5.4 using Eq. 5.1

gaussian distributions $N(V)$ of Eq. 5.1 that fit the corresponding data is shown. In the measurements the smaller trigger threshold considered was that just above noise. Tab. 5.1 is a summary of the characteristics of the curves of Fig. 5.8 where there is an evidence of the signal dependence on the PMT bias voltage.
In Fig. 5.9 the response to the single photon is shown as a function of the PMT bias voltage. When the photoelectron emitted is accelerated and strikes the first dynode, it produces secondary electrons. These electrons, following the same procedure, emit other electrons re-

Bias (V)	750	800	850	900	950
Signal (Me$^-$)	0.399	0.826	1.500	2.061	2.982
Sigma (Me$^-$)	0.429	0.638	0.886	1.283	1.735

Table 5.1: Single photon peak position and resolution of the fitting single photon response of Fig. 5.8 as a function of PMT bias voltage

peating the process at every following dynode, as shown in Fig. 5.2 achieving a large charge amplification.
The gain is the ratio of the anode output charge to the photoelectron from the photocathode, for the MaPMT considered is in the order of 1.5×10^6.
Considering a photomultiplier tube with $n = 12$ dynode stages, the gain is described by [134]:

$$Q_{el} = K\left(\frac{|V|}{n+1}\right)^{\alpha n} \tag{5.2}$$

Where from the fit $K = 6.19 \times 10^{-15}$ Me$^-$/V$^{\alpha n}$, V is the biasing voltage and $\alpha = 0.66$ a coefficient determined by the dynode material and geometric structure. The accuracy of the fit was limited by the dynamic range in Fig. 5.4 of the setup that loses linearity above 3.5 Me$^-$.
Eq. 5.2 puts into evidence the strong dependence of the signal to the applied voltage.
In Fig. 5.9 the measured gain is shown as a bias voltage function. Data are fitted with Eq. 5.2.
Also an empirical exponential works fine in the range considered:

$$Q_{el} = a + b^{c|V|} \tag{5.3}$$

where parameters $a = -1.76$ Me$^-$, $b = 0.11$ Me$^-$ and $c = 3.94$ V^{-1} are obtained from the

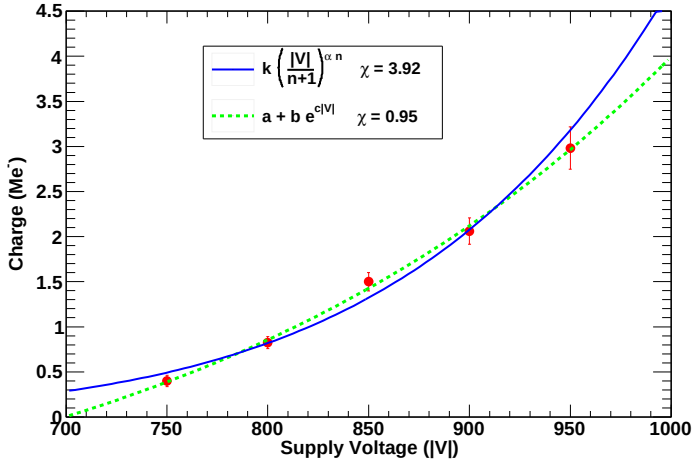

Figure 5.9: Charge gain in response to single photon as a function of the PMT bias voltage for the H9500

fit with green line in Fig. 5.9.

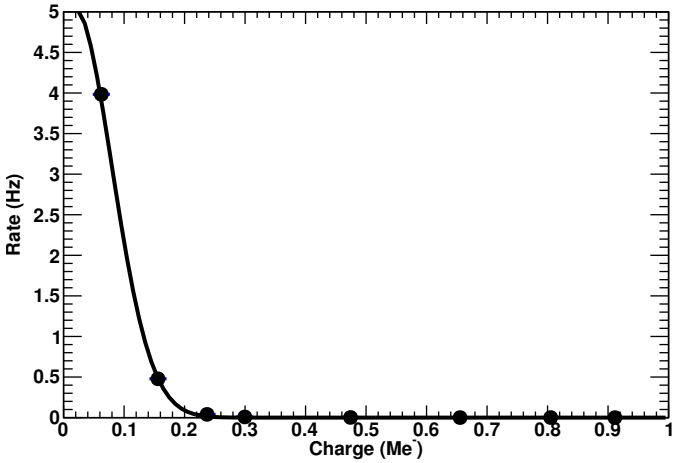

Figure 5.10: Plot obtained, for one channel, without any light source. It represent the dark count rate

The response curves of Fig. 5.8 have the mean values consistent with the gain measured for continuous light. The rate of the signals from the LED, biased with a fixed voltage value, remains constant varying the reading–strobe from a few Hz up to a few tens of KHz, giving an indication of the absence of pile–up. These considerations prove that the set–up was able to generate and read single photon excitations.
To study the noise spectra, measurements have been done also when the LED source was off. In that case only noise and dark current are collected and the obtained signal spectrum is shown, for one pixel in Fig. 5.10. For this test the trigger threshold was limited to a range for which the rate resulted smaller than the sample rate, as for the signal case.

5.5 The study of the cross–talk

The statistics that regulates the Cross–Talk (CT) from a single photon response in a PMT must consider the mechanism of generation of the electrons at each dynode.
When a photon enters into the quartz window of the PMT a photoelectron is generated. This photoelectron is accelerated by an applied field to hit the first dynode. A few electrons, Poisson distributed with mean at about 3.5 e^- [134], are generated. Each of such a new generation of electrons are driven toward a second dynode by the electric field. Each electron will rise a new generation at this second stage. The process continues at each stage of the dynodes chain. In the H9500, 12 stages are present before the final anode collects all the charge. The final gain is in the order of few Me^-/photon.
Let's consider a possible small non–uniformity in the geometry of the dynode structure, in Fig. 5.2 and/or electric field applied. An electron traveling to a dynode, has a small probability to change direction toward a lateral dynode. This electron generates, at the end of the chain, a detectable CT signal.
As first approximation any dynode and any electron have the same probability to undergo this process. Nevertheless, due to the multiplication mechanism described, the first and the second dynode of the chain are those susceptible to give origin to the largest CT signals.

Two situations, illustrated in Fig. 5.11 are possible.

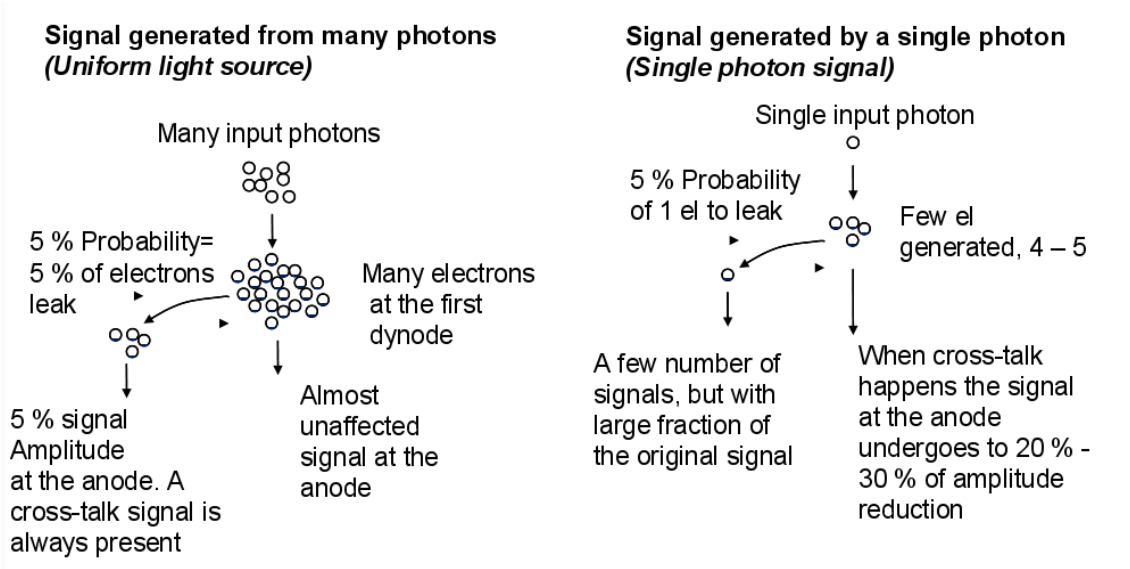

Figure 5.11: Statistical model of signals. On the left: signals generated from many input photons. On the right: signal generated from a single input photon. In both cases p is the CT probability while G the gain of the multiplication

In the first case, left panel, many photons, at the same time, hit the input quartz window at the same pixel position. A similar number of photoelectrons is created and at the first dynode generates many secondary electrons K. Considering p the probability that an electron changes its direction traveling to the following stage of the chain and taking into account $p \ll 1$ and $pK > 1$, on average, pK is the number of electrons deviating from the original direction. These electrons generate, at the end of the chain, a CT signal that is p times smaller than that of the central pixel.
This signal is present every time a large number of photons hit the pixel, or every time $pK > 1$.
The second cause is when only one photon hits the pixel (right panel of Fig. 5.11). In this case only J electrons are generated, with J a few units, and $pJ < 1$. This means that not all signals generate CT. On average, a cross-talk signal is generated every $1/pJ$ single–photon events. For most of the times only one electron generates a CT signal that is a significant fraction of the inducing signal having 20% or 30% of the original amplitude.
As described in the previous section, single photon signals were generated and collected. In this study only events, from the lateral pixels, in coincidence with those coming from the central pixel were considered. This is done in order to suppress, as much as possible, contribution from noise and dark current. The probability pJ shown in Fig. 5.11 can be appreciated from Fig. 5.12, where the histogram of the central pixel and the 4 colored lateral pixels in the cluster example of Fig. 5.5 are shown when the trigger threshold is set just above noise. From the measurement a value of about $pJ \approx 2.9\%$ was obtained. The total probability from the 4 lateral pixels is 11.5%.
To interpret the phenomena a simulation was developed. Fig. 5.13 shows that CT extends in amplitude to a significant fraction of the signal from the central pixel.

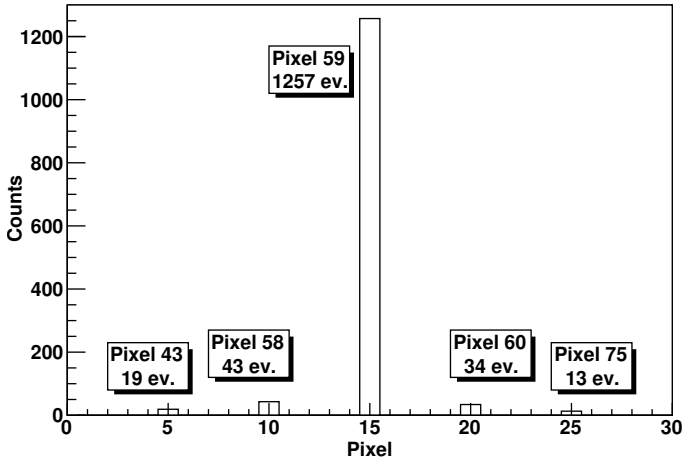

Figure 5.12: Histogram showing the number of counts for the central pixel and the lateral pixels. The ratio of the two counts is the CT probability. PMT biased at 900 V

The CT signals percentage is not negligible up to large amplitudes.

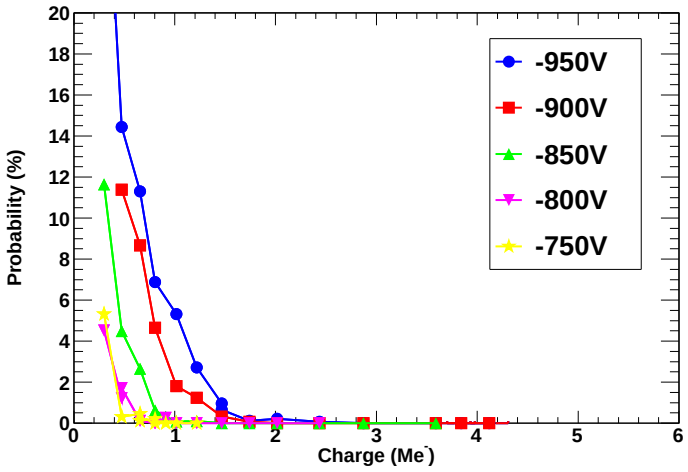

Figure 5.13: Cross–talk signals in coincidence with the central single photon signal

It can be seen that by increasing the trigger threshold the cross-talk probability decreases, but the rate of the inducing signal decreases as well. This is evidenced in Fig. 5.14 where the signals from central pixel and the sum from all the laterals are plotted. Superimposed to the measurements are the simulated curves that match data fairly well.
Tab. 5.2 shows an estimation of the loss of signal as a function of the trigger threshold for the PMT under test when biased at -900 V. In Fig. 5.15 measurements are shown where the percentage of missing signal is plotted with respect to the percentage of CT signal.
CT amplitude is not negligible for the H9500 PMT but the probability that it happens only $\sim 10\%$ of cases. As an example, in the RICH of LHCb a ring contains about 20 photons: a CT signal is expected for only a couple of pixels in average.
Taking into account this effect, the MaPMT H9500 can be considered a possible candidate for the HPD replacement.

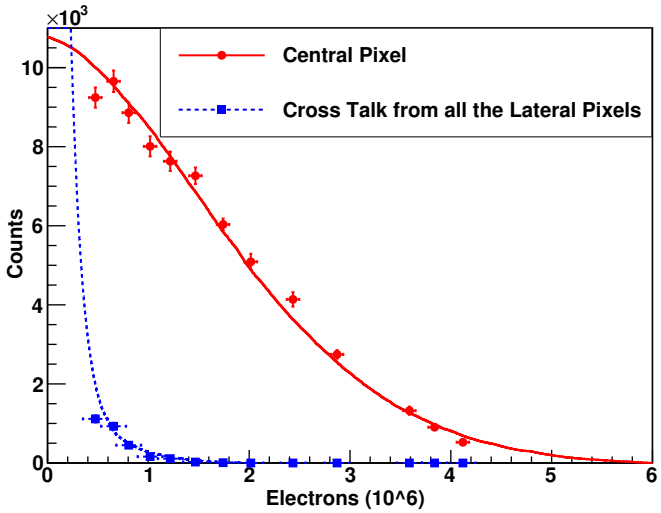

Figure 5.14: Comparison between measured CT signals and inducing signals

Threshold(Me^-)	*Main signal lost (%)*	*CT signal detected (%)*
0.474	0	11
0.805	10	5
1.217	22	1
1.467	26	0

Table 5.2: Percentages of the main and CT signals detected increasing threshold values for MaPMT biased at 900 V

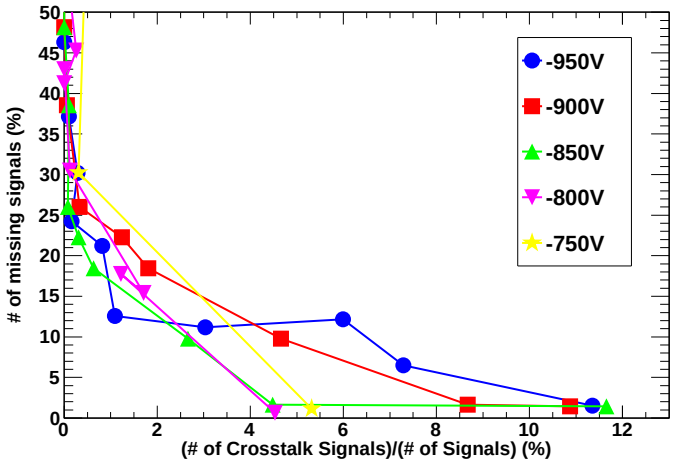

Figure 5.15: Percentage of missing signals is shown as a function of the maximum percentage of Cross–talk signals obtained modifying the trigger threshold

CHAPTER 6

THE PROTON–PROTON COLLISIONS AT LHCb AND COMPARISON OF DATA WITH MONTECARLO EXPECTATIONS

Collisions at LHC have started on the 23 November 2009 and a lot of data are available for the first analysis.
Seventeen years is the time spent from the expression of intent (1992) to the end of the construction to have an operational LHC. LHCb, after 11 years (1998) of construction and after a long commissioning period, is taking data. In this first year of running the proton–proton collisions were at $\sqrt{s} = 7$ TeV.
In this chapter a brief description of the 2010 data collected at LHCb and a first comparison with Monte–Carlo simulation is given. The importance of this kind of analysis is to understand background for the CP and rare decays studies and for the tuning of Monte–Carlo generators at the LHC energies.

6.1 First physics at LHCb

The Large Hadron Collider at CERN has provided its first collisions. It started operations on the 23 November 2009 and LHCb detected its first event at $\sqrt{s} = 0.9$ TeV. The following step was the first world's record energy of $\sqrt{s} = 2.36$ TeV of the 14 December 2009. The 2010 restart was not less successful with the $\sqrt{s} = 7$ TeV reached the 30 March 2010.
Another important and not trivial step was to increase the number of bunches per fill needed to reach higher luminosities. At the end of the 2010 LHCb has recorded an integrated luminosity of $\mathcal{L} \sim 38\ pb^{-1}$, as shown in Fig. 6.1.
After one year from the start up although the nominal designed energy was not yet achieved, LHC has fulfilled several and important milestones. The year was mainly dedicated to the machine commissioning but it was possible to collect data at energies never available before. Thanks to the relatively high statistics recorded, several interesting studies can be done. One is the comparison with theoretical predictions at $\sqrt{s} = 7$ TeV necessary to tune

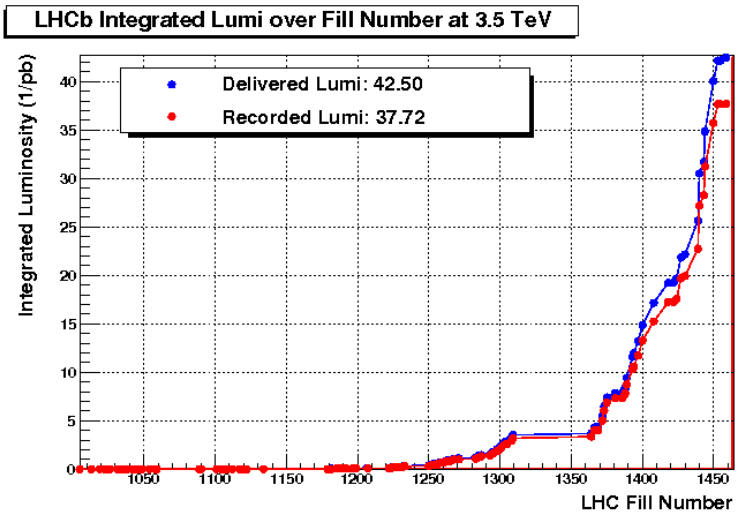

Figure 6.1: The integrated luminosity delivered by LHC in blue, and recorded by LHCb in red, for the 2010 data at 7 TeV

all the Monte Carlo generators.
In Fig. 6.2 the cross sections of various physical processes as a function of the energy in the center of mass $\sqrt{s}$ for the proton–proton collision is shown.
The total inelastic cross section is of the order of $\sim$ 100 mb at $\sqrt{s} = 14$ TeV and it is dominated by soft emissions with low momentum transferred. These events are the so–called Minimum Bias (MB) events.
From the total cross section value (100 mb), the inclusive ($\sigma_{b\bar{b}}$) production is down by a factor 2, and further down there are processes where the $W^{\pm}$ and Z^0 are produced in the few–nb range. The electroweak symmetry breaking Higgs boson production is of the order of 1–100 fb. To be able to study these rare processes a large statistics is needed and the integrated luminosity collected this year is not enough yet.
Details about LHCb data acquisition conditions will be described in the following sections.
In the MB sample there are also hard scattering events with a large momentum transfer, but the rate of these events is small due to their lower production cross sections.
To maximize the collection of such events with a large momentum transfer, specific triggers are implemented to reject the majority of MB events. During the first days of data taking, the luminosity was very low and all the interactions were essentially triggered.
The analysis of minimum bias events is important, especially in this first phase of the experiment. It is necessary to measure the multiplicity, the momentum distribution of the particles, in order to tune the Monte Carlo predictions for future studies; first results for ALICE, ATLAS and CMS are already available in [135–137].
At LHCb several analysis are under study, with the statistics available, based on the minimum bias data sample. First results have been obtained for the production of neutral strange particles, different types of hadrons [138–141] and $b\bar{b}$ cross section [142]. The strange hadron production offers a very good test for phenomenological models of pp interactions. In particular, being the strange quark mass at the level of Λ_{QCD}, it probes the non perturbative QCD regime or soft hadronic interactions. Moreover, as the valence quarks in the

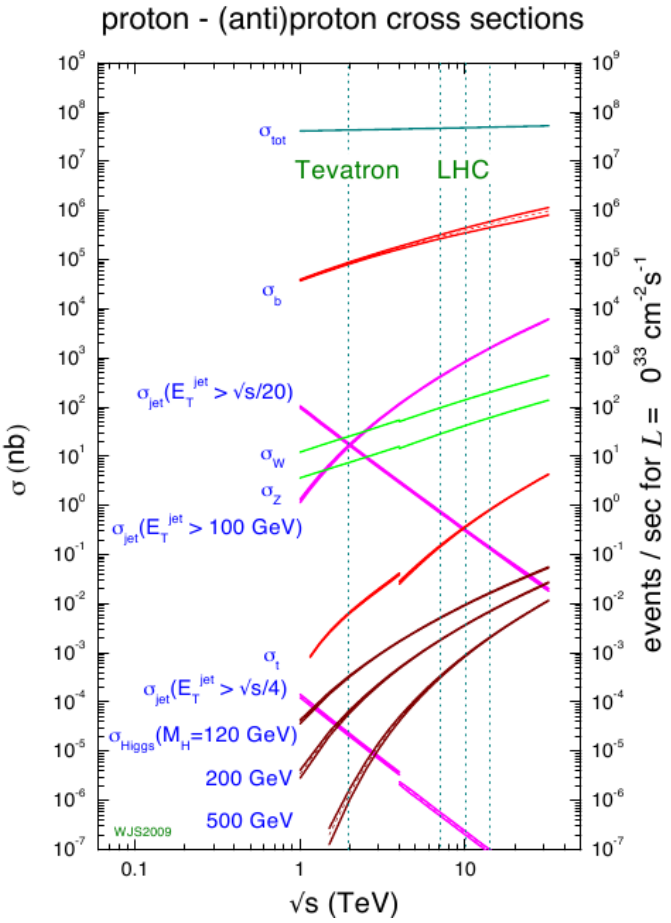

Figure 6.2: Production cross sections as a function of the energy in the center of mass

proton are up and down only, the study of strangeness production provides a good environment to tune phenomenological models of hadronization. For the K^0_S analysis the first results are in good agreement with previous results from other experiments [143–145].
The measurement of the cross section of b hadron production has been compared with predictions at higher orders (NLO) and also in that case values are in agreement with predictions.

6.2 The hadron–hadron interaction kinematics

LHCb was designed with a specific aim, it is not a general purpose detector. For this reason it is a single arm spectrometer covering a region ($\eta \approx 2$–5) complementary to the one of general particle detector.
Proton-proton interactions are composed by diffractive and non–diffractive processes that predominantly involve low momenta transfers. These processes are not described within perturbative QCD but only by phenomenological models implemented in Monte Carlo (MC) event generators.
In Fig. 6.3 Feynman diagram describing the inelastic hadron–hadron scattering is sketched.

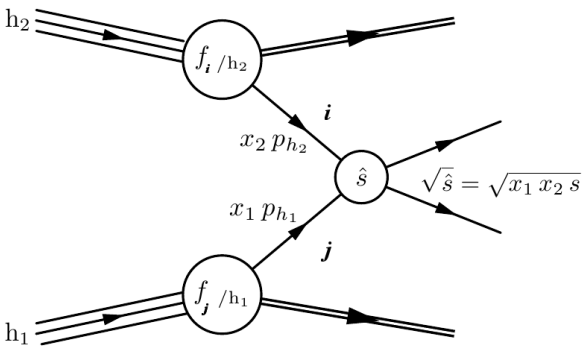

Figure 6.3: Feynman diagram of an inelastic hadron–hadron scattering

The inclusive cross section for hard production processes can be determined using the QCD parton model:

$$\sigma_{h_1h_2}(p_1p_2) = \sum_{ij} \int dx_1 dx_2 f_i^{h1}(x_1,\mu) f_j^{h2}(x_2,\mu) \widehat{\sigma}_{ij}(\mu,\mu')(x_1p_1,x_2,p_2) \tag{6.1}$$

i, j are the two interacting partons, quarks or gluons, with i and j running over all the partons. They carry a fraction $x_{1,2}$ of the incoming hadron's momenta $p_{1,2}$, interact at a momentum transfer scale of $\widehat{s} = x_1x_2s$, where s is the squared center-of-mass energy of the incoming hadrons $f_i^H(x,\mu)$ is the parton density function of the hadron, representing the probability to find the constituent i inside the hadron h. It carries a fraction x of the hadron momentum at the process scale μ and $\widehat{\sigma}_{ij}$ is the cross section calculated in perturbation theory evaluated at a scale μ' of the order of the process scale itself. This function is the main source of error in any theoretical description and it can be fine–tuned only with real data.
In the case of a heavy particles and resonances of mass M produced in the interaction of the 2 partons, the energy needed is $\widehat{s}$=M^2. The energy and longitudinal momentum of the new states produced, not considering the parton masses, are given by:

$$E = (x_1 + x_2)\frac{\sqrt{s}}{2} \qquad\qquad p_L = (x_1 - x_2)\frac{\sqrt{s}}{2} \tag{6.2}$$

Considering the definition of rapidity:

$$y = \frac{1}{2} ln\left[\frac{(E + p_L)}{(E - p_L)}\right] \tag{6.3}$$

and the pseudorapidity as:

$$\eta = \frac{1}{2} ln\left(\frac{|\overrightarrow{p}| + p_L}{|\overrightarrow{p}| - p_L}\right) = -ln\left(\frac{\theta}{2}\right) \tag{6.4}$$

for massless particle η is equal to rapidity y. θ is the angle of $|\overrightarrow{p}|$ with respect to p_L.
Substituting E and p_L into the Eq. 6.2:

$$x_{1,2} = \frac{M}{\sqrt{s}} e^{\pm y} \tag{6.5}$$

which describes the relation between the momentum of the partons and the related rapidities. This can be seen in Fig. 6.4. The plot shows in blue the accessible zone at the LHC energy of 14 TeV.

Considering the Eq. 6.5, if the mass M of the particle generated is very large and com-

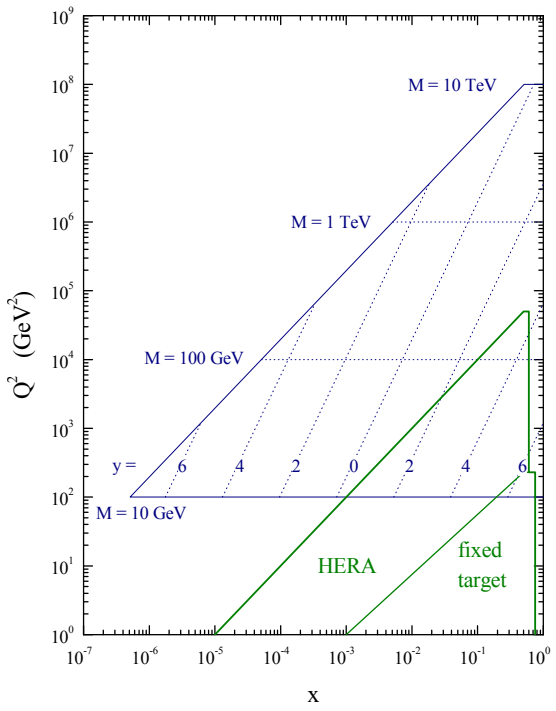

Figure 6.4: The LHC kinematic plane [146] in blue, with $\sqrt{s} = 14$ TeV at scale $Q = M$. In green the coverage at HERA and at fix target experiments

parable with the energy in the center of mass, e^y approaches to 1. The heavy particle is created at central rapidities ($y \to 0$). On the other hand if the momenta of the two partons are very different, the produced particle has a strong boost and it will appear in a region with large rapidity value. The $b\bar{b}$ quarks production at LHCb is shown in Fig. 6.5. The b quarks are preferentially produced at small polar angles and in a narrow cone i.e. either in the forward or backward with respect to the z direction. Fig. 6.6 shows the region covered by the three experiments at LHC. LHCb is designed to cover the zone where the B meson production has the higher probability. The fact that b and $\bar{b}$ have the same direction is the main reason of the LHCb design, covering $1.9 < \eta < 4.9$. Although LHCb covers only the $\sim 2.5\%$ of the solid angle compared to the $> 95\%$ for ATLAS and CMS, the total visible cross section is larger in LHCb ($\sigma(b\bar{b})_{Visible_{LHCb}} = 230\ \mu$b) than for the two other experiments ($\sigma(b\bar{b})_{Visible_{CMS/ATLAS}} = 100\ \mu$b) [147].

The LHCb acceptance is not only suitable to study B meson decays but, giving access to a pseudorapidity region not covered by other LHC experiments (limited to $|\eta| < 2.5$) it allows the investigation in the unexplored forward region.

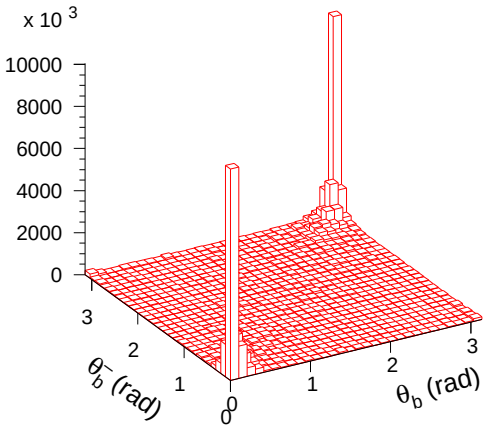

Figure 6.5: Polar angle distribution at LHCb of $b\bar{b}$ hadron production by proton–proton interactions ($\sqrt{s} = 14$ TeV) obtained by Pythia [148] event generator. In evidence the two narrow peaks in opposite directions

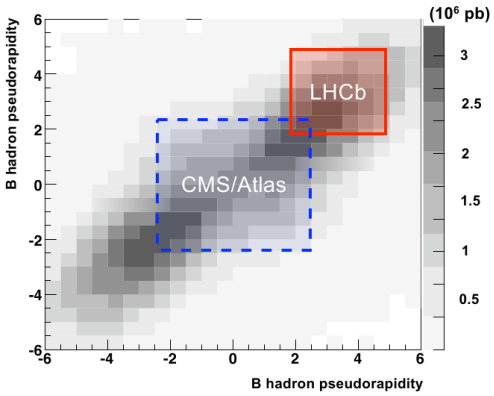

Figure 6.6: The pseudorapidity correlation of $b\bar{b}$ hadron production for the B mesons at the LHC. The regions accessible at LHCb and the general purpose detectors, ATLAS and CMS, are highlighted.

6.3 First collisions at LHCb

During the pilot run of the 2009 and first fills of the 2010, beams had low intensities at $\sqrt{s} = 0.9$ TeV which is the LHC injection energy. Due to the LHCb dipole magnetic field, beams have a crossing angle that results in the center of mass frame moving with velocity 0.0021c in the $-x$ direction. In Fig. 6.7 the top part is the xz plane where is clearly visible the angle between the two beam directions. In the bottom plot (yz plane) the beam direction are aligned. These plots are obtained with 2009 data.

In the first period of collisions, LHC was in the commissioning phase and all the parameters had to be tuned and optimized. One example is the crossing angle which was larger than the nominal one. In order not to risk the safety of the VELO, data were recorded with the two VELO halves positioned 15 mm away (VELO partially open) from their nominal data taking position, resulting in a reduced azimuthal angle coverage.

Another parameter that changed during the machine commissioning was the number of the colliding bunches in the fill. LHC started with a configuration of four bunches per beam, only 2 were colliding in LHCb and spaced by more than 8 μs and a total peak beam intensity of about 1.8×10^{10} protons per bunch. During the last fill at of the end of October 2010, the number of bunches of the two beam were 368 and 344, with an instantaneous luminosity of 1.37×10^{32} and a rate of 3.2 MHz equal to 300 ns spacing between bunches.

The trigger strategy was deployed to provide high efficiency for pp inelastic interactions and for beam collisions with the residual gas in the vacuum chamber. These kind of events (called beam–gas events), happened when only one of the two protons beams interacts with the residual gas. Events were collected for three bunch–crossing types: two colliding

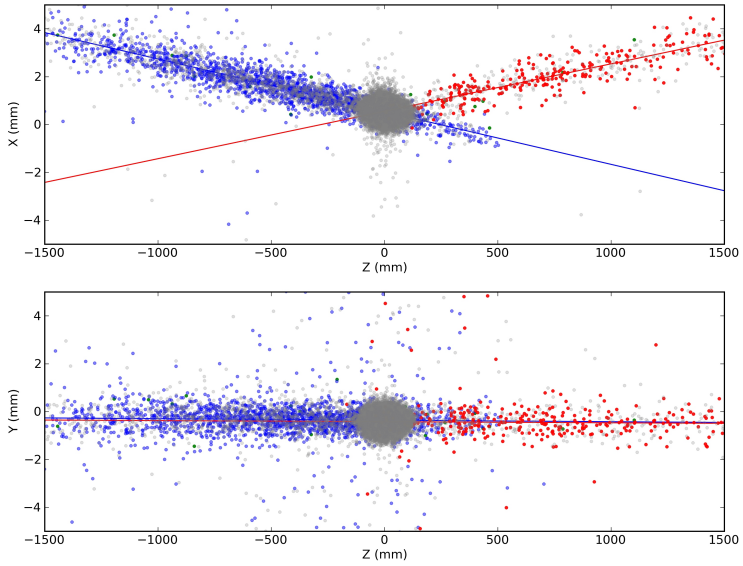

Figure 6.7: Reconstruction of the beam directions in the planes used for the vertex reconstruction. The top plot shows the *xz* plane and the crossing angle is clearly visible. Bottom plot: reconstruction of the beam directions in the *yz* plane

bunches (bb), beam 1 bunch with no beam 2 bunch (b1), and beam 2 bunch with no beam 1 bunch (b2). Measured rates were 10 Hz for the single bunch pair and 0.015 Hz for the b1 and b2 events.
Another important parameter is the number of pp collisions per bunch crossing (ν). LHCb was designed to have $\nu = 1$ at the interaction point. The detectable value is the average number of visible pp interactions per bunch crossing (μ) detected by the experiment. In the earlier runs this value was less than 1 but, during the year, the increase of the number of protons per bunch also increase the probability to have more than one visible pp collision in the event. In fall 2010 μ typically was about 2. The main parameters are listed in Tab. 6.1 and one example of events with high multiplicity is given in Fig. 6.10.
When μ assumes a value larger than 1, then the pile–up effect appears. Pile–up represents

	N.of bunches	**Rate**	**Energy/beam**	μ	L_{Int}
2009	4 (2 colliding)	few Hz	450 GeV	< 1	6.8 μb^{-1}
end of 2010	368 (344 colliding)	3.4 MHz	3.5 TeV	> 2	35 pb^{-1}

Table 6.1: Comparison of the first and last collision runs of LHCb for the 2009/2010. The big effort done to pass from the 2009 values to the values of the last run was very successful

the existence of two or more interaction per bunch–crossing. When this happens the two or more vertices should be detected and reconstructed. The effect of the pile–up is under detailed study because LHCb was designed and optimized for a single interaction per bunch crossing.

The trigger also evolved with the increase of the luminosity and of the beam conditions. During the first runs the threshold values were very loose to detect most of the interactions. This setting is called Minimum Bias (MB) trigger, but the amount of data to be stored increases and only hard events with higher momentum must be considered. Nowadays the collection of MB events is "prescaled". It consists of detecting a random event and the detection frequency is given by the prescaled factor.

6.4 Minimum Bias and Underlying events

The Large Hadron Collider (LHC) is going to open a new kinematic regime in high energy proton–proton collisions, to search for new physics.
The hard scattering in production processes, governed by the strong interactions is calculated by perturbative QCD (pQCD). However for non perturbative effects often only a phenomenological approach is possible. The solution was to extrapolate at this energy range variables measured at low $\sqrt{s}$ and now they must be tuned.
The description of the proton–proton interactions is very complex. It includes hard scattering, as described by pQCD, parton distribution functions inside the proton, underlying event, multiple parton interactions, and jets.
Looking at the total cross–section (σ_{Tot}) for hadron–hadron collisions in Fig. 6.2, it is mainly made up of events with low P_T hadrons (minimum bias events). The most important processes can be divided into elastic (σ_{elas}) and inelastic processes.
The latter one can also be divided in sub–processes, the main ones are: single–diffractive (σ_{sd}), double–diffractive (σ_{db}) and non–diffractive inelastic (σ_{nd}).
All these processes are shown in Fig. 6.8 in the $\eta\phi$ plane, where ϕ is the azimuthal angle and η the pseudorapidity. These events can be classified according to the distribution of the produced particles in the available pseudorapidity region. Most of the total cross section is composed by events with no well defined gaps, the non–diffractive processes. A pseudorapidity gap $\Delta\eta$, an example is shown in the third plot of Fig. 6.8, is the separations between the systems traveling in the forward and backward directions.
The total cross section can be written as:

$$\sigma_{Tot} = \sigma_{elast}(\sqrt{s}) + \sigma_{sd}(\sqrt{s}) + \sigma_{dd}(\sqrt{s}) + \sigma_{nd}(\sqrt{s}) \tag{6.6}$$

where $\sqrt{s}$ is the total center of mass energy.
There are two important "categories":

Minimum Bias (MB): these events are soft partonic events with hadrons with low P_T [150], selected by very loose cuts of the trigger. They are mainly due to double– diffractive and non–diffractive inelastic events, most of them have no gaps in the $\eta\phi$ plane

Underlying Events (UE): they can be defined as what happen in a pp interaction besides the hard scattering process (containing a jet)

In the following analysis the main issue will be the minimum bias sample characterization. An evaluation of the number of charged particles density distribution ($dN_{ch}/d\eta$) as a function of pseudorapidity and the P_T spectrum for minimum bias events at the LHC energy of

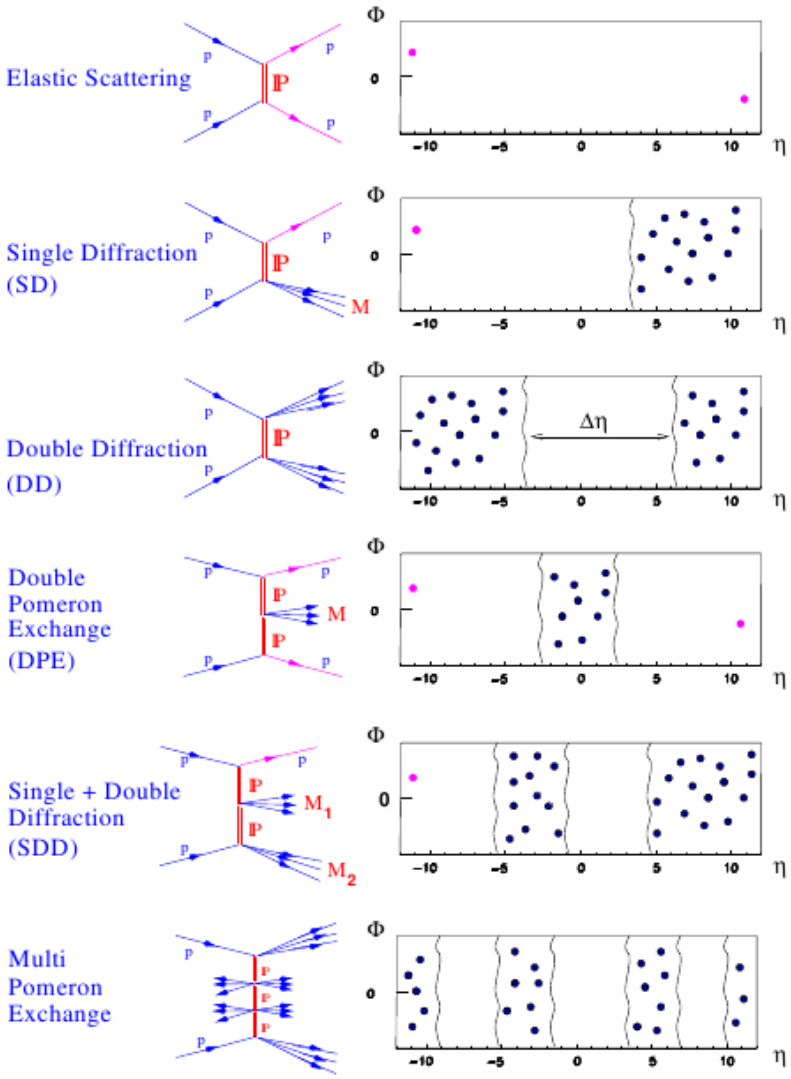

Figure 6.8: Schematic view of elastic and diffractive processes classes in the ηϕ plane[149]. The main contributions is coming from elastic, single and double diffraction processes. Last 3 processes are high order processes with low probability

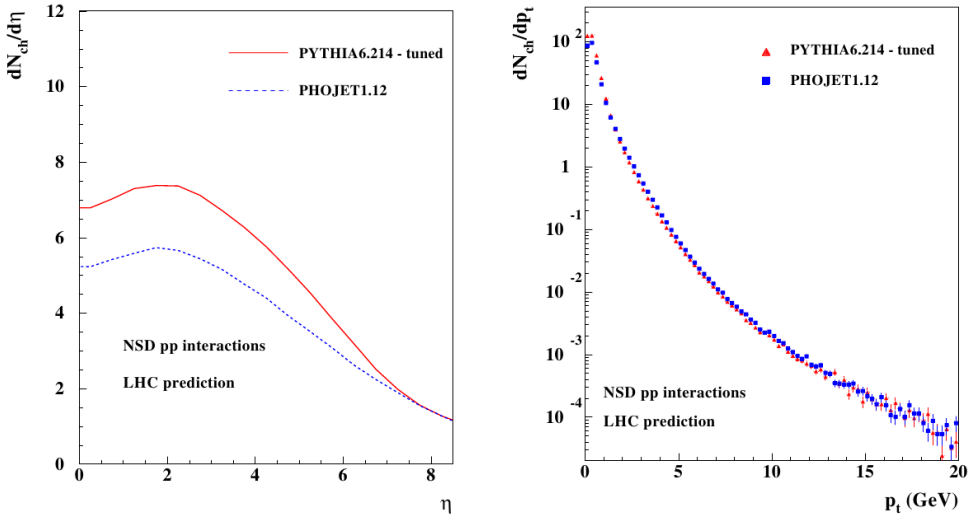

Figure 6.9: Evaluation of minimum bias distributions at the LHC nominal energy of $\sqrt{s} = 14$ TeV with two different MC event generators. Left plot: number of charged particles per unity of pseudo-rapidity. Right plot: P_T distribution [150]

$\sqrt{s} = 14$ TeV, for two MC generators, are in Fig. 6.9. The dip at $\eta = 0$ is only a kinematic effect due to the use of pseudorapidity instead of rapidity, which is flat.

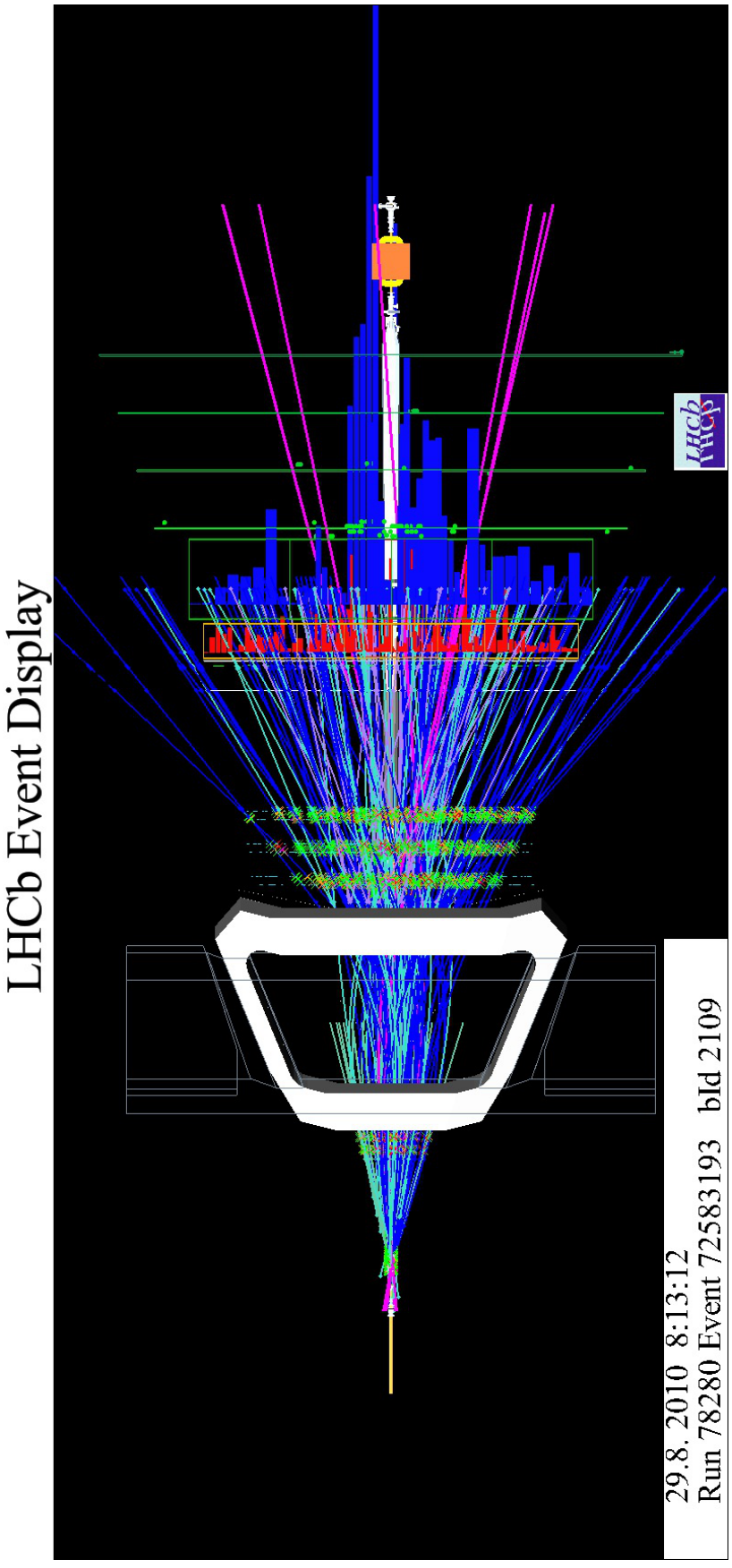

Figure 6.10: Event display of a high multiplicity event detected at LHCb

6.5 Analysis of LHCb minimum bias events

The aim of this analysis is the comparison of the charged particle multiplicity between data and Monte Carlo simulation.
LHCb has the possibility to easily reverse its magnetic field, so that is possible and interesting the comparison of both magnetic field *Up* and *Down* data.
In this section a brief description of the selection criteria applied to events and tracks is given.
The LHCb software used to analyze minimum bias events [1] at 7 TeV is DaVinci [153] v25r4p3. This software provides tools for developing and applying offline selection algorithms to select physics processes of interest.
The analysis is obtained considering only tracks, i.e. charged particles detected by the tracking system, as described in Sect. 2.2. For this analysis only two kind of tracks are considered: *Long* and *Downstream*. This is motivated by the fact that these are the best reconstructed tracks. Both types have hits in the tracking stations, but Longs have hits also in the VELO detector while Downstream tracks do not have VELO hits. They are originated from particles reconstructed outside the vertex locator acceptance (for example K^0_S e Λ).
Several cuts have been applied to select the sample. First of all the selected events [2] have only a single primary vertex (NPV$=1$). There is a cut also on the z axis of the primary vertex ($|\mathrm{PV}_z| < 100$ mm) i.e. z is the beam direction, to have a good primary vertex resolution in z direction. Selection criteria are applied to tracks to select the best tracks passing

Table 6.2: Tab. 6.2(a) lists all the selection criteria applied.Tab. 6.2(b) shows the number of events used for all the sample considered

(a)

Variable	Cut
NPV	1
P_{Min}	3 GeV/c
P_{TMin}	200 MeV/c
$\lvert PV_z\rvert$	100 mm
χ^2	60
χ^2/DOF	3

(b)

Samples	N. Events
$Data\ \overrightarrow{B}Down$	413069
$MC\ \overrightarrow{B}Down$	124552
$Data\ \overrightarrow{B}Up$	149316
$MC\ \overrightarrow{B}Up$	123251

through all the tracking stations. Cuts applied are listed in in Tab. 6.2(a) and yields are listed in Tab. 6.2(b).
During 2010 data taking, the number of collision per bunch crossing increased as described in the previous sections. The "only one collision" per event request is the warranty to have a clean event with the best LHCb operational conditions.

[1] Data: Reco03 [151], Monte Carlo: Sim03 [152]
[2] All the events are *Beam–Beam* events selected by the trigger lines *Lumi* and *Physics* [154]

6.5.1 The track multiplicities

After event and track selections, a study of track multiplicities has been performed. In order to compare with Monte Carlo simulation, identical cuts are applied to MC samples as to data. The study is also performed analyzing magnetic fields Up and Down separately.
In Fig. 6.11 all the plots show the comparison between data (black points) and Monte Carlo (coloured histograms) for the Up field. The plots are normalized to the same area in order to compare the shapes.
The top plots of Fig. 6.11 show separately the two categories, Long and Downstream as

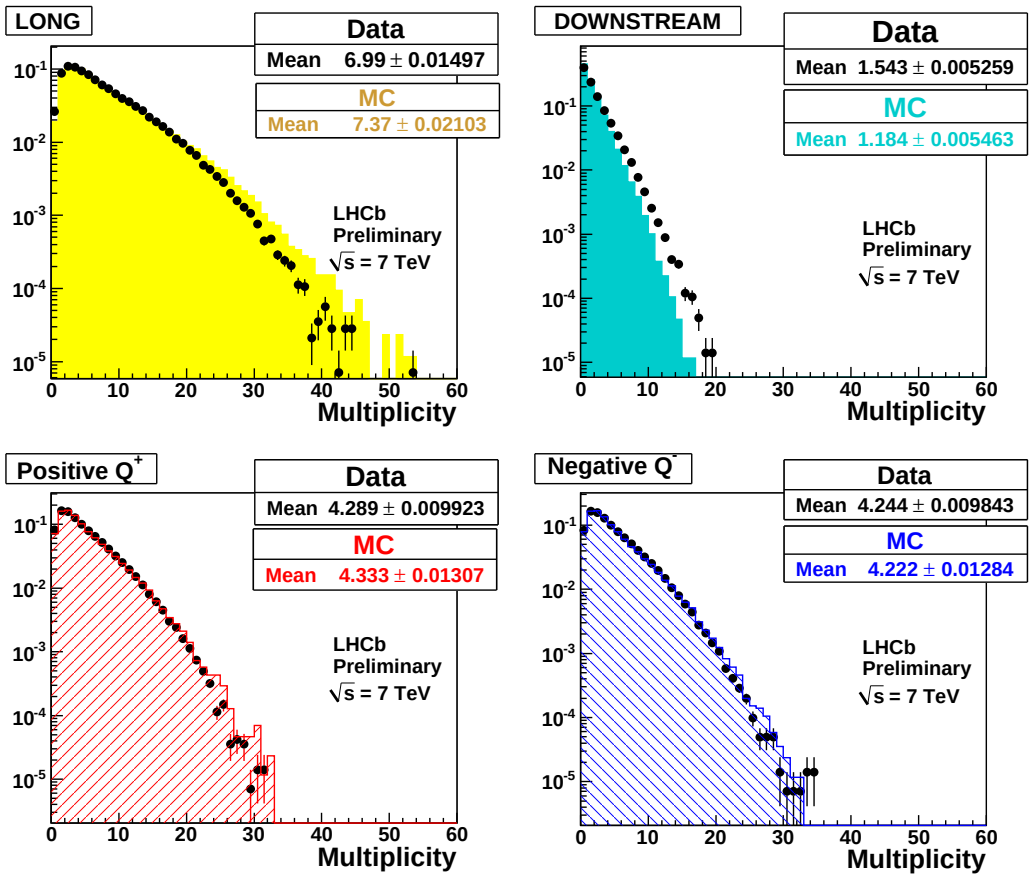

Figure 6.11: Comparison between Data (points) and Monte Carlo (coloured) samples. They are obtained with magnetic field Up. Plots correspond to different track selections as described in the text

defined in Sect. 2.2. The bottom plots show the distribution of positive and negative particles separately. Monte Carlo well describes Long tracks at low multiplicities, but there is a discrepancy at higher, where there is an overestimation of the Monte Carlo sample.
Downstream tracks have another behaviour, Monte Carlo and data are not comparable except for very low multiplicities (< 4 particles/event). To be notice that their contribution to the total is a small amount and corresponds to ~ 1 particle/event.
At the bottom part of the same figure, tracks are selected considering the associated sign of the electrical charge. In this case the comparison simulation–data is better than the previous

case. Only at high values ($>$ 20 tracks/event) a small discrepancy is visible.
In Fig. 6.12 ratios between MC and data are shown for the distributions in Fig. 6.11. If MC

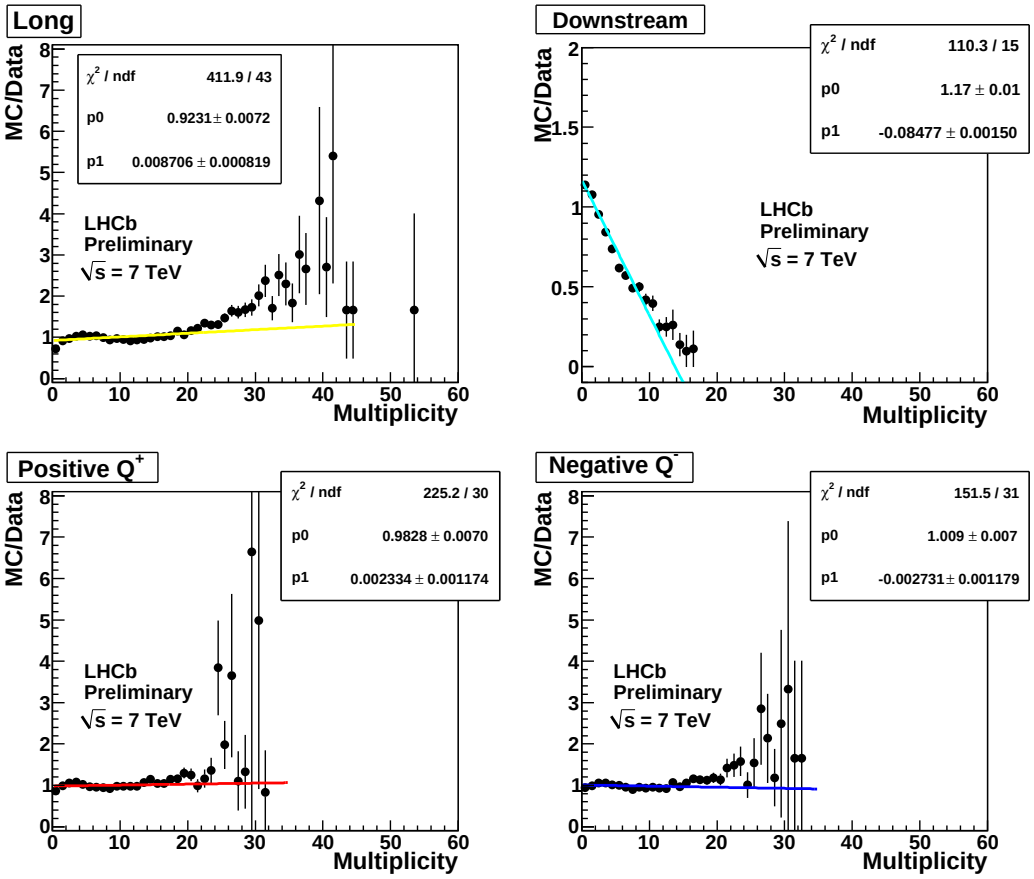

Figure 6.12: Multiplicity ratios between Monte Carlo and data with magnetic field Up

well describe data this ratio should be one. This behaviour is clearly confirmed, except with Downstream tracks. Deviations also displayed only for high multiplicity events when the statistics is small. Compared to the Long, the small fraction of the Downstream tracks and the impact is less relevant.
This analysis is done with the tracking reconstruction and performance available in July 2010.
The percentage composition of the events considered are given in Tab. 6.3. MC values, for both magnetic fields polarities are in agreement for all track types. The same behaviour is also observed comparing the two data samples collected with magnetic fields Up and Down. The track type selection for the same magnetic field, on the contrary, gives different results. In this case data show lower values compared to MC for Long tracks (MC has the $\approx 86\%$ and Data the $\approx 81\%$). Considering Downstream, they have the opposite behaviour. On the other side applying track selection, on the basis of their charge, numbers are comparable.
Another interesting thing to notice is the number of positive charged tracks which is slightly higher than the negatives for all the selected samples.
The same considerations are valid considering Tab. 6.4 where the mean values per event are listed.

	$\overrightarrow{B}Up$		$\overrightarrow{B}Down$	
Type	**N. MC** (%)	**N. Data** (%)	**N. MC** (%)	**N. Data** (%)
Positive	50.65 ± 0.10	50.26 ± 0.08	50.75 ± 0.10	51.09 ± 0.05
Negative	49.35 ± 0.10	49.74 ± 0.08	49.27 ± 0.10	49.91 ± 0.05
Long	86.16 ± 0.15	81.92 ± 0.10	86.0 ± 0.10	81.96 ± 0.06
Downstream	13.84 ± 0.05	18.08 ± 0.04	13.93 ± 0.05	18.04 ± 0.02

Table 6.3: Percentages of tracks types per event

	$\overrightarrow{B}Up$		$\overrightarrow{B}Down$	
Type	$\langle N.MC \rangle_{/Evt}$	$\langle N.Data \rangle_{/Evt}$	$\langle N.MC \rangle_{/Evt}$	$\langle N.Data \rangle_{/Evt}$
Positive	4.33 ± 0.01	4.29 ± 0.01	4.30 ± 0.01	4.377 ± 0.006
Negative	4.22 ± 0.01	4.24 ± 0.01	4.17 ± 0.01	4.190 ± 0.006
Long	7.37 ± 0.02	6.99 ± 0.01	7.29 ± 0.02	7.02 ± 0.01
Downstream	1.18 ± 0.005	1.542 ± 0.005	1.182 ± 0.005	1.550 ± 0.003

Table 6.4: Particle multiplicities per event. Comparison between Monte–Carlo and data samples for the two magnetic field polarities

6.5.2 The pseudorapidity distribution

In the following section η and ϕ distributions are described.
As defined in Eq. 6.4 pseudorapidity η describes the relation with momentum P and its longitudinal projection P_L. It can be also interpreted as the particle angular distribution along the beam direction.
The LHCb spectrometer geometry covers the pseudorapidity region between $1.9 < \eta < 4.9$. Fig. 6.13 shows the plots of η distribution in several different momentum ranges. The chosen ranges are five: $3GeV/c < P \leq 5GeV/c$, $5GeV/c < P \leq 7GeV/c$, $7GeV/c < P \leq 10GeV/c$, $10GeV/c < P \leq 20GeV/c$ and $P > 20GeV/c$. They will be used for the following analysis.
On the top part Long and, on the bottom, Downstream samples are shown from data collected with magnetic field Down. Considering the η shapes for different intervals it is possible to notice the correlation between η and θ. Tracks with momentum smaller than 7 GeV/c are emitted at larger θ value, far from the beam axis. Increasing momentum the accessible kinematic region increases and higher η values are reached. The behaviour described is valid for both Long and Downstream tracks considered, as displayed in the two plot series of Fig. 6.13.
Looking to the acceptance with P larger than 10 GeV/c there is an evident drop at $\eta \approx 4.3$. This is a feature due to the geometry of the detector. That drop is due to a separation zone between two detector parts (inner and outer trackers of the tracking stations).

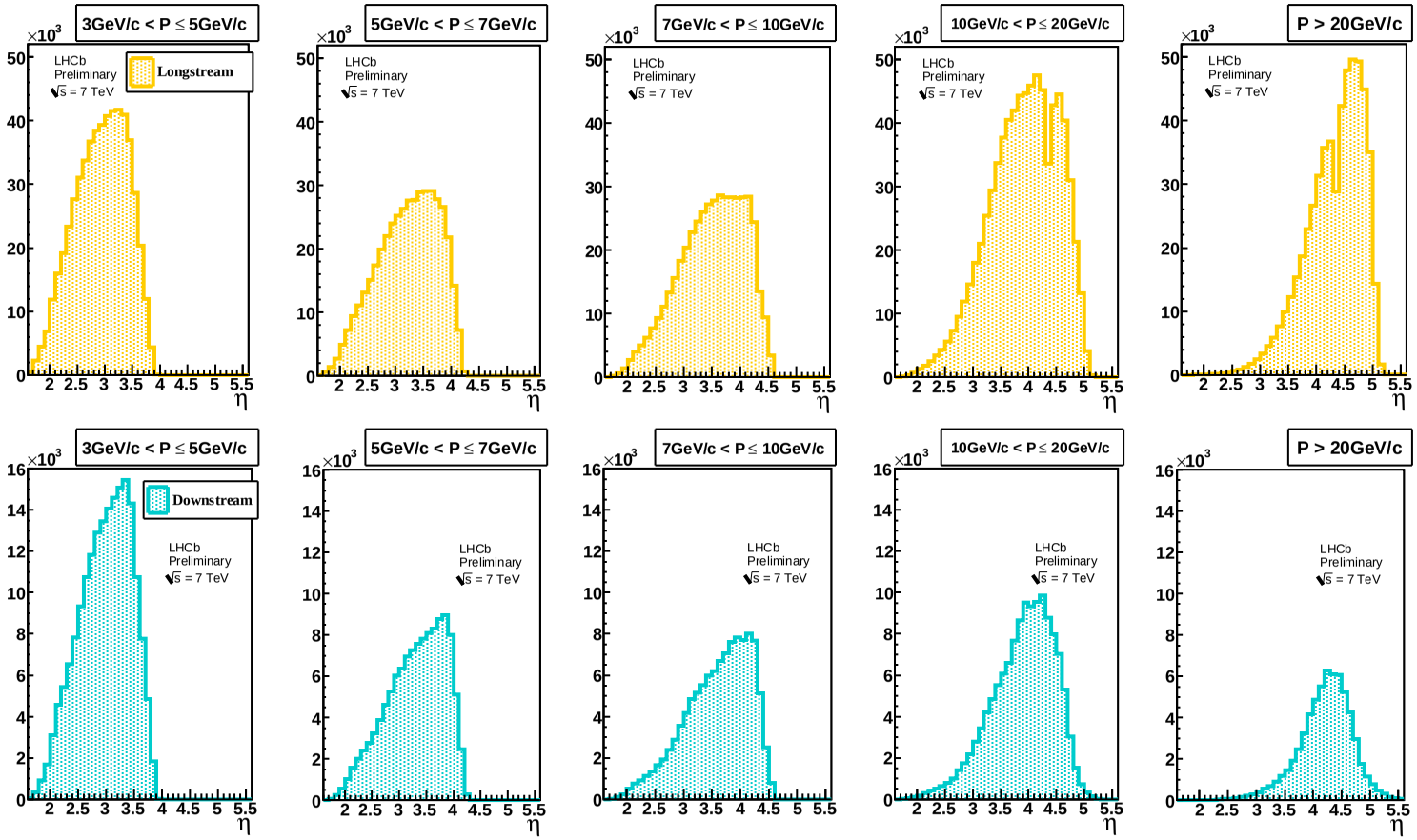

Figure 6.13: Pseudorapidity η distributions divided into few momentum ranges. The upper plots show Long track distributions. On the bottom plots Downstream tracks are shown. Data correspond to events collected with magnet polarity Down

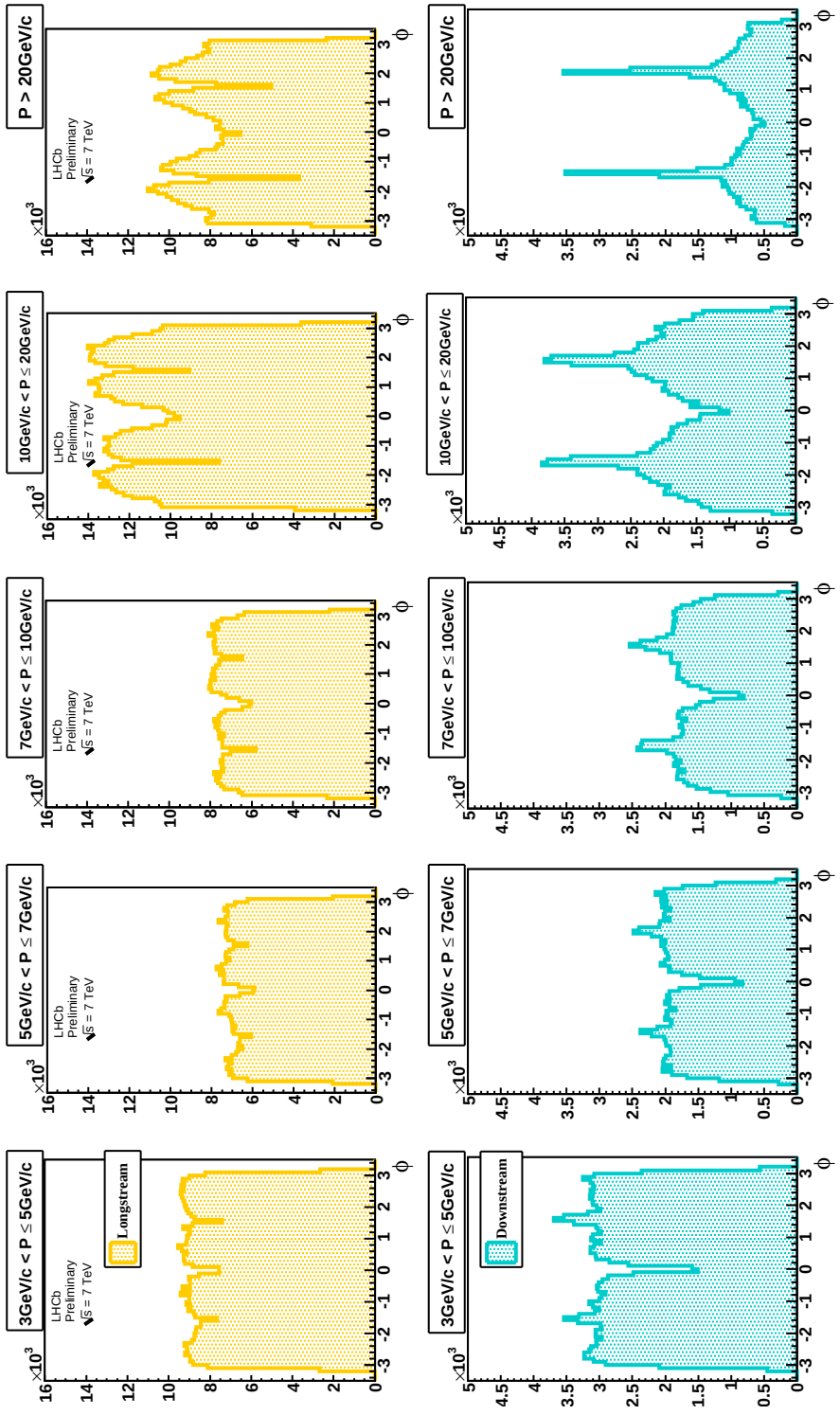

Figure 6.14: Angular distribution ϕ distributions divided into momentum ranges. The upper plots show Long track distributions. On the bottom plots Downstream tracks are shown. Data correspond to events collected with magnet polarity Down

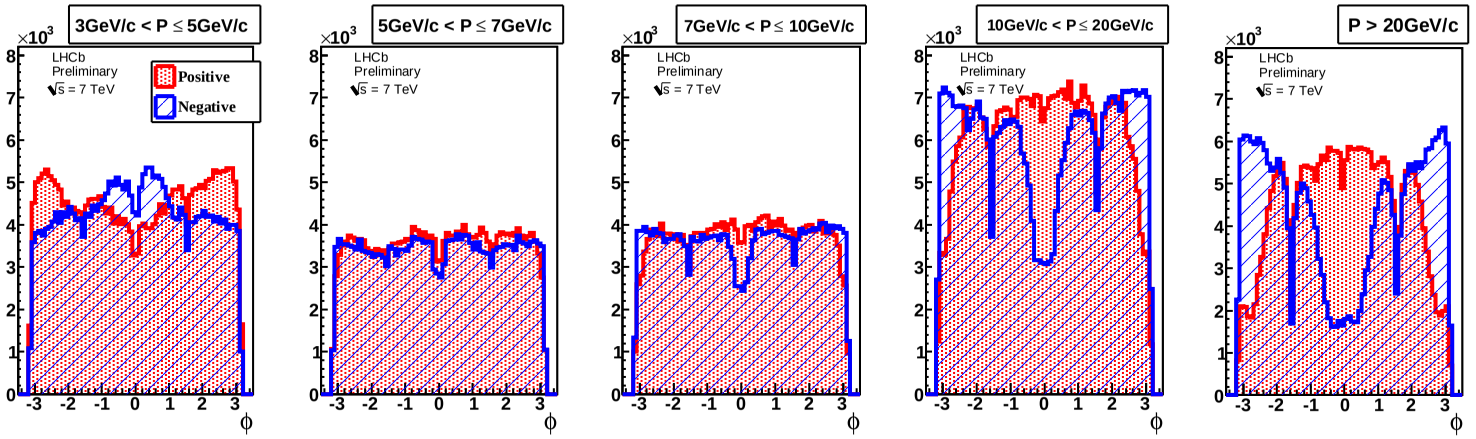

Figure 6.15: Angular ϕ distribution for magnetic field Down obtained with data

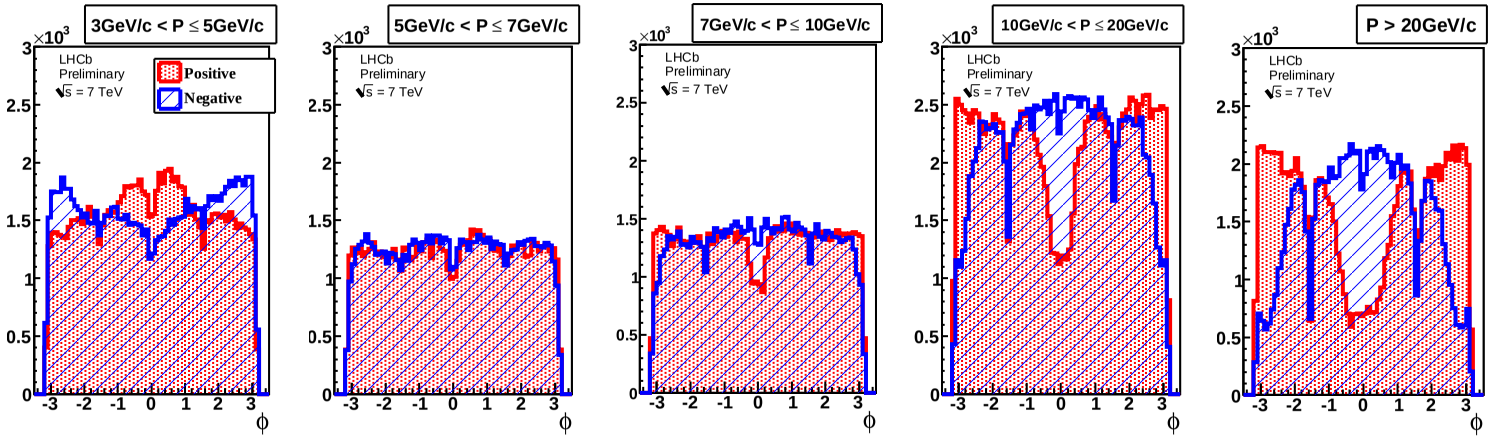

Figure 6.16: ϕ distribution for magnetic field Up obtain with data

6.5.3 The angular distribution ϕ

Another interesting distribution is the ϕ distribution which is the angle in the plane xy, perpendicular to the beam direction. The angle ϕ is defined equal to zero and $\pm\pi$ for $y = 0$ and $\phi = \pm\pi/2$ for $x = 0$, laying in the vertical plane.
In Fig. 6.14 ϕ plots for both track types Long and Downstream are shown.
As for the η distribution, also the ϕ angular distribution is evaluated for several momentum ranges. The division in sub–ranges was done to control any possible variation related to kinematics.
Without considering different statistic values of different intervals, distributions for P lower than 10 GeV/c can be considered equally distributed over all ϕ, except for two small ranges about $\phi \approx 0$ and $\phi \approx \pm\pi/2$. The same behaviour is displayed for both samples.
These two empty zones are related to a detector effect. The LHCb layout has two movable parts (A and C sides) and in closed position the dead zones are at $\phi \approx \pm\pi/2$. The $\phi \approx 0$ dip could be induced by the different reconstruction for different tracks.
The angular ϕ distribution for Long tracks different magnetic field polarities (in Fig. 6.15 Down and Fig. 6.16 Up) and divided for positive and negative are shown.
Thus allows to search for possible differences in the angular distributions that could be due to an asymmetric detection.
Moreover the study considering tracks selected by their associated by electrical charge is very useful. Considering different interactions which occur in the detector material. Select positive, negative, soft and hard tracks is useful because they interact differently in the material. These differences can be used to study the detector response.
The reversed magnet polarity is the best way to appreciate any possible deviation of the angular distributions induced by these effects. The two series of plot, in Fig. 6.15 and Fig. 6.16, display the same data sample of Long tracks. Plots with momentum in the range between 5 GeV/c and 10 GeV/c, show compatible and uniform distributions. In the central zones ($\phi \approx 0$) some differences between positive and negative tracks can be easily seen. For example, considering the plot with momentum between 7 GeV/c and 10 GeV/c in Fig. 6.15 there are more negative tracks on the two lateral edges ($|\phi| \approx \pi$). Therefore positive tracks are centrally displayed at about $\phi \approx 0$. The opposite feature is observed, in the same momentum range, in Fig. 6.16 obtained with opposite polarities of the magnetic field.
Referring to plots at very low or very high momenta, this behaviour is much more visible. This can be explained in terms of magnetic field effect. In fact it acts on charged particles bending them in the opposite direction according to their electric charge.

6.6 The charge asymmetry

In a proton–proton collision, the interacting partons generate new particles. Considering the LHC colliding protons, both of them are positive charged, should result in a small forward positive charge in the final state.
In the LHCb detector it is possible to invert the polarity of the dipole magnet to reduce systematics and study the detector behaviour. All systematics due to any asymmetry in the detector acceptance and/or efficiency should be negligible comparing data taken with opposite polarity of the magnetic field.

6.6.1 The charge asymmetry ratio R_0

Several methods can be used to determine a possible production charge asymmetry.
First of all it is important to evaluate the detector uniformity.
The ratio between the number of positive (Q^+) and negative (Q^-) tracks can provide some informations. This ratio is calculated as a function of η and ϕ and divided into several momentum ranges already described in the previous sections.
Two examples are reported in Fig. 6.17. They have been obtained, for the same momentum range, considering the two magnetic field polarities. The opposite track behaviour bent by

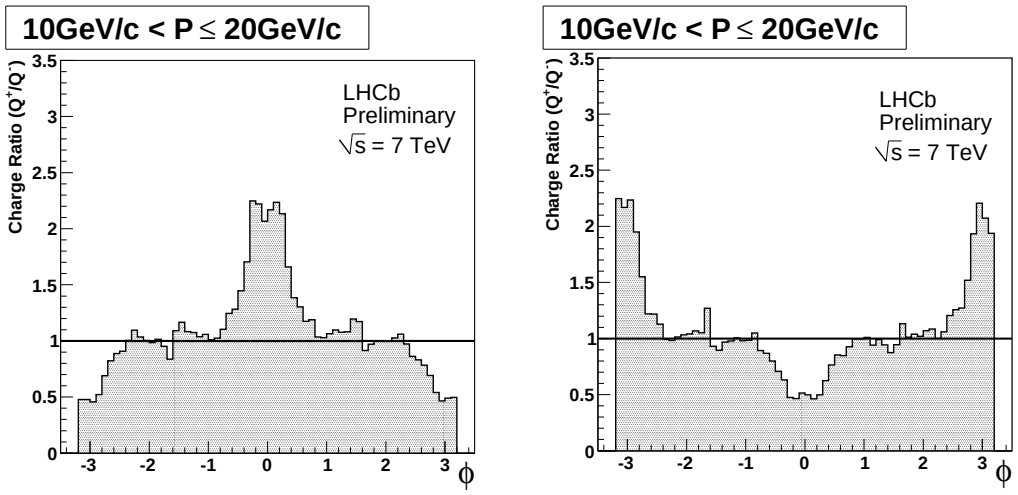

Figure 6.17: Q^+/Q^- ratio for both magnetic polarities obtained with data. On the left: Down field. On the right: Up field. These ratios are obtained considering plots in Fig. 6.15 and Fig. 6.16 for the momentum range 10–20 GeV/c

the magnetic field, described in the previous section is clearly visible. The line displayed is equal to 1 and it is plotted to guide the eye. It points to a perfect compensation between positive and negative charged tracks. Deviations from the unity indicate the effects of magnetic bending fields for opposite charged particles.
To limit this contribution and check detector uniformity, the simplest way is to consider the ratios of the two magnetic field samples. The new ratio considered is:

$$R_0 = \frac{\left(\frac{Q^+}{Q^-}\right)_{\vec{B}_{Up}}}{\left(\frac{Q^-}{Q^+}\right)_{\vec{B}_{Down}}} \tag{6.7}$$

It is important to remember that the magnet polarity is opposite in the two samples so that tracks behaviour are opposite to each other.
To study the detector uniformity this ratio is calculated for all the momentum ranges shown in Fig. 6.15 as a function of ϕ. Results obtained with data are shown in Fig. 6.18 for the momentum range 10–20 GeV/c. The result of a linear fit is superimposed.
The flatness of this distribution shows the uniformity detector response over the whole ϕ range. This description is true for the graph shown in Fig. 6.18, but it is valid for all the momentum ranges considered. All distributions are completely flat and all the fit parameters

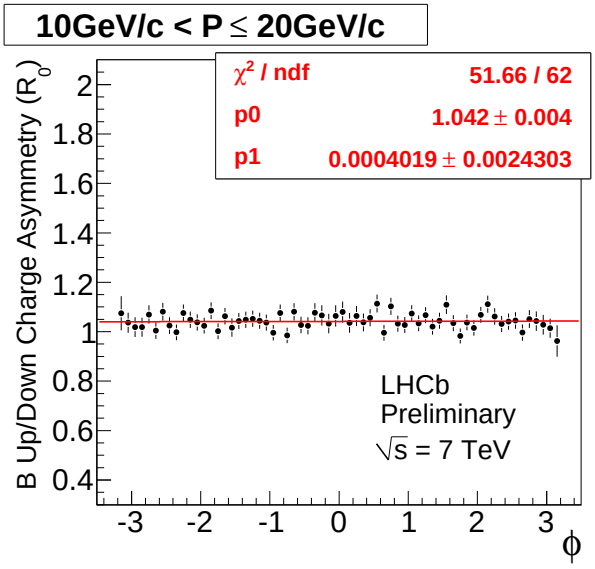

Figure 6.18: Example of the ratio R_0 plot as a function of ϕ. it is obtained for the momentum range 10–20 GeV/c obtained with data

obtained are shown in Fig. 6.19. On the right, graph shows the angular coefficient $p1$ of the linear fit. All the values can be fit with a linear function compatible with zero. In the left plot $p0$ parameters are displayed. All of them have values well above one, as described for the single case of Fig. 6.18.
Results of the ϕ distribution analysis show that MC and data are in good agreement.
The two fit parameters, for all the samples, have been plotted in Fig. 6.19. The final fit values are reported in Tab. 6.5.
A different approach is used as a function of η. In this case the distributions considered are integrated over the whole momentum range. This is done to disentangle detector geometric uniformity from the kinematic effect.
All distributions have been fitted using one–order polynomial and the same fit procedure has been applied also to the Monte Carlo samples. The fit range used is $1.9 < \eta < 4.9$, the LHCb pseudorapidity range.
The two obtained distributions are shown in Fig. 6.20 for data (on the left) and MC (on the right). Values of the fit are given in Tab. 6.5.

			Monte–Carlo	**Data**
η		p0	1.147 ± 0.018	1.169 ± 0.012
		p1	-0.025 ± 0.005	-0.031 ± 0.003
ϕ	p0	p0	1.063 ± 0.008	1.067 ± 0.005
		p1	-0.002 ± 0.002	-0.0025 ± 0.0016
	p1	p0	-0.0025 ± 0.0045	0.003 ± 0.003
		p1	0.002 ± 0.001	-0.0006 ± 0.0009

Table 6.5: Fit parameters $p0$ and $p1$ of the R_0 ratio

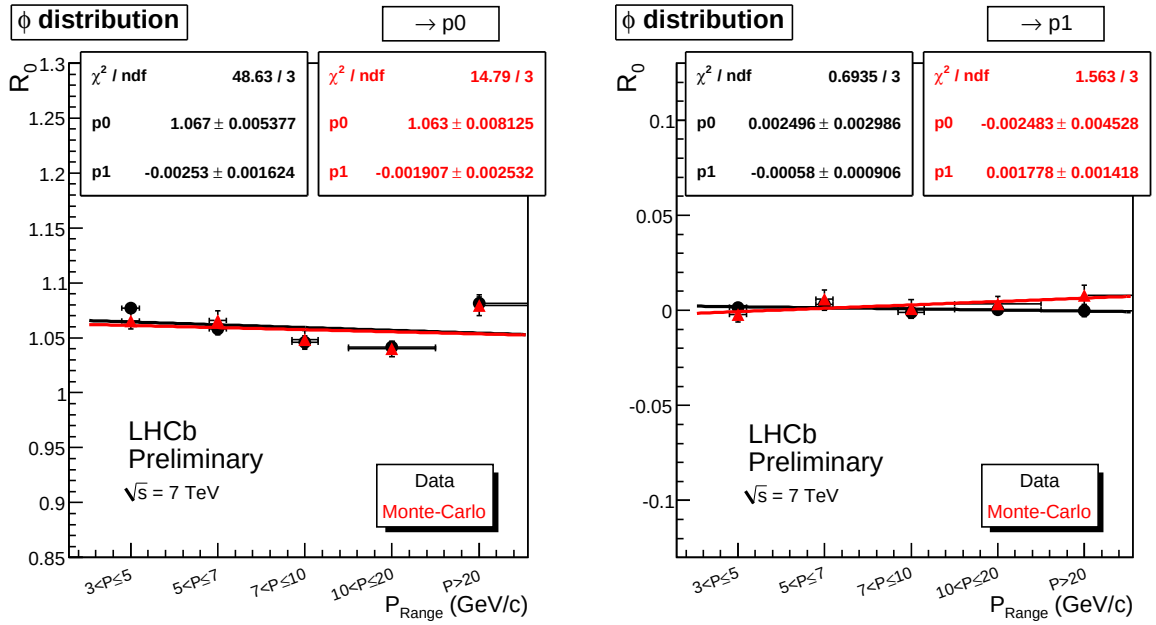

Figure 6.19: Distribution of the results from the R_0 fits, one example is in the plot in Fig. 6.18. Each plot shows the comparison between data (black points) and MC (red points). Values are obtained from R_0 fits of the plots ratios in Fig. 6.17. On the left: plot of $p0$ parameters. On the right: $p1$ fit parameters

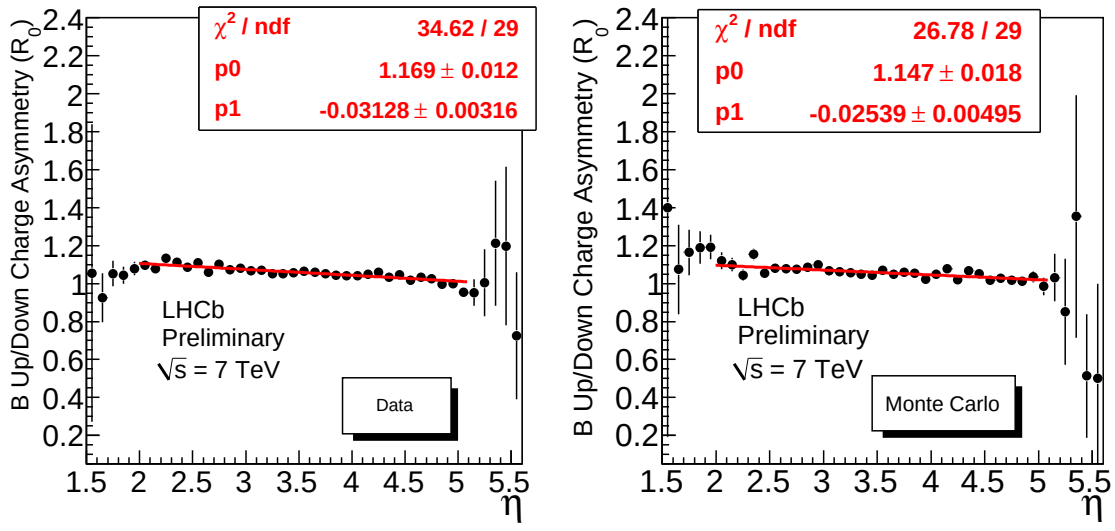

Figure 6.20: Ratio R_0 as a function of η integrated over all momentum range. The two plots are obtained with data (on the left) and with Monte Carlo (on the right)

6.6.2 The charge asymmetry A

A charge asymmetry study has been done considering the asymmetry definition:

$$A = \frac{Q^+ - Q^-}{Q^+ + Q^-} \tag{6.8}$$

where, Q^+ and Q^- are the number of positive or negative tracks.
The asymmetry A is evaluated as a function of the kinematic variables P, P_T and η and all the tracks considered detected in the range $2.2 < \eta < 4.7$, the best tracking resolution region. Also in this case the analysis is performed for data taken with both magnetic fields polarities. Fig. 6.21 and Fig. 6.22 shows the magnet Down and Up data. As the previous case the fit is linear for all the variables. The straight line well represent the behaviour displayed.
All fit results are listed in Tab. 6.6 ($p0$ parameter) and in Tab. 6.7 ($p1$ parameter). The

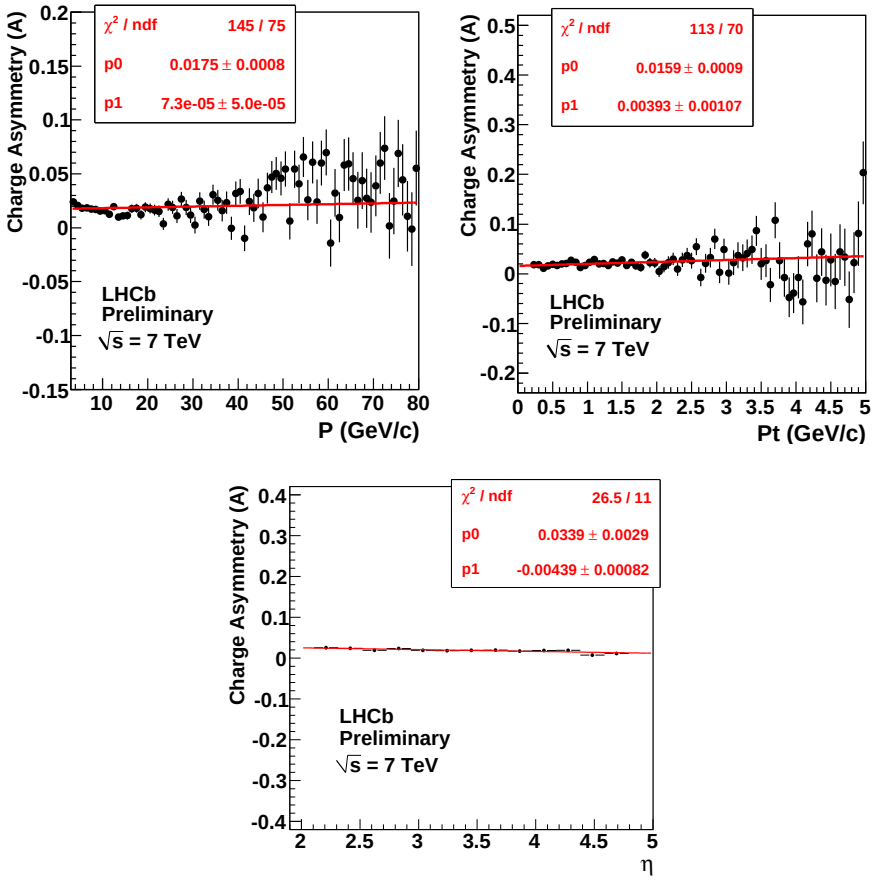

Figure 6.21: Charge asymmetry A as a function of several variables. On the top left plot: momentum. On the top right plot: transverse momentum. On the bottom: η. Data collected with magnetic field Down

second table shows that all $p1$ values are small and about zero. The $p0$ values, which should give an evaluation of the charge asymmetry, are always different from zero.
The asymmetry values calculated with magnetic field Up, are compatible between data and Monte Carlo, except for η where data have a larger value than MC.
Data with magnetic field Down is the largest data sample used in this analysis and it has the smallest statistical error. In this case the values obtained are comparable between data and MC in all the variables.
In the last column of Tab. 6.6 are listed the values of A calculated from Eq. 6.8 for all the

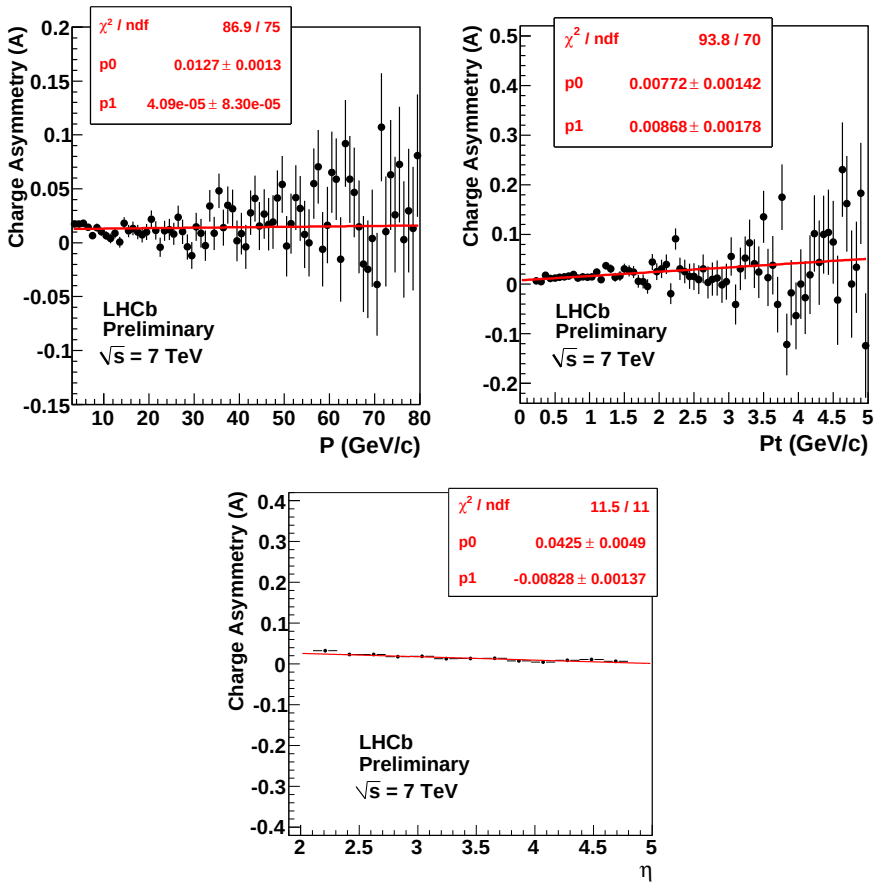

Figure 6.22: Charge asymmetry A as a function of several variables. On the top left plot: momentum. On the top right plot: transverse momentum. On the bottom: η. Data collected with magnetic field Up

events. In this case there is a discrepancy and all the values calculated are slightly different from the expected ones.
Only statistical errors are considered. Systematic errors must be evaluated which could introduce errors able to reduce the discrepancy shown.

		$P(GeV/c)$	$P_T(GeV/c)$	η	$\mathbf{A}_{Int}$
$\overrightarrow{B}_{Up}$	*MC*	0.0092 ± 0.0018	0.0061 ± 0.0020	0.0193 ± 0.0066	0.0125±0.0012
	Data	0.0127 ± 0.0013	0.0077 ± 0.0014	0.0425 ± 0.0049	0.0037 ±0.0010
$\overrightarrow{B}_{Down}$	*MC*	0.0151 ± 0.0018	0.0099 ± 0.0020	0.0397 ± 0.0066	0.0159 ± 0.0012
	Data	0.0175 ± 0.0008	0.0159 ± 0.0008	0.0339 ± 0.0029	0.0249±0.0006

Table 6.6: $p0$ parameter values filled for the samples and variables (P, P_T, η) considered. In the last column the asymmetry A as evaluated from Eq. 6.8 for all events

		$P(GeV/c)$	$P_T(GeV/c)$	η
$\overrightarrow{B}Up$	*MC*	0.0002 ± 0.0001	0.0098 ± 0.0027	-0.0020 ± 0.0018
	Data	0.00004 ± 0.00008	0.0087 ± 0.002	-0.0083 ± 0.0014
$\overrightarrow{B}Down$	*MC*	-0.00001 ± 0.00012	0.0087 ± 0.0027	-0.007 ± 0.002
	Data	0.00007 ± 0.00005	0.0039 ± 0.0011	-0.0044 ± 0.0008

Table 6.7: $p1$ fit parameters of the fits displayed in Fig. 6.21

6.7 Conclusions

This preliminary analysis is obtained with a sample of minimum bias data collected with the best LHCb operational condition. It demonstrates the detector uniformity response for charged particles detection over all the LHCb spatial coverage.
The direct study of the charge asymmetry is already reported. Values obtained show a difference between values obtained with different magnetic fields and between data and Monte Carlo, to be explained.
Both the analysis shown signs in favour of a positive charge asymmetry as expected. All the values obtained are, in fact, positive. All the evaluated errors are statistical only. Systematic errors are also to be considered and implemented in further analysis.

LIST OF FIGURES

LIST OF TABLES

BIBLIOGRAPHY

[1] A. D. Sakharov, *Violation of CP Invariance, c Asymmetry, and Baryon Asymmetry of the Universe*, Pisma Zh. Eksp. Teor. Fiz. **5**, 32 (1967).

[2] A. D. Sakharov, *Violation of CP Symmetry, C–Asymmetry, and Baryon asymmetry of the Universe*, Sov. Phys. JETP Lett. 5 , 24 (1967).

[3] The AMS Collaboration, *Search for Antihelium in Cosmic Rays*, Phys. Lett. B 461 , 387 (1999).

[4] L. R. Evans and P. Bryant, *LHC Machine*, J. Instrum. **3**, S08001. 164 p (2008).

[5] *ALICE Collaboration*, *ALICE: Technical proposal for a Large Ion collider Experiment at the CERN LHC*LHC Tech. Proposal (CERN, Geneva, 1995).

[6] *ALICE Collaboration*, *The ALICE experiment at the CERN LHC*, J. Instrum. **3**, S08002. 259 p (2008).

[7] *ATLAS Collaboration*, *ATLAS: technical proposal for a general-purpose pp experiment at the Large Hadron Collider at CERN*LHC Tech. Proposal (CERN, Geneva, 1994).

[8] The ATLAS collaboration, *Track-based underlying event measurements in pp collisions at sqrts = 900 GeV and 7 TeV with the ATLAS Detector at the LHC*, ATLAS-CONF-2010-081, 2010.

[9] *CMS Collaboration*, *CMS Technical proposal*LHC Tech. Proposal (CERN, Geneva, 1994), Cover title : CMS, the Compact Muon Solenoid : technical proposal.

[10] *CMS Collaboration*, *The CMS experiment at the CERN LHC*, J. Instrum. **3**, S08004 (2008).

[11] W.N. Cottingham, D.A. Greewood, *An Introduction to the standard model of particle physics* (Cambridge University Press, 1991).

[12] P. W. Higgs, *Broken symmetries massless particles and gauge fields*, Phys. Lett. **12**, 132 (1964).

[13] P. W. Higgs, *Broken symmetries and the masses of gauge bosons*, Phys. Rev. Lett. **13**, 508 (1964).

[14] G. Ross, *Grand Unified Theories* (Westview Press, 1984).

[15] C. S. Wu, E. Ambler, R. W. Hayward, D. D. Hoppes, and R. P. Hudson, *Experimental Test of Parity Conservation in Beta Decay*, Phys. Rev. **105**, 1413 (1957).

[16] J.H. Christenson, J.W. Cronin, V.L. Fitch, R. Turlay, *Evidence for the* 2π *Decay of the* K_2^0 *Meson*, Phys. Rev. Lett. **13**, 138.

[17] (BABAR Collaboration), B. e. a. Aubert, *Observation of CP Violation in the* B^0 *Meson System*, Phys. Rev. Lett. **87**, 091801 (2001).

[18] (Belle Collaboration), K. e. a. Abe, Observation of large cp violation in the neutral b meson system, Phys. Rev. Lett. **87**, 091802 (2001).

[19] N. Cabibbo, Unitary symmetry and leptonic decays, Phys. Rev. Lett. **10**, 531 (1963).

[20] M. Kobayashi and T. Maskawa, *CP-Violation in the Renormalizable Theory of Weak Interaction*, Progress of Theoretical Physics **49**, 652 (1973).

[21] L.-L. Chau and W.-Y. Keung, *Comments on the Parametrization of the Kobayashi-Maskawa Matrix*, Phys. Rev. Lett. **53**, 1802 (1984).

[22] L. Wolfenstein, *Parametrization of the Kobayashi-Maskawa Matrix*, Phys. Rev. Lett. **51**, 1945 (1983).

[23] R. Aleksan, B. Kayser, and D. London, Determining the quark mixing matrix from cp-violating asymmetries, Phys. Rev. Lett. **73**, 18 (1994).

[24] *Commutator of the Quark Mass Matrices in the Standard Electroweak Model and a Measure of Maximal CP Nonconservation*.

[25] CKMfitter Group, Charles, J. and others, *CP violation and the CKM matrix: Assessing the impact of the asymmetric B factories*, Eur. Phys. J. **C41**, 1 (2005), hep-ph/0406184.

[26] C. Jarlskog and R. Stora, *Unitarity polygons and CP violation areas and phases in the standard electroweak model*, Physics Letters B **208**, 268 (1988).

[27] K. Nakamura et al., *Particle data Group* .

[28] LHCb Collaboration, *Road map for selected key measurements from LHCb*, CERN-LHCb-PUB-2009-029, 2010.

[29] LHCb Collaboration, *LHCb Trigger System Technical Design Report*, 2003.

[30] E. Aslanides et al., *the level–0 muon trigger for the LHCb experiment*, Nucl. Instrum. Meth. **A 579** (2007).

[31] E. Van Herwijnen, *The LHCb Trigger*, CERN-LHCb-PROC-2010-055.

[32] LHCb Collaboration, *LHCb Magnet*, 2000.

[33] J.André et al., *Status of the LHCb Magnet System*, IEEE Trans. Appl. Superconduct. **12 No.1**, 366 (2002).

[34] J.André et al., *Status of the LHCb Dipole Magnet*, IEEE Trans. Appl. Superconduct. **14**, 509 (2004).

[35] LHCb Collaboration, *LHCb VELO*, 2001.

[36] L. Eklund, *Control and Monitoring of VELO and Pile-Up Level 0 Electronics*, EDMS document https://edms.cern.ch/document/596194.

[37] S. Lochner and M. Schmelling, *The Beetle Reference Manual*, Note LHCb 2005-105.

[38] M. Schmelling, *Specification of the Front-End Electronics for the LHCb Vertex Locator*, Note LHCb 2001-048.

[39] D. Petrie, C. Parkes, S. Viret, *Study of the impact of VELO misalignments on the LHCb tracking and L1 trigger performance*, Note LHCb 2005-056.

[40] W. Baldini et al., *LHCb alignment strategy*, Note LHCb 2006-035.

[41] *A new method for the high–precision alignment of track detectors*, 2002, PHYSTAT2002, Durham.

[42] J. Gassner, F. Lehner and S. Steiner, *The Mechanical Design of the LHCb Silicon Trigger Tracker*, Note LHCb 2004-110.

[43] A. Vollhardt, *A radiation tolerant fiber-optic readout system for the LHCb Silicon Tracker*, Note LHCb 2005-032.

[44] M. Needham, *Silicon Tracker Occupancies and Clustering*, Note LHCb 2007-024.

[45] LHCb Collaboration, *LHCb Trigger System*, 2003.

[46] J. Gassner, M. Needham and O. Steinkamp, *Layout and Expected Performance of the LHCb TT Station*, Note LHCb 2003-140.

[47] LHCb Collaboration, *LHCb Inner Tracker*, 2002.

[48] LHCb Collaboration, *LHCb Outer Tracker*, 2001.

[49] S. Bachmann, *Specifications for the drift gas quality of the outer tracking system*, Note LHCb 2002-031.

[50] S. Bachmann, *Proposal for the gas distribution in the outer tracking system*, Note LHCb 2003-054.

[51] A. Berkien et al., *The LHCb Outer Tracker Front-End Electronics*, Note LHCb Note LHCb 2005-025.

[52] LHCb Collaboration, *LHCb Calorimeter*, 2000.

[53] C. Beigbeder-Beau et al., *A joint proposal for the Level 0 calorimetric triggers*, Note LHCb 1999-017.

[54] R. Djeliadine,O. Iouchtchenko, V. F. Obraztsov, *LHCb hadron trigger and HCAL cell size and length optimisation*, Note LHCb 1999-035.

[55] S. N. Filippov et al., *Design and construction of the LHCb Scintillator-Pad/Preshower Detector*, Note LHCb 2000-042.

[56] E. Guschin, S. V. Laptev, *MonteCarlo study of LHCb preshower*, Note LHCb 2000-030.

[57] Z. Ajaltouni et al., *Study of mutlti anode photomultipliers for the electromagnetic calorimeter preshower read out of the LHCb experiment*, Nucl. Instrum. Meth. **A 504** (2003).

[58] E. Aguilo et al., *Test of muti–anode photomultiplier tubes for the LHCb scitillator pad detector*, Nucl. Instrum. Meth. **A 538** (2005).

[59] E. Graugés et al., *Mass characterization of MaPMT tubes for the LHCb scintillator pad detector*, Nucl. Instrum. Meth. **A 572** (2007).

[60] S. Barsuk et al., *Design and construction of the electromagnetic calorimeter for the LHCb experiment*, Note LHCb 2000-043.

[61] A. Arefiev et al., *Design of PMT base for the LHCb electromagnetic calorimeter*, Note LHCb 2003-150.

[62] A. Arefiev et al., *Design, construction, quality control and performance study with cosmic rays of modules for the LHCb electromagnetic calorimeter*, Note LHCb 2007-148.

[63] R. Dzhelyadin, *The LHCb hadron calorimeter*, Nucl. Instrum. Meth. **A 494** (2002).

[64] LHCb Collaboration, *LHCb Muon System*, 2001.

[65] LHCb Collaboration, *Addendum at the LHCb Muon System*, CH-1211 Geneve 23, Suisse, 2003.

[66] LHCb Collaboration, *Second Addendum at the LHCb Muon System*, CH-1211 Geneve 23, Suisse, 2005.

[67] G. Martellotti, R. Santacesaria and A. Satta, *Particle rates in the LHCb muon detector*, Note LHCb 2005-075.

[68] B. Bochin et al., *Wire pad chamber for LHCb muon system*, Note LHCb 2000-003.

[69] G. Lanfranchi, *time resolution and aging properties of the MWPCs for the LHCb muon system*, Nucl. Instrum. in Phys. Res. **A 535** (2004).

[70] A. Kachtchouk et al., *Design and construction of the wire chambers for the LHCb Muon System*, Note LHCb 2001-026.

[71] G. Bencivenni et al., *Advances in triple–GEM detector operation for high–rate particle triggering*, Nucl. Instrum. in Phys. Res. **A 513** (2003).

[72] M. Alfonsi et al., *Advances in fast multi–GEM based detector operation for high–rate charged particle triggering*, IEEE Trans. Nucl. Sci. **51** (2004).

[73] G. Sabatino et al., *Cluster size measurements for the LHCb Muon System M5R4 MWPCs using cosmic rays*, Note LHCb 2006-011.

[74] S. de Capua et al., *Study of gas gain uniformity for the LHCb Muon System MWPCs using cosmic rays*, Note LHCb 2006-010.

[75] LHCb Collaboration, *LHCb online system technical design report*, 2001.

[76] N. Brook et al., *LHCb Computing Model*, Note LHCb 2004-119.

[77] LHCb Collaboration, *Addendum to the LHCb online system technical design report*, 2005.

[78] LHCb Collaboration, *LHCb computing : Technical Design Report*, CH-1211 Geneve 23, Suisse, 2005.

[79] O. Heaviside, *On the Electromagnetic Effects due to the Motion of Electrification through a Dielectric*, (1889).

[80] P.A. Cherenkov, *Visible Emission of Clean Liquids by Action of Radiation*, (1934).

[81] The LHCb Coll., *The LHCb Detector at the LHC*, 2008.

[82] The LHCb Coll., *LHCb Technical Proposal*, 1998.

[83] The LHCb Coll., *LHCb RICH TDR*, 2000.

[84] The LHCb Coll., *LHCb Reoptimized Detector Design and Performance TDR*, 2003.

[85] A. Papanestis, *Limits of software compensation for mirror misalignment of the RICH detectors*, Note LHCb 2001-141.

[86] C. D'Ambrosio et al., *The optical systems of LHCb RICHes : a study on the mirror walls and mirrors specifications*, Note LHCb-2000-071.

[87] The LHCb RICH Group, *LHCb RICH 1 Engineering Design Review Report*, 2004.

[88] M.Y. Barnykov et al., *Development of aerogel Cherenkov counters with wavelength shifters and phototubes*, Nucl. Instrum. Meth. **A 419** (1998).

[89] T. Bellunato et al., *Performance of aerogel as Cherenkov radiator*, Nucl. Instrum. Meth. **A 519** (2004).

[90] T. Bellunato et al., *Study of ageing effects in aerogel*, Nucl. Instrum. Meth. **A 527** (2004).

[91] T. Bellunato et al., *Refractive index inhomogeneity within an aerogel block*, Nucl. Instrum. Meth. **A 556** (2006).

[92] T. Bellunato et al., *The RICH with aerogel for the LHCb experiment*, Nucl. Phys. Proc. Suppl. **150** (2006).

[93] D. Perego, *Ageing tests and recovery procedures of silica aerogel*, Note LHCb-2008-004.

[94] O. Ullaland, *Fluid systems for RICH detectors*, Nucl. Instrum. Meth. **A 553** (A 553).

[95] The LHCb RICH Group, *LHCb RICH gas system proposal*, LHCb-2000-079.

[96] The LHCb RICH Group, *LHCb RICH 2 Engineering Design Review Report*, 2002.

[97] M. Alemi et al., *First operation of a hybrid photon detector prototype with electrostatic cross-focussing and integrated silicon pixel readout*, Nucl. Instrum. Meth. **A 449** (2000).

[98] T. Gys, *The pixel hybrid photon detectors for the LHCb-rich project*, Nucl. Instr. and Meth. **A 465** (2001).

[99] M. Moritz et al., *Performance study of new pixel hybrid photon detector prototypes for the LHCb RICH counters*, IEEE Trans. Nucl. Sc. **51**.

[100] N. Kanaya, et al., *Performance study of hybrid photon detectors for the LHCb RICH*, Instr. and Meth. **A 553** (2005).

[101] T. Gys, *Production of 500 pixel hybrid photon detectors for the RICH counters of LHCb*, Nucl. Instr. and Meth. **A 567** (2006).

[102] Stephan Eisenhardt, *Production and tests of Hybrid Photon Detectors for the LHCb RICH detectors*, Nucl. Instr. Meth. **A 595** (2008).

[103] G.Aglieri–Rinella et al., *Performance studies of pixel hybrid photon detectors for the LHCb RICH counters*, Nucl. Phys. **B, Proc. Suppl. 150** (2006).

[104] M.Patel et al., *Magnetic Shielding Studies of the RICH Photon Detectors*, Note LHCb-2005-055.

[105] K. Wyllie, *The front-end electronics of the LHCb ring-imaging-Cherenkov system*, Nucl. Instr. and Meth. **A 567** (2006).

[106] K. Wyllie, *Silicon detectors and electronics for pixel hybrid photon detectors*, Nucl. Instr. and Meth. **A 530** (2004).

[107] A. Powell, *verview of the LHCb RICH Optical Data Link and Evaluation of its Optical Attenuation*, LHCb-2006-003 RICH.

[108] K. Wyllie, *Level-0 Electronics for the LHCb RICH LHCb Technical Note*, LHCb 2000–075 RICH.

[109] F. Legger et al., *TELL1 : development of a common readout board for LHCb*, Nucl. Instr. and Meth Phys. Res. **A 535** (2004).

[110] D. Breton and D. Charlet, *SPECS: the Serial Protocol for the Experiment Control System of LHCb*, LHCb-2003-00.

[111] A. Arnaboldi et al., *The high voltage protection boards for the RICH detectors of LHC*, IEEE Trans. Nucl. Sc. **1** (2007).

[112] A. Arnaboldi et al., *The High Voltage Distribution System for The Hybrid Photodetector Arrays of RICH1 and RICH2 at LHCb*, IEEE Trans. Nucl. Sc. **53, Issue 3, Part 3** (2006).

[113] E. Fanchini, *Caratterizzazione dei fotorivelatori HPD per il RICH di LHCb con fasci di elettroni, protoni e pioni*, 2007.

[114] A. Arnaboldi et al., *The high-voltage system for the LHCb RICH hybrid photon detectors*, Nucl. Instr. and Meth Phys. Res. **A 598** (2009).

[115] F.Fontanelli et al., *Very high voltage power supply system for the ring imaging Cherenkov detectors of the LHCb experiment*, NIM A **604**, 675 (2009).

[116] F.Fontanelli et al., *Embedded Controllers for Local Board–Control*, IEEE Trans. Nucl. Sci. **Vol.53, NO.3** (2006).

[117] F. Fontanelli et al., *CC–PC Gluecard Application and User's Guide*, LHCb 2003-098.

[118] D. Paret, C. Fenger, *The I2C Bus from Theory to Practice* (John Wiley & Sons, 1997).

[119] *IEEE Standard Test Access Port and Boundary–Scan Architecture* (IEEE, New York, NY, 2001).

[120] S. Koestner et al., *Generic and layered framework components for the control of a large scale data acquisition system*, IEEE Trans. Nucl. Sci. **Vol.55, NO.1** (2008).

[121] M. Sannino, *LHCb RICH detector control and high voltage system*, Nucl.Instrum.Meth. **A 595**, 208 (2008).

[122] A. Papanestis, *The LHCb RICH detector control system*, in *LHCb-PROC-2009-049*, 2009.

[123] T. Gys.

[124] B. Storaci, *The LHCb RICH : its application to the study of the $B_s \rightarrow J/\Psi\phi$ decay channel and magnetic distortions corrections*, 2007.

[125] G.F. Knoll, *Radiation detection and measurement (Third edition)* .

[126] J. Christiansen, *Requirements to the L0 front–end electronics*, Note LHCb 2001-014.

[127] LHCb Collaboration, Expression of Interest for an LHCb Upgrade, 2008.

[128] H.Dijkstra, The LHCb Upgrade, in *Proceedings of 5th Flavor Physics and CP Violation Conference (FPCP 2007)*, p. 027, Bled, Slovenia, 2007.

[129] Z. F.Alessio and R.Jacobsson, TFC and readout electronics aspects of the LHCb Upgrade, LHCb note 2008-072, 2008.

[130] M.Artuso, The BTeV RICH front–end electronics, in *Nucl.Instrum.Meth. A553 (2005)*, pp. 130–134, Mexico, 2004.

[131] M.Artuso et al., Performance of a c4f8 gas radiator ring imaging cherenkov detector using multi-anode photomultiplier tubes, Nucl.Instrum.Meth. **A558**, 373 (2006).

[132] C.Arnaboldi et al., Cherenkov light detection for the LHCb RICH Upgrade, in *Proceedings of the 11th International Conference on Particle Physics and Advanced Technology (11th ICPPAT) World Scientific (Singapore) 2010*.

[133] C.Arnaboldi et al., Cross talk study to the single photon response of a flat panel pmt for the rich upgrade at lhcb, Nucl. Sci. Symp. Conf. Rec. 2009 IEEE **Vol. 1**, 1513 (2009).

[134] http://jp.hamamatsu.com/resources/products/etd/pdf/PMT_TPMZ0001E01.pdf.

[135] ALICE Collaboration, First proton-proton collisions at the LHC as observed with the ALICE detector : measurement of the charged particle pseudorapidity density at $\sqrt{S} = 900$ GeV, Eur. Phys. J. C **65**.

[136] Kar, D, Minimum Bias and Early QCD at ATLAS, 2010.

[137] CMS Collaboration, *Transverse momentum and pseudorapidity distributions of charged hadrons in pp collisions at* $\sqrt{s} = 0.9$ *and 2.36 TeV*, J.High Energy Phys. **02** (2010).

[138] Lhcb Collaboration, *Prompt* K^0_S *production in pp collisions at* $\sqrt{s} = 0.9$ *TeV*, Physics Letters B **693**, 69 (2010).

[139] M. Knecht et al., *Measurement of* V^0*particle production at LHCb with 2009 data*, CERN-LHCb-ANA-2010-002, 2010.

[140] T. Blake et al., *Production ratios of prompt* V^0 *particles at LHCb from inelastic non–diffractive pp collisions at* $\sqrt{s} = 0.9$ *TeV and 7 TeV*, CERN-LHCb-ANA-2010-002, 2010.

[141] A. Contu et al., *Measurement of prompt hadron production ratios in pp collisions at* $\sqrt{s} = 0.9$ *and 7 TeV*, CERN-LHCb-ANA-2010-002, 2010.

[142] LHCb Collaboration, *Measurement of* $\sigma(pp \to b\bar{b}X)$ *at* $\sqrt{s} = 7$ *TeV in the forward region*, 2010.

[143] D. Drijard et al., *Neutral strange particle production in proton–proton collisions at* $\sqrt{s}$ *=63 GeV*, 1982.

[144] CDF Collaboration, K^0_S *and* Λ^0 *production studies in* $p\overline{p}$ *collisions at* $\sqrt{s} = 1800$ *and 630 GeV*, Phys. Rev. D **72**, 052001 (2005).

[145] STAR Collaboration, *Strange particle production in* p^+p^- *collisions at* $\sqrt{s} = 200$ *GeV*, Phys. Rev. C **75**, 064901 (2007).

[146] M. Dittmar et al., *Parton Distributions*, ArXiv e-prints (2009), 0901.2504.

[147] A. Sarti, *B Physics at LHC*, ArXiv e-prints (2008), 0809.0450.

[148] T. Sjostrand, S. Mrenna, and P. Z. Skands, PYTHIA 6.4 Physics and Manual, JHEP **05**, 026 (2006), hep-ph/0603175.

[149] M.Deile, *Diffraction and Total Cross-Section at the Tevatron and the LHC*, 2005.

[150] A. M. et al., *Prediction for minimum bias and the underlying event at LHC energies*, Eur. Phys. J. C 50 , 2 (2007) 435-466 **50**, 435 (2007).

[151] *The Brunel Project*, http://lhcb-release-area.web.cern.ch/LHCb-release-area/DOC/brunel/.

[152] *The Gauss Project*, http://lhcb-release-area.web.cern.ch/LHCb-release-area/DOC/gauss/.

[153] *The DaVinci Project*, http://lhcb-release-area.web.cern.ch/LHCb-release-area/DOC/davinci/.

[154] *The MOORE Project*, http://lhcb-release-area.web.cern.ch/LHCb-release-area/DOC/moore/.

ACKNOWLEDGMENTS

My Ph.D. would have never been possible to accomplish, and to carry out all the work fulfilled during these years, without the support of all the people around me.

First of all, I would say thanks to my supervisor Clara Matteuzzi for having introduced me to the wonderful high–energy physics world. You have supported me since my Master Thesis!

A warm thanks you goes also to Gianluigi Pessina. Your help was always indispensable, especially in the laboratory. You were always available to answer any question and to give me suggestions. I will never forget that.

Another important person who taught me a lot is Thierry Gys: your patience is without limits. Thanks to have introduced me to the high voltage world and for the "Spike–Girl", I will bring the nickname in my heart forever.

I have benefitted of supports from the Università degli Studi di Milano–Bicocca and I.N.F.N. They were essential to bring this work to completion.

I don't want to forget the whole LHCb experiment!!!
I never forget all the exiting moments spent with all of you at CERN!
Good Luck!

A peculiar thanks you goes to all the people I met and that I can't stand or I don't understand. Your presence remembers me, every day, the kind of person I don't want to be and I don't want to become.

I know that there are so many people who helped me a lot...not only at work. Discussions, critics or simply chats were indispensable.
You are spread over few countries, independently from the fact I know you since childhood or I met you more recently: "you have been and will be with me, thanks friends!"

Ed ora il grazie più profondo che riesco ad esprimere.
Questo va alla mia famiglia, mi siete stati vicini in ogni circostanza, mi avete aiutata e sopportata, anche nelle mie follie.
Vi voglio bene e non ve lo ripeterò mai abbastanza.

Erica

...non ci guarderemo indietro mai.

Negrita - Non ci guarderemo indietro mai